Politecnico di Torino

Master's degree in Civil Engineering
Academic Year.2024/2025
Graduation Session: December 2025

Seismic assessment of masonry bell towers by nonlinear analysis and modelling

Supervisor:

Prof. Rosario Ceravolo

Co-Supervisors:

Ing. Gaetano Miraglia

Ing. Linda Scussolini

Ing. Alessio Crocetti

Candidate:

Lutfullah Sarwari s329597

For those who supported me.

Abstract

The assessment and evaluation of historical masonry structures represent a well-known problem in the field of seismic engineering. Indeed, their unique value, often associated with a lack of documentation, represents also a constraint in the testing and evaluation of their geometrical and mechanical characteristics. Among them, bell towers represent a compelling category with inherent complexity, due to their slenderness and to the presence of elements such as large opening and adjacent buildings. In this context, appropriate models to simulate structural behavior play a fundamental role, especially in the definition of proper materials characteristics. The complexity in the behavior of these structures is often related to nonlinearity in material and geometric irregularity, requiring advanced computational tools. Nevertheless, implementing Finite Element Model (FEM), which proves effective in the case of simplified linear models, and performing nonlinear analyses involving the whole structure requires significant computational time, making obtaining reliable results in reasonable time difficult. The aim of this thesis is to explore more efficient modelling strategies. Following this approach, only the most vulnerable part of the structure is simulated with nonlinear laws, while the remaining part will follow a common linear elastic model. The proposed strategy is evaluated on a valuable case study, given by the masonry bell tower of the old parish church of S. Antonio Abate in Montà (CN, Italy), assessing its effectiveness.

Table of Contents

List of Figures

List of Tables

Introduction

Historic masonry structures are an important part of cultural heritage, yet they are also among the most vulnerable to seismic actions. Their complex geometry, material inelasticity and degradation make it difficult to predict their behavior during earthquakes. Failures in these structures often occur due to cracking, crushing, and progressive stiffness loss, which can lead to partial or total collapse. Understanding and accurately modeling these mechanisms is therefore essential for the preservation and seismic safety of masonry structure [1].

Among historical masonry structures, bell towers represent a challenging category, as their height and slender geometry make their response strongly affected by dynamic effects and lateral loads. The presence of large openings and the partial interaction with adjacent church buildings further increase their seismic vulnerability. Even moderate ground motions can lead to cracking and localized damage, emphasizing the need for reliable numerical tools to assess their safety [1].

Nonlinear modelling and analysis are essential for understanding the behavior of masonry structures. Such analyses are required to capture the actual damage mechanisms through advanced constitutive laws, since purely elastic models cannot represent the progressive cracking and collapse behavior. A detailed nonlinear simulation provides a realistic picture of the sequence of damage and the overall collapse mechanism. However, performing a detailed nonlinear analysis for the entire structure is computationally demanding.

In this context, this thesis introduces an efficiency-oriented approach that combines localized nonlinear analysis with a data-driven surrogate model. A set of nonlinear simulations is first used to train surrogate models capable of predicting strain and damage indicators throughout the tower. These predictions are then evaluated within model optimization, which explores the material parameter domain and identifies the region most likely to develop nonlinear behavior. The resulting damage distribution leads the use of a localized nonlinear finite-element model, where nonlinear constitutive laws are assigned only in the zones identified as damaged.

The thesis is organized as follows:

- Chapter 1 introduces the problem and research objectives.
- Chapter 2 reviews the mechanical behavior of masonry and the nonlinear

constitutive models adopted.

- Chapter 3 presents the case study and the baseline nonlinear analysis.
- Chapter 4 describes the construction, validation, and damage extraction of the surrogate models.
- Chapter 5 details the model optimization for nonlinear analyses, including sampling, optimization, damage distribution, and localized nonlinear modelling.
- Chapter 6 provides a discussion of the results and computational benefits.
- Chapter 7 concludes the thesis and outlines possible future developments.

.

1.0 Problem description and research objectives

Performing a full nonlinear analysis for the entire structure of a masonry bell tower requires substantial computational effort. A fine mesh is necessary to accurately capture the complex geometry and stress gradients of the tower. When this high level of discretization is combined with the nonlinear constitutive behavior of masonry and the iterative nature of the nonlinear numerical analysis, the analysis becomes computationally intensive and may encounter convergence issues. Depending on the mesh density and boundary conditions, a single simulation can require several hours or even days. This computational effort represents a major limitation for structural assessment, particularly when numerous analyses are needed for calibration, validation, or parametric studies.

Despite these challenges, nonlinear modeling remains the most accurate approach for predicting real structural behavior and assessing safety margins. To use its advantages while keeping the analysis efficient, a targeted modeling strategy is required, one that applies nonlinear formulations only where they are most needed. For masonry, which behaves as a brittle material, failure is governed by localized mechanisms rather than by uniform degradation across the structure. Cracking and crushing tend to initiate and develop in regions of stress concentration or geometric discontinuity, such as openings, connections with other structures, or slender wall segments. These critical areas govern global stability and the resulting collapse mechanism of the structure.

To further improve efficiency and generalize the analysis, a probabilistic surrogate regression model was developed based on a numerical dataset. A total of 200 nonlinear analyses were carried out by varying the tensile and compressive strengths of the masonry material. From each simulation, the nodal stress–strain fields and the corresponding capacity curve were extracted. The equivalent plastic strain (EPS) is used as a quantitative indicator of damage, consistent with established approaches for masonry modeling. Using this data, a regression-based surrogate model was trained to capture the relationship between material parameters and the resulting damage distribution within the structure.

This surrogate framework allows the rapid prediction of damage distribution and structural capacity without the need for additional nonlinear analyses. In this way, it combines the accuracy of nonlinear finite element modeling with the computational speed required for large-scale parametric studies and probabilistic assessment procedures. As a result, the proposed approach offers a practical and efficient tool for evaluating the capacity and collapse mechanisms of historical masonry bell towers.

2.0 Nonlinear model for masonry structures

Masonry is one of the oldest structural materials, and it is still used in modern construction through traditional techniques [2]. The widespread use of masonry structures on a global scale can be attributed to the simplicity of their construction techniques and their visually appealing form. Historically, the design of masonry was largely empirical, with practices developed through trials and errors without numerical calculation and prediction about the behavior [2].

Masonry is a composite material which is composed primarily of blocks, which may be stone or brick, and the material that serves to bind these blocks together, known as mortar. The constituent materials of masonry are inherently fragile, and due to the arrangements of components, the resultant structure exhibits inelastic, heterogeneous, and anisotropic properties [2]. The properties of masonry depend not only on the characteristics of the brick and mortar but also on the conditions under which it is loaded. Its behavior differs significantly under compressive and tensile stresses [2], [3], [4].

2.1 Mechanical behavior of masonry

To understand the behavior of masonry, it is necessary to understand the behavior of its individual components, including the properties of the masonry units and the characteristics of the mortar. The mechanical characterization of masonry is traditionally obtained through experimental testing. Previously, the widely used method for assessing the compressive strength of masonry was the use of a stacked prism of masonry under uniaxial loading. However, nowadays the RILEM test has emerged as the prevailing standard within the masonry community [2]. The behavior of masonry under uni-axial and bi-axial stresses is discussed in the following subchapters.

2.1.1 Uni-axial behavior of masonry

Uni-axial testing is one of the most used tests for defining constitutive law for materials. In masonry, brick units are subjected to compression testing, a method that

allows the assessment of the response of various brick types, each possessing distinct elasticity modules, the relationships between compressive strength and modulus of elasticity, ranging from 150 to 500 times compressive strength. In the context of compressive stress, bricks demonstrate linear behavior up to 33 percent of their ultimate strength. Beyond this threshold, a transition to nonlinear behavior occurs [4]. Similarly, mortar exhibits linearity up to roughly one-third of its compressive strength, after which its response becomes nonlinear. The modulus of elasticity ranges from 100 to 400 of the mortar compressive strength. In the context of composite materials, the response of a system composed of two distinct ingredients, stiff brick and soft mortar, subjected to uniaxial compressive stress, is characterized by a response that falls somewhere between the properties of its constituent parts [4].

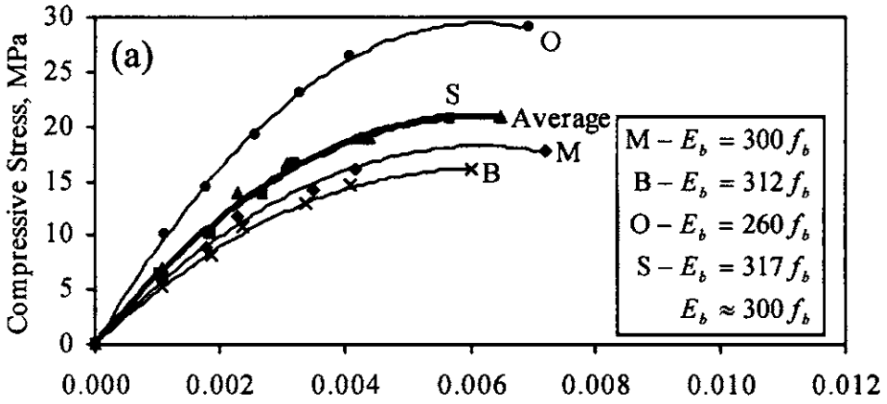

Figure 1 Compressive stress-strain curves for brick units. [4]

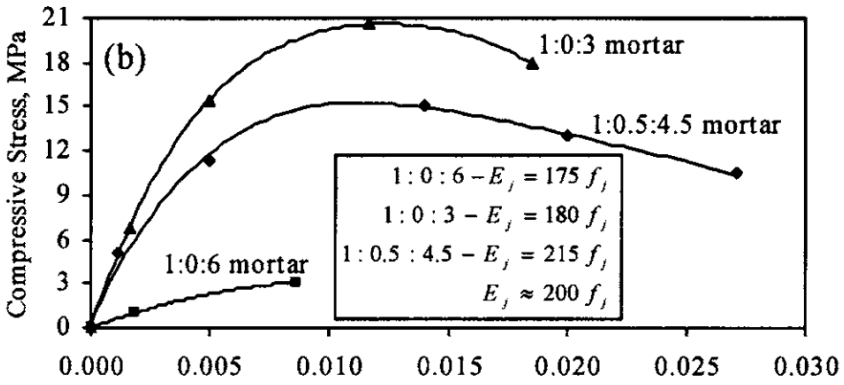

Figure 2 Compressive stress-strain curves for mortar [4]

The compressive strength of masonry prism which depend on the compressive strength of brick and mortar can be determined by the following equation:

$$f'_m = K\, f_b^{\alpha} f_j^{\beta} \quad [4]$$

Where K, α, and β are constant, depending on the mortar, brick and interface

properties. The compressive strength of masonry is highly dependent on the compressive strength of brick than mortar; therefore, the coefficient α is greater than β. The value of α , and β are 0.65 and 0.25, respectively, and the value of the K is between 0.4 to 0.6 [5].

According to the experimental data Dayaratnam (1987) proposed mathematical relationships as:

$$f'_m = 0.275\, f_b^{0.5} f_j^{0.5} \quad [3]$$

Similarly, based on the experimental tests using the above equations proposed another relationship for finding compressive strength of masonry from the compressive strength of mortar and brick as follows:

$$f'_m = 0.63\, f_b^{0.49} f_j^{0.32} \quad [3]$$

The constant used in the Dayaratnam formula, which gives the same percentage for both brick and mortar, makes the estimation assuming higher value than the real one; for this reason, the update coefficients have been calibrated and provide more reliable estimation. The value of the modulus of elasticity is about 250 to 1100 of the compressive strength of masonry [4].

According to NTC 2018, a value of $E'_m = 1000 f'_m$ is recommended, and this expression is adopted in the present work to determine the compressive strength.

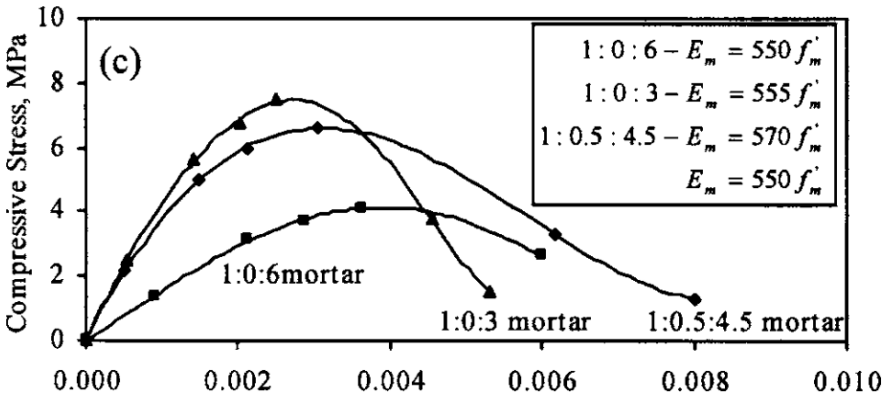

Figure 3 Compressive stress-strain curves for prism masonry [4]

Masonry behaves as a quasi-brittle composite in which failure is governed by crack initiation, propagation and localization. Under uniaxial tension, the strain-stress curve is somehow linear elastic up to tensile strength f_t and after reaching this point crack propagate and material show softening behavior which is governed by fracture energy G_f. The mode I of failure under tensile stress depends on the bond area or the net bond

area and based on this the fracture energy G_f is for masonry between 5.0 J/mm^2 to 20 J/mm^2 and the tensile bond strength from 0.3 N/mm^2 to 0.9 N/mm^2 [2].

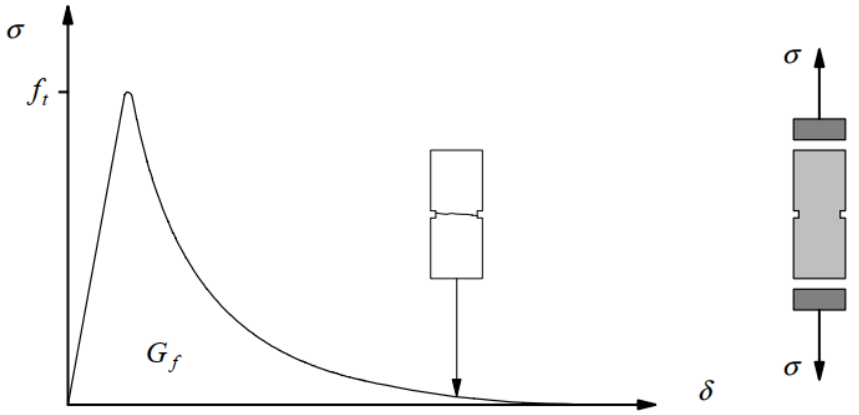

Figure 4 Typical behavior of quasi-brittle materials under uniaxial tensile loading [2]

In masonry structures, failure may occur in either the brick or the mortar, although the mortar, being the weaker component, typically governs the response, and most failures therefore originate within the joints. This is due to the natural anisotropic behavior of masonry, in which the failure of the composite under uniaxial compression stress is related to the orientation of bed joint and the direction of the applied stress [3]. Similarly, under uni-axial tension, the strength is highly dependent on properties of constituent material and the orientation of the joint with respect to loading. Tensile failure is commonly results from insufficient bond strength between brick and mortar; however, when the bond strength is particularly high, failure may instead occur within the brick itself [3].

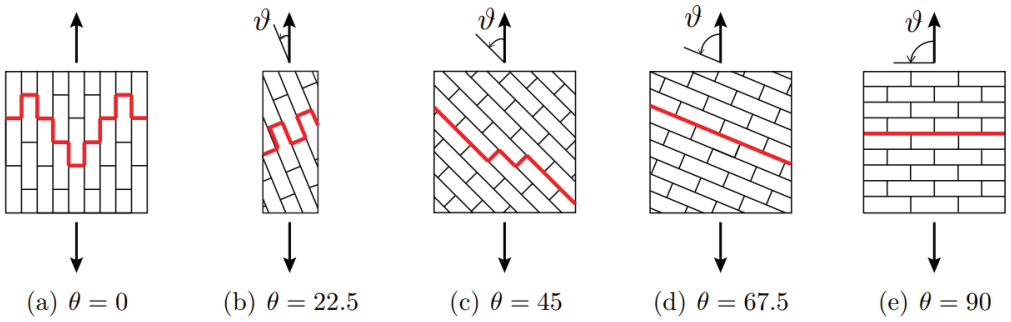

Figure 5 Local state of stress in masonry prisms under uni-axial tension with different orientation θ from the bed joint direction. [3], [6]

Under compression, the brick–mortar interaction is complex. Due to its lower stiffness, mortar tends to expand more than brick. This differential deformation is restrained by friction and cohesion at the interface, generating shear stresses that induce triaxial compression in the mortar and biaxial tension in the brick [4].

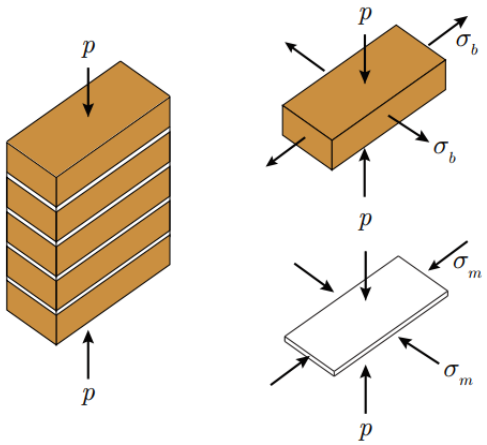

Figure 6 Compressive behavior for uni-axial load normal to bed joints state of stress in masonry constituents [6]

In most cases the softening branch in the tensile stress regime is neglected and considered as elastic perfectly brittle. Under compression, after reaching to the compressive strength f_c show the same softening behavior but with a reduction in strength while the failure mode does not exhibit excessive brittleness, and strain softening is evident. Which is governed by G_c the compression fracture energy, both G_f and G_c are the properties of material [2].

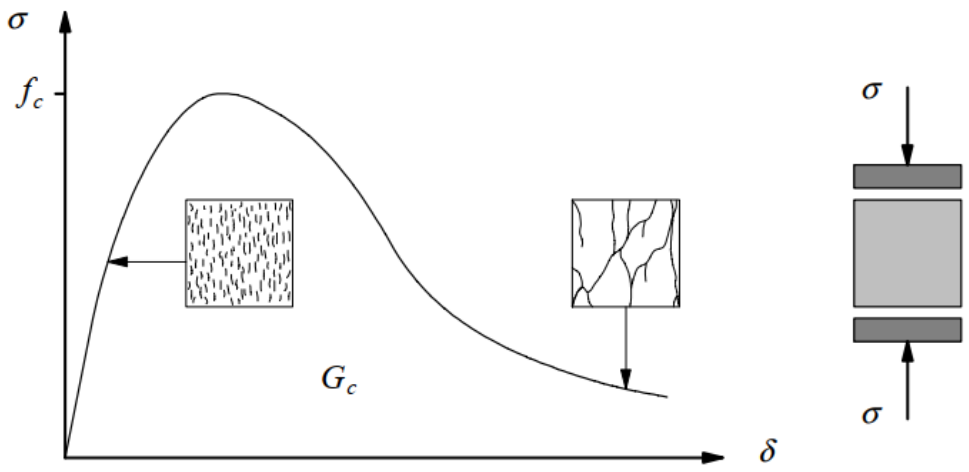

Figure 7 Typical behavior of quasi-brittle materials under uniaxial compressive loading [2]

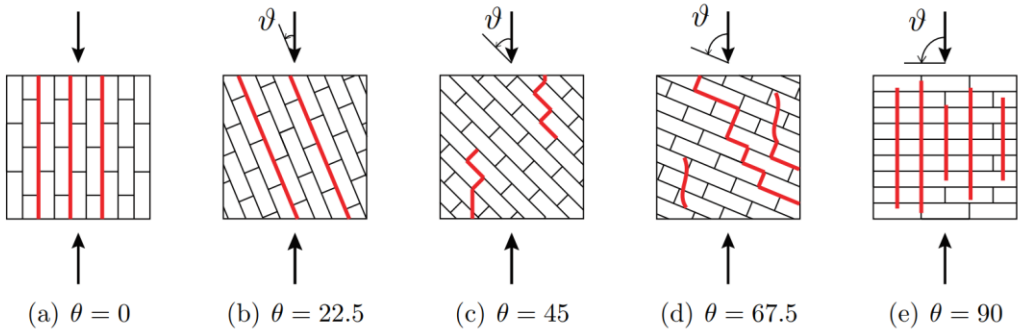

Figure 8 Local state of stress in masonry prisms under uni-axial compression with different orientation θ from the bed joint direction. [3], [6]

2.2.2 Bi-axial behavior of masonry

Masonry material behaves differently depending on the direction it is stressed. It's harder to predict how materials behave under biaxial stresses (stress is applied along two different directions) than it is under uniaxial stresses [2]. Experiments have shown that in compression/tension state of stress the strength of masonry can vary greatly based on the direction of the principal stresses with respect to the material axis (bed joint orientation) and the ratio between the two principal stresses, σ_1 and σ_2. When a particular principal stress becomes higher, failure occurs at the joints. In compression/compression state of stress the failure occurs in plane of the prism, resulting in a division of the prism at its midpoint and is not dependent on the bed joint orientation and is not related to the orientation of the bed joint and/or the ratio of the principal stresses. The observed strength is greater than the uniaxial strength [3].

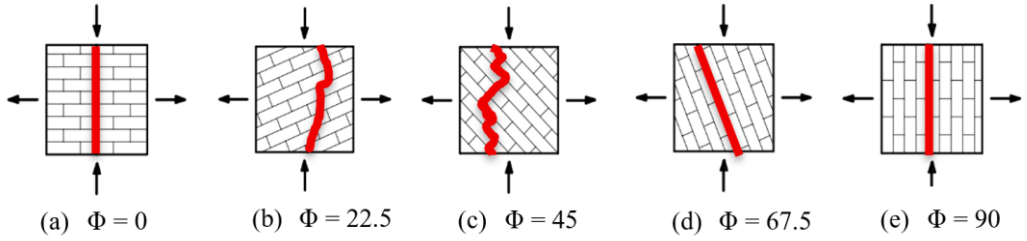

Figure 9 Modes of failure of solid clay units masonry under biaxial compression/tension state of stress Dhansaseker et al. (1985) [1]

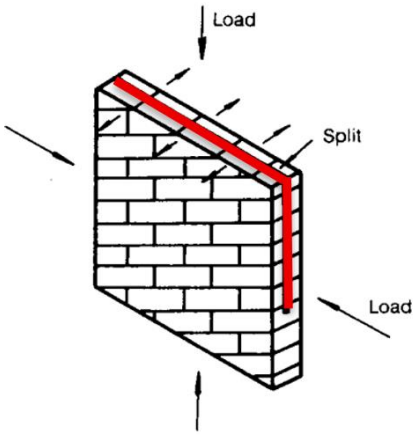

Figure 10 Mode of failure of solid clay unit masonry under biaxail compression/compression state of stress Bi-axial failure [3]

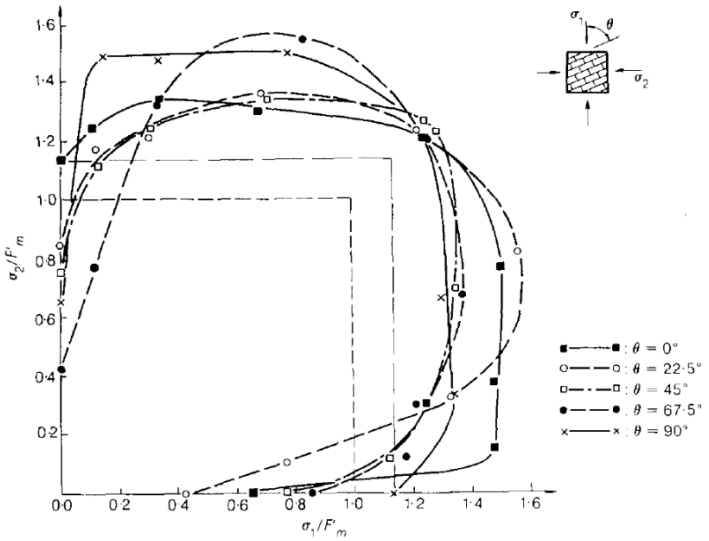

Figure 11 Failure surface for brickwork projected on to σ_1 - σ_2 plane [3]

It is possible to define the in-plane failure by normal stress and shear stress instead of σ_1, σ_2 and θ. Particularly, σ_n which is normal to the bed joint, σ_p which is parallel to the bed joint and τ which is shear stress. This type of failure is called mode II of failure and is governed by G_f^{II} fracture energy. This type of failure is caused by the amount of normal and shear loading. It is also based on the properties of the constituents, blocks, and mortar.

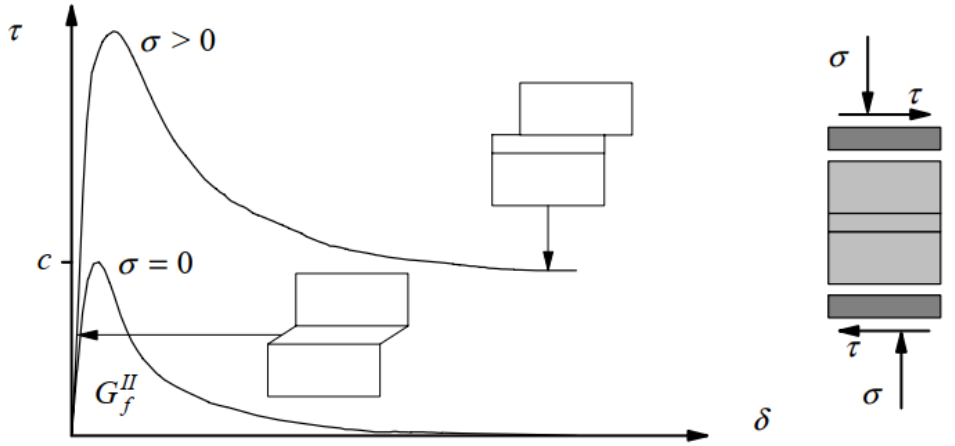

Figure 12 Behavior of masonry under shear and definition of mode II fracture energy G_f^{II} (c denotes the cohesion)[2].

The result of this test reveals some important characteristics of masonry. First, the type of failure depends on the amount of normal stress. When the confining stress is sufficiently high, the failure mode tends to shift toward diagonal shear, meaning that the fracture develops through zigzag cracking along the joints or through diagonal crushing of the units. Second, the fracture energy G_f^{II} for masonry ranges from 10 J/mm^2 to 250 J/mm^2. The initial friction angle which is computed as $tan\varphi_0$ varies between 0.7 and 1.2 for different types of mortar, while the residual friction angle computed as $tan\varphi_r$ remains approximately constant value of 0.75. According to the test the dilatancy angle $tan\psi$, which measures the uplift of one unit over another, assumes values from 0.2 to 0.7 for low confinement masonry and zero for high confined masonry [2].

Assigning this type of behavior depends on the modeling scale, whether a micro or macro modeling approach is used. In micro models, since the mechanical properties are assigned separately to each component (brick, mortar and the joint), allowing a better representation of actual response under the different loading conditions. In contrast, continuum (macro) models treat masonry as a homogenized material, where an inelastic constitutive law with calibrated tensile, compressive, and shear characteristics is employed to reproduce a response equivalent to that of the detailed micro-model [7].

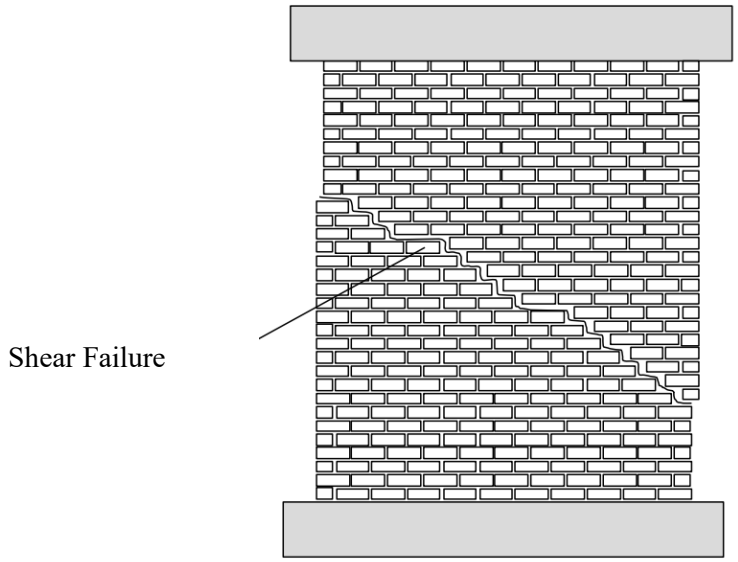

Figure 13 Typical shear failure [7]

Another type of failure will occur when the mortar strength is low, and the horizontal stress is large. This will cause the brick units to slide over each other and slip [7].

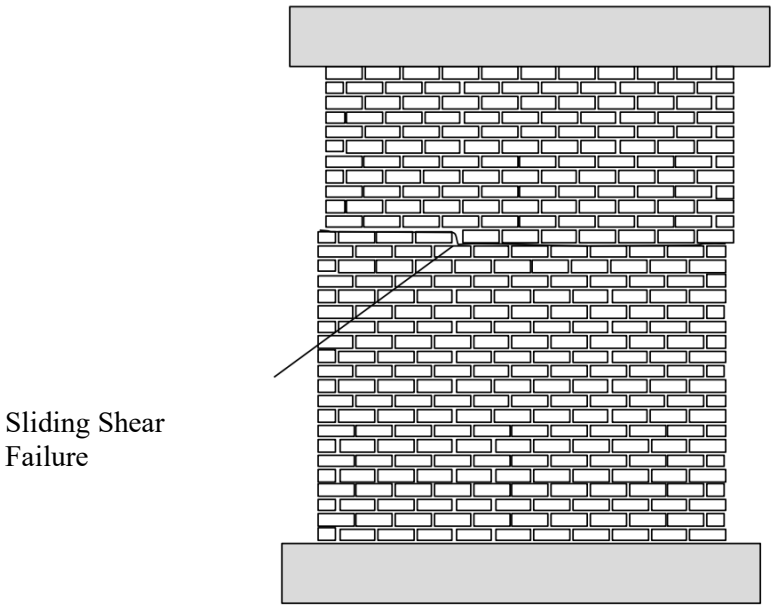

Figure 14 typical sliding shear failure [7]

In circumstances where the wall is exposed to low confined stress yet exhibits high shear resistance, the resultant failure will be of the bending type. Even in scenarios where the horizontal load is not substantial, the wall will undergo a rocking motion, with one segment experiencing tension and the other compression. Consequently, the wall will collide with the compression segment, thereby propagating a crack in the tension segment [7].

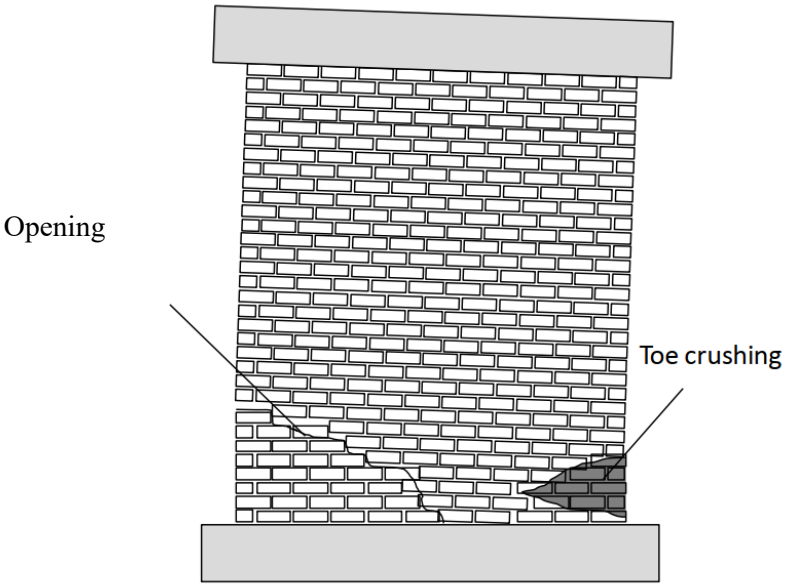

Figure 15 Typical bending failure [7]

2.3 Nonlinear constitutive models for masonry

Based on the understanding of masonry behavior under different stress conditions and corresponding failure mechanisms, it becomes possible to develop a constitutive model capable of reproducing its nonlinear response. To accurately capture the anisotropic and inelastic behavior, it is necessary to define appropriate yield surfaces and failure criteria. As previously discussed, the material response differs under tension and compression; therefore, the constitutive model to be employed should be a composite model that treats these two regimes separately .In this context, a Rankine-type criterion is typically adopted to describe tensile cracking, while a Hill-type or Drucker–Prager-type criterion is used to model compressive failure [2].

In the material library of ANSYS, several geo-mechanical constitutive models are available to simulate the nonlinear behavior of materials such as masonry, rock, and concrete, both in their natural and engineered forms. These models are designed to capture material failure along stress concentrations or weak regions, including the cracking of masonry, the crushing of concrete, and the failure of intact or jointed rock masses [8]. The following sections present a brief discussion of the material models used to simulate the nonlinear behavior of masonry structures, as well as the masonry wall adopted as a benchmark to verify these models.

2.3.0 Benchmark wall model

Material models that will be presented later, are applied to the shear wall commonly used in the masonry community, specifically the one used in the CUR 1994 project. The wall has a width of 990 mm, a height of 1000 mm, and a thickness of 100 mm, and it is tested under a compressive stress of 0.3 MPa while being subjected to either a monotonic displacement or a monotonic force at the top [2], [9].

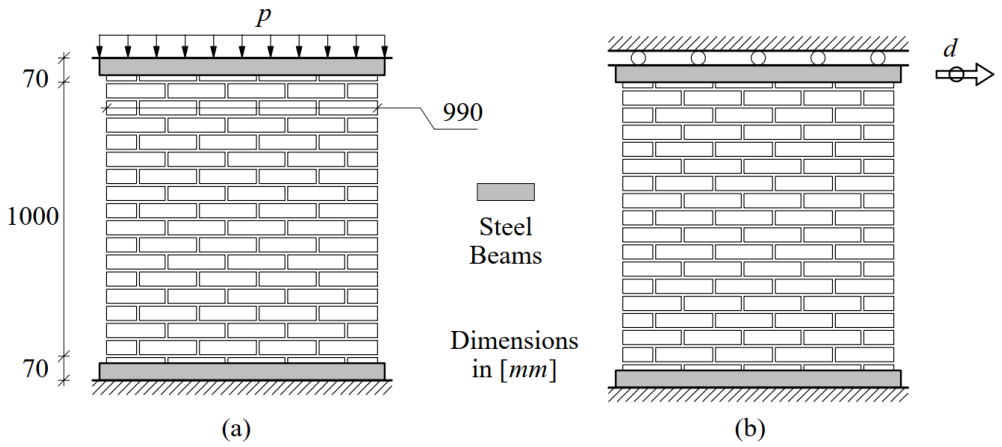

Figure 16 Load on shear walls: (a) phase 1 - vertical loading;(b) phase 2 - horizontal loading under displacement control [2], [9]

The wall is modeled as continuum model with mesh size of 0.025 and is fixed at the base. The loading is applied in the following configuration, first the vertical pressure of 0.3 MPa then the monotonic displacement is applied horizontally while the displacement is fixed in the vertical direction because in real test there is a concrete beam which is fixed the tilting of the wall.

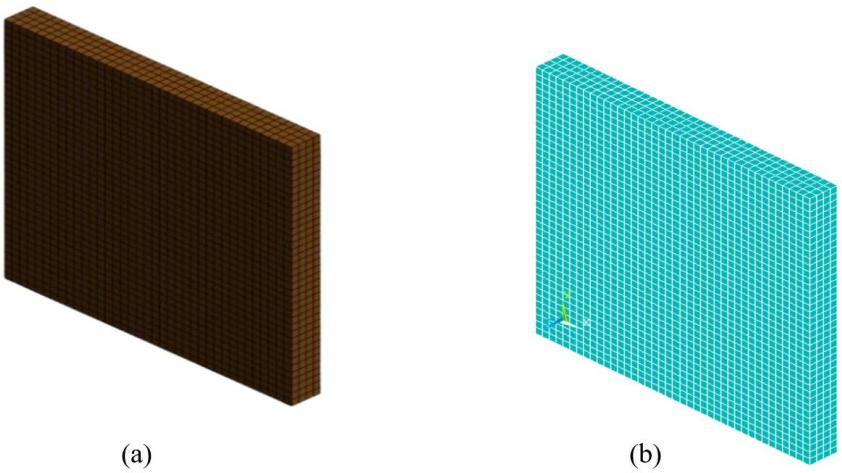

Figure 17 Adopted mesh for the simulated masonry wall [13]

The properties of the wall under the numerical analysis are as follows: [10]

Parameter	Symbol	Value
Young's Modulus (MPa)	E	3200
Poisson's coefficient (-)	ν	0.15
Compressive strength (MPa)	f_c	6.32
Tensile strength (MPa)	f_t	0.36
Cohesion (MPa)	c	0.6
Friction Angle (°)	φ	36
Dilatancy Angle (°)	ψ	0
Open shear transfer coefficient (-)	β_0	0.2
Closed shear transfer coefficient (-)	β_c	0.2

Table 1 Material properties of the benchmark wall

This test is used to assess the shear capacity and overall behavior of the masonry material model, and the results indicate a peak strength of about 50,000 N, as confirmed by both experimental data and numerical simulations. According to the experimental results, the response is initially linear up to roughly 33% of the compressive strength, after which nonlinear hardening develops until the peak load is reached, followed by a progression into the strain-capacity range. This comparison also allows verification of the predicted crack pattern and failure mechanism, which is essential for validating the material model[10].

2.3.1 Mohr-Coulomb Failure Criteria

This model is based on the Mohr-coulomb yield criterion which the concept is that the yield surface follows a linear relationship between normal and shear stresses and formulates as follows:

$$\tau = c - \sigma \tan \varphi \quad [8]$$

Where τ is the shear stress, c is the cohesion, σ is the normal stress, and φ is the inner friction angle. Based on this equation, the greater the normal stress, the greater the shear resistance. The friction angle is proportional to the stress required to shear particles past one another. Loose materials have low friction angles, but in the case of

masonry, this value is somewhat high. Based on the mortar mixture.

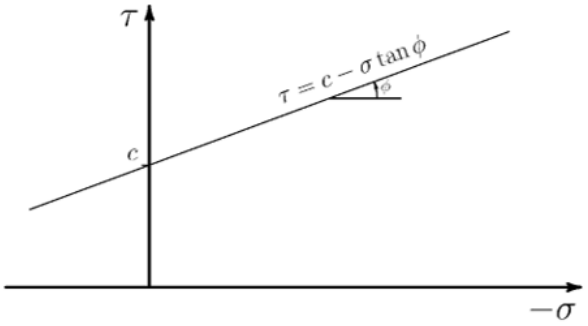

Figure 18 Mohr-Coulomb Yield Surface as Shear vs. Normal Stress [8]

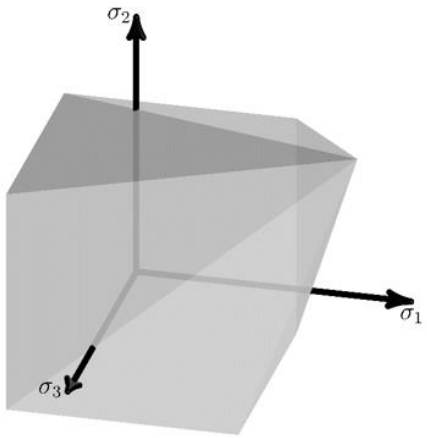

Figure 19 Mohr-Coulomb Yield Surface in Principal Stresses [8]

Generalization to any state of stress gives the Mohr-Coulomb yield surface:

$$f_{MC}(\sigma) = \sigma_m \sin\phi + \frac{\sigma_e}{\sqrt{3}}\left(\cos\theta - \frac{\sin\theta \sin\phi}{\sqrt{3}} - c\cos\phi\right) [8]$$

Where,

$$\sigma_m = \frac{\sigma_{11}+\sigma_{22}+\sigma_{33}}{3}, \qquad \sigma_e = \sqrt{3J_2}, \qquad \sin(3\theta) = -\frac{3\sqrt{3}}{2}\frac{J_3}{\sqrt{J_2^3}} \quad [8]$$

$$J_2 = 1/6\left((\sigma_{11}-\sigma_{22})^2 + (\sigma_{22}-\sigma_{33})^2 + (\sigma_{33}-\sigma_{11})^2 + (\sigma_{12}^2+\sigma_{23}^2+\sigma_{13}^2)\right)[8]$$

$$J_3 = \det(\sigma - I\sigma_m) \ [8]$$

In ANSYS, it is possible to combine the yield surface with the tension-failure surface to limit material strength in tension.

$$f_R(\sigma) = \sigma_m + \frac{2}{3}\sigma_e \sin(\theta + 120°) - T$$

where T is the tensile strength of the material.

For M-C model in total we need to define five parameters which are the initial inner friction angle (ϕ), initial cohesion (c), dilatancy angle (ψ), residual inner friction angle (ϕ'), residual cohesion (c') and if Rankine yield surface for the tension is also considered so the initial tensile strength (T), and residual tensile strength (T') should also be considered.

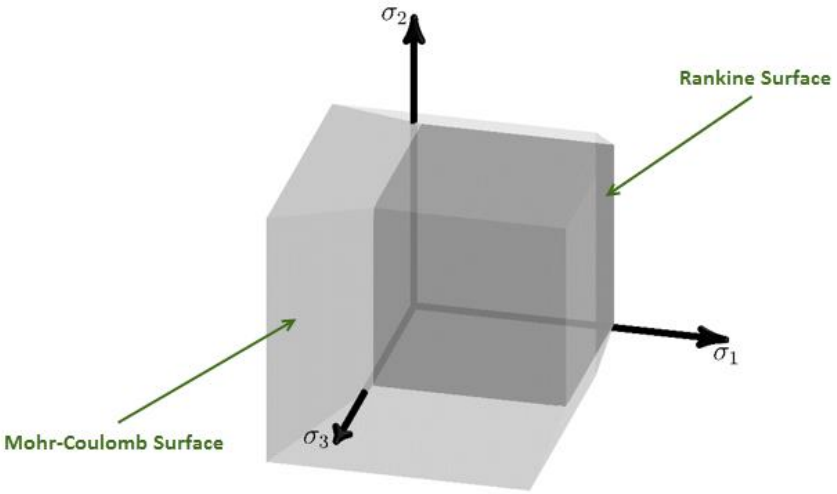

Figure 20 Mohr-Coulomb with Tension-Failure Yield Surface in Principal Stress [8]

Mohr-Coulomb criteria failure is generally used for geotechnical materials and is widely used in geotechnical field; its simplicity is one of the major advantages.

No.	Parameter	Symbol	Value	Unit
1	Elastic modulus	E	3.20×10^9	Pa
2	Poisson's ratio	ν	0.15	–
3	Friction angle	φ	36	°
4	Cohesion	c	0.6×10^6	Pa
5	Dilation angle	ψ	0	°
6	Residual friction angle	φ_r	25	°
7	Residual cohesion	c_r	$0.5 \times c = 0.3 \times 10^6$	Pa
8	Tensile strength	f_t	0.36×10^6	Pa
9	Residual tensile strength	σ_{tr}	$0.7 \times \sigma_t = 0.252 \times 10^6$	Pa

Table 2 M-C model parameter values

M-C failure criteria which work well for geotechnical material require defining data such as angle of friction, cohesion and mechanical parameters of masonry wall, which can be derived from material testing, or it is possible to get values from literature. The result from M-C failure criteria reveals that the material after reaching peak strength there is sudden drop of strength and continues the same behavior until the strain capacity.

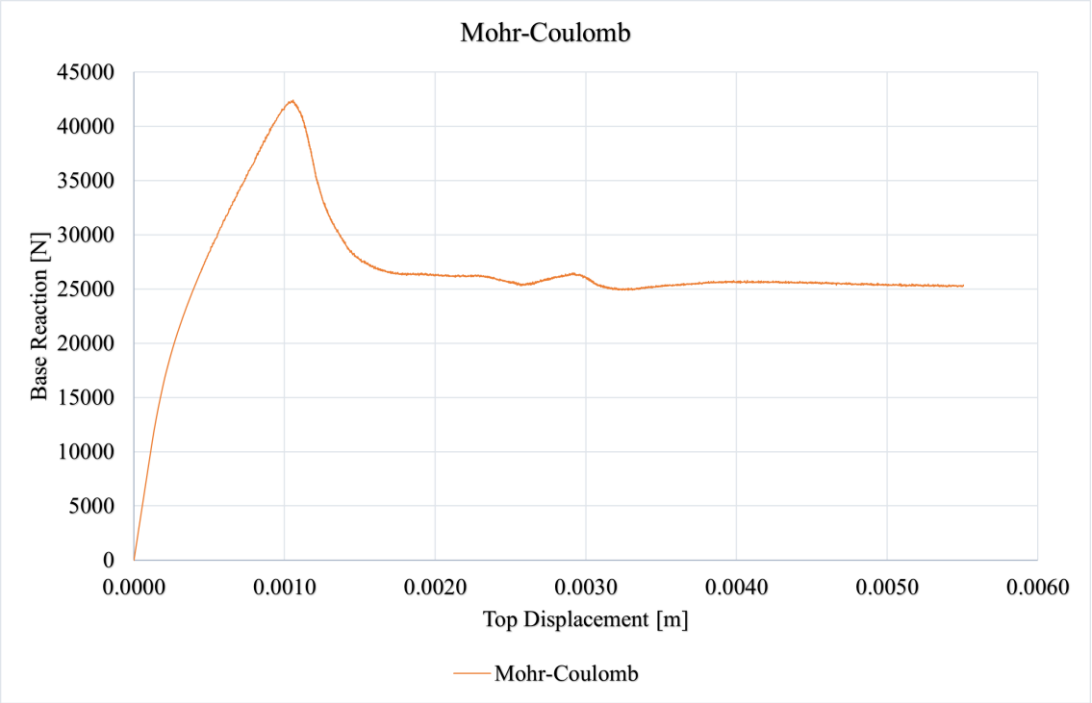

Figure 21 Capacity Curve of the shear wall for M-C model

It's not recommended to use M-C model for masonry since the M-C concept doesn't consider the effect of the intermediate principal stress on the material's shear strength which can be seen in true triaxial testing. Furthermore, the M-C model failure surface has sharp edges, which makes it hard to use the criterion for numerical analysis [11].

2.3.2 William-Warnke failure criteria

The William-Warnke model is originally used for modeling concrete and exhibits properties of plasticity, creep, cracking, and crushing. This material model predicts either plastic behavior, cracking behavior, or crushing behavior. SOLID 65 element in ANSYS which is named as legacy element, permits the incorporation of four distinct materials within each element, including one matrix material for example for concrete and a maximum of three independent reinforcing materials. The criterion for

failure of concrete due to a multiaxial stress state can be expressed as:

$$\frac{F}{f_c} - S \geq 0$$

Where,

F = a function of the principal stress state (σxp, σyp, σzp)

S = failure surface expressed in terms of principal stresses

Fc = is the uniaxial compressive strength [crushing strength].

If the above equation is satisfied, the material will crack or crush.

For different states of stress, the function F and S can be found as follows:

The domain (compression – compression – compression)

where $0 \geq \sigma_1 \geq \sigma_2 \geq \sigma_3$ the function F and S are:

$$F = F_1 = \frac{1}{\sqrt{15}}[(\sigma_1 - \sigma_2)^2 + (\sigma_2 - \sigma_3)^2 + (\sigma_3 - \sigma_1)^2]^{\frac{1}{2}}$$

The failure surface can be computed by:

$$S = S_1 = \frac{2r_2(r_2^2 - r_1^2)\cos\eta + r_2(2r_1 - r_2)[4(r_2^2 - r_1^2)\cos^2\eta + 5r_1^2 - 4r_1r_2]^{\frac{1}{2}}}{4(r_2^2 - r_1^2)\cos^2\eta + (r_2 - 2r_1)^2}$$

The term $\cos\eta$ can be computed by:

$$\cos\eta = \frac{2\sigma_1 - \sigma_2 - \sigma_3}{\sqrt{2}[(\sigma_1 - \sigma_2)^2 + (\sigma_2 - \sigma_3)^2 + (\sigma_3 - \sigma_1)^2]^{\frac{1}{2}}}$$

Where,

$$r_1 = a_0 + a_1\xi + a_2\xi^2 \quad , \quad r_2 = b_0 + b_1\xi + b_2\xi^2 \quad , \quad \xi = \frac{\sigma_h}{f_c}$$

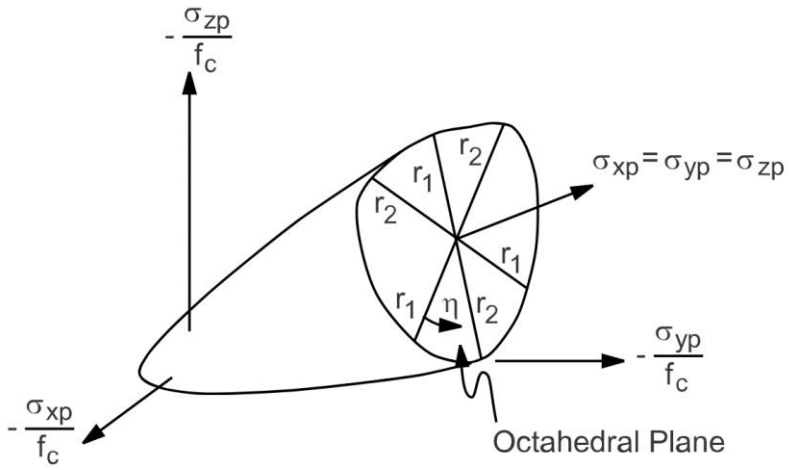

Figure 22 3D Failure Surface in Principal Stress Space [8]

The parameters r1 and r2 are defined by matrix form which I did not report here.

The domain (tension – compression – compression)

where $\sigma_1 \geq 0 \geq \sigma_2 \geq \sigma_3$ the function F and S are:

$$F = F_2 = \frac{1}{\sqrt{15}}[(\sigma_2 - \sigma_3)^2 + \sigma_2^2 + \sigma_3^2]^{\frac{1}{2}}$$

The failure surface can be computed by:

$$S = S_2 = \left(1 - \frac{\sigma_1}{f_t}\right)\frac{2p_2(p_2^2 - p_1^2)\cos\eta + p_2(2p_1 - p_2)[4(p_2^2 - p_1^2)\cos^2\eta + 5p_1^2 - 4p_1p_2]^{\frac{1}{2}}}{4(p_2^2 - p_1^2)\cos^2\eta + (p_2 - 2p_1)^2}$$

Where,

$$p_1 = a_0 + a_1\chi + a_2\chi^2 \quad , \quad p_2 = b_0 + b_1\chi + b_2\chi^2 \quad , \qquad \chi = \frac{(\sigma_2 + \sigma_3)}{3f_c}$$

The domain (tension – tension – compression)

where $\sigma_1 \geq \sigma_2 \geq 0 \geq \sigma_3$ the function F and S are:

$$F = F_3 = \sigma_i; \quad i = 1,2$$

$$S = S_3 = \frac{f_t}{f_c}\left(1 + \frac{\sigma_3}{f_c}\right); \quad i = 1,2$$

If the failure criterion for both i = 1, 2 is satisfied, cracking occurs in the planes perpendicular to principal stresses σ_1 and σ_2. If the failure criterion is satisfied only for i = 1, cracking occurs only in the plane perpendicular to principal stress σ_1.

The domain (tension – tension – tension)

where $\sigma_1 \geq \sigma_2 \geq \sigma_3 \geq 0$ the function F and S are:

$$F = F_4 = \sigma_i, \quad i = 1,2,3$$

$$S = S_4 = \frac{f_t}{f_c}$$

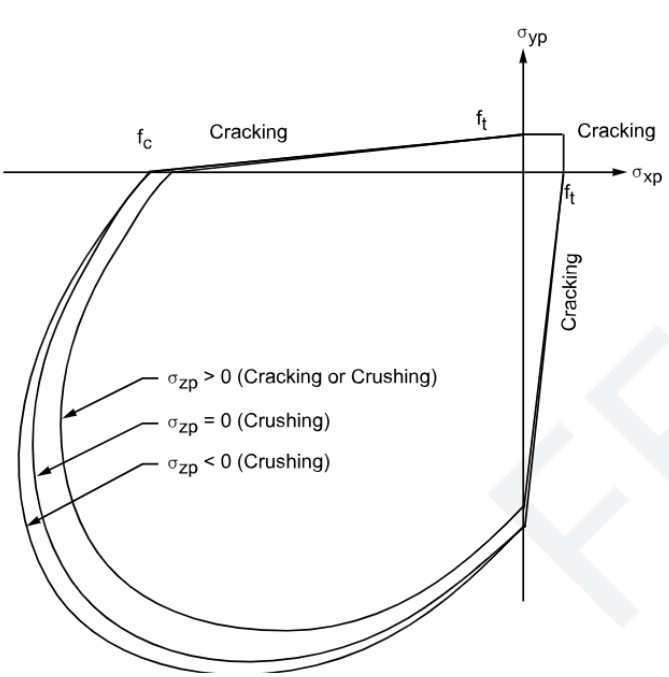

Figure 23 Failure Surface in Principal Stress Space with Nearly Biaxial Stress[8]

No.	Parameter	Symbol	Value	Unit
1	Elastic modulus	E	3.20×10^9	Pa
2	Poisson's ratio	ν	0.15	–
3	Open shear transfer coefficient	β_o	0.2	–
4	Closed shear transfer coefficient	βc	0.2	–
5	Tensile strength	ft	0.36×10^6	Pa
6	Compressive strength	fc	6.32×10^6	Pa
7	Cohesion	c	0.6×10^6	Pa
8	Friction angle	φ	36	°
9	Dilation angle	ψ	0	°

Table 3 William-Warnke model parameter values

The William-Warnke material model, which ANSYS uses material model for concrete, is only compatible with solid 65-element type. It shows a high degree of mesh sensitivity and frequently fails to converge in nonlinear analysis, as evidenced by the results presented below.

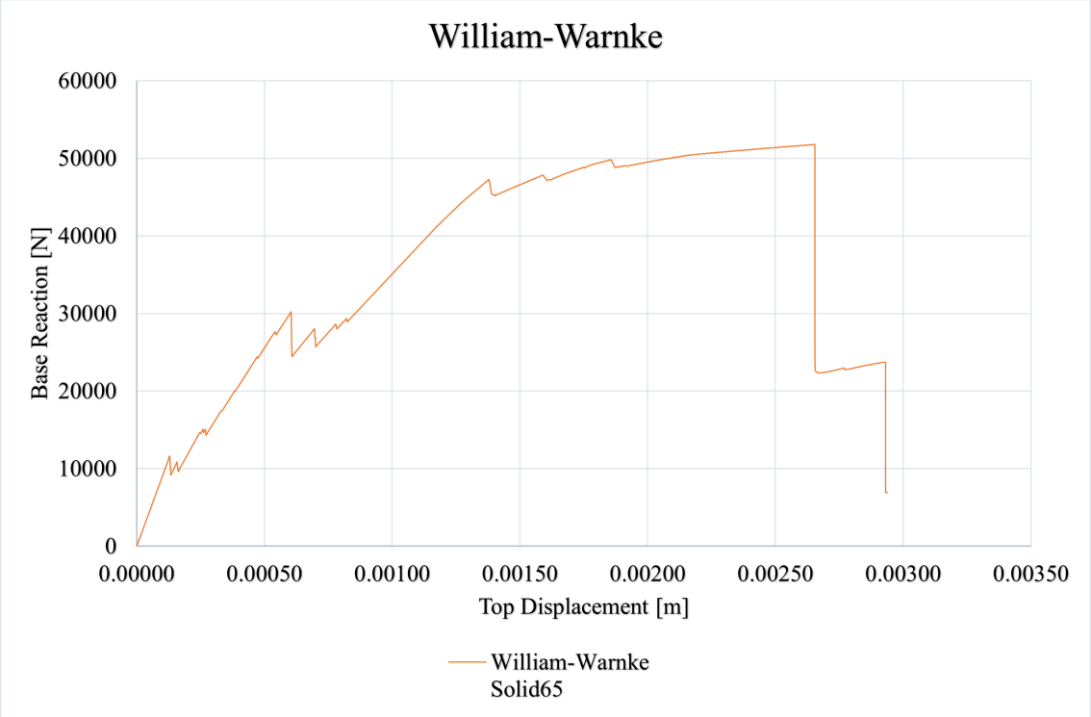

Figure 24 Capacity Curve of the shear wall for W-W model

2.3.3 Drucker-Prager failure criteria

The Drucker–Prager model was tested in this work due to its ability to represent pressure-dependent strength in brittle materials such as rock, soil, concrete, and masonry. The failure surface is the smooth form of Mohr-Columb failure surface which in the 3D plane has a shape of cone. Drucker-Prager model is used to model frictional material that has higher compressive strength and lower tensile strength. The failure surface will determine whether the material is yielded or failed under which state of stress [8].

The difference between M-C [Mohr-Columb] and D-P [Drucker-Prager] in the measurement is between 0.6 to 3.0 of M-C and only in some specific value of angle friction these two give the same result [11].

The tension and tension-compression Drucker-Prager yield surface is given by:

$$(f_{\mathrm{DP},t} = \frac{\sigma_e}{\sqrt{3}} + \beta_t \sigma_m - \sigma_{Y_t}) \quad [8]$$

where β_t and σ_{Y_t} are constants defined by the uniaxial tensile strength f_t and uniaxial compressive strength f_c:

$$(\beta_t = \frac{\sqrt{3}(f_c\Omega_c - f_t\Omega_t)}{f_c\Omega_c + f_t\Omega_t}), \quad (\sigma_{Y_t} = \frac{2f_c\Omega_c f_t\Omega_t}{\sqrt{3}(f_c\Omega_c + f_t\Omega_t)}) \qquad [8]$$

Ω_c and Ω_t are hardening/softening functions in compression and tension, which depend on the stress and hardening variables. To combine the yield surface with the tension-failure surface to limit material strength in tension [8].

$$f_R(\boldsymbol{\sigma}) = \sigma_m + \frac{2}{3}\sigma_e \sin(\theta + 120°) - T \text{ [8]}$$

Where T is the tensile strength of the material.

For compression loading, the D-P yield surface is:

$$f_{DPc} = \frac{\sigma_e}{\sqrt{3}} + \beta_c\sigma_m - \sigma_{Yc}\Omega_c [8]$$

Where,

$$\beta_c = \frac{\sqrt{3}(f_b - f_c)}{2f_b - f_c}, \qquad \sigma_{Yc} = \frac{f_b\, f_c}{\sqrt{3}(2f_b - f_c)} [8]$$

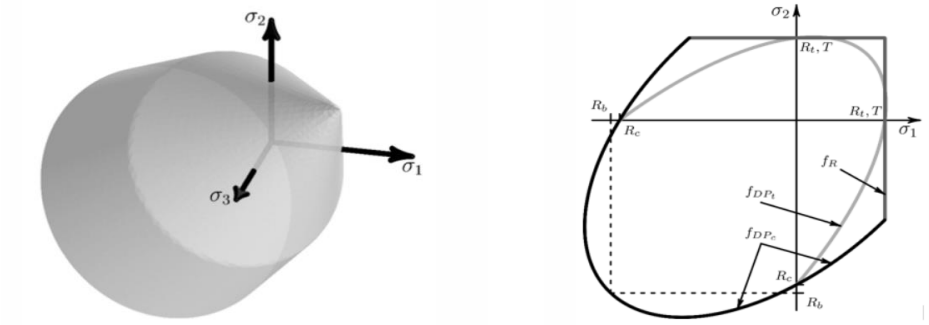

(a) (b)

Figure 25 (a) Composite Surface with Drucker-Prager Compression and Drucker-Prager Tension Yield Surfaces, (b) 2D Yield Surfaces Showing Drucker-Prager and Rankine Surfaces [8]

For D-P model we need to define three parameters including uniaxial compressive strength (fc), uniaxial tensile strength (ft), and biaxial compressive strength (fb). The D-P model has the possibility to define the hardening, softening and dilation [HSD Model] behavior of material. In ANSYS there are different HSD models which are not only used in D-P models but also on the other models that we will discuss next.

No.	Parameter	Symbol	Value	Unit
1	Elastic modulus	E	3.20×10^9	Pa
2	Poisson's ratio	ν	0.15	–
3	Compressive strength	fc	6.32×10^6	Pa
4	Tensile strength	ft	0.32×10^6	Pa
5	Biaxial compressive strength	fb	7.584×10^6	Pa
6	Tensile dilation parameter	δt	0.0	–
7	Compressive dilation parameter	δc	0.0	–
8	Inelastic strain at compression peak	κcm	$0.0025 - Rc/E = 0.000525$	–
9	Inelastic strain at compression residual	κcr	0.0025	–
10	Damage variable at compression initiation	ωci	0.33	–
11	Damage variable at compression residual	ωcr	0.10	–
12	Inelastic strain at tension residual	κtr	0.0005	–
13	Damage variable at tension residual	ωtr	0.20	–

Table 4 D-P model parameter values

The result of the D-P failure is slightly higher than the expected value because the failure surface of the D-P, does not include the third invariant of the stress deviator, called the Lode angle. As the failure criteria have been described, the D-P uses only two stress invariants: the first, related to hydrostatic stress, and the second, related to shear stress [8].

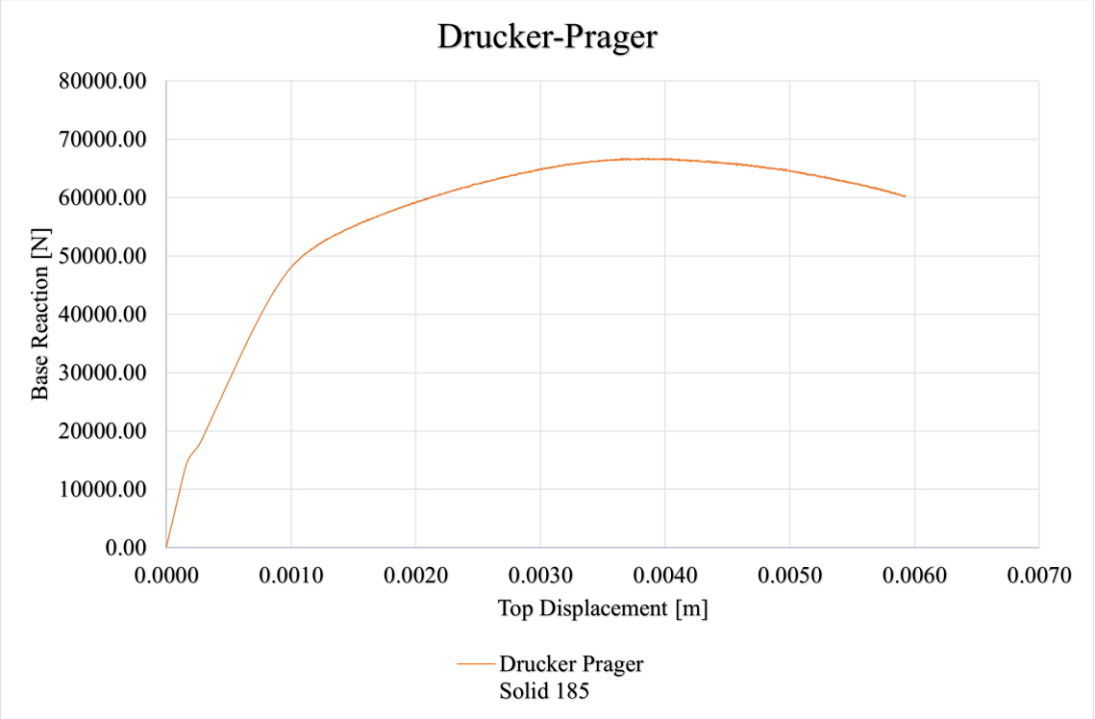

Figure 26 Capacity Curve of the shear wall for D-P model

2.3.4 Menetrey-William Failure Criteria

The Menetrey-Willam constitutive model is based on the Willam-Warnke yield surface and depends on three independent invariants of the stress tensor. This failure criterion, like the Willam-Warnke surface, shares notable similarities with the Mohr-Coulomb surface; however, it lacks the sharp edges that can complicate the Mohr-Coulomb surface stress solution. It also shares some characteristics with the Drucker-Prager model and can be used to model similar materials. However, the Menetrey-Willam model is generally considered superior for simulating the behavior of bonded aggregates, such as concrete [8].

The yield surface in Haigh-Westergaard stress coordinates is given by:

$$f_{MW} = \frac{c_2}{c_3}\left[\sqrt{2}\,\xi + r\rho\right] + \rho^2 - \frac{1}{c_3} \qquad [8]$$

Where c_2 and c_3 are functions of the material parameters and the hardening softening functions

$$c_2 = \frac{1}{\sqrt{6}}\left[\frac{1}{\bar{f}_c} - \frac{1}{\bar{f}_b} + \frac{\bar{f}_b - \bar{f}_t}{\bar{f}_c^2}\right], \qquad c_3 = \frac{3}{2}\frac{1}{\bar{f}_c^2} \qquad [8]$$

And

$$r = \frac{4(1-e^2)\cos^2\theta + (2e-1)^2}{2(1-e^2)\cos\theta + (2e-1)\sqrt{4(1-e^2)\cos^2\theta + 5e^2 - 4e}} \text{ [8]}$$

$$e = \frac{1+\epsilon}{2-\epsilon} \quad , \quad \epsilon = \frac{\overline{f_t}}{\overline{f_b}} \frac{\overline{f_b^2} - \overline{f_c^2}}{\overline{f_c^2} - \overline{f_t^2}} \quad \text{[8]}$$

The Haigh-Westergaard stress coordinates are:

$$\xi = \frac{1}{\sqrt{3}} I_1 \quad , \quad \rho = \sqrt{2J_2} \quad , \quad \cos 3\theta = \frac{3\sqrt{3}}{2} \frac{J_3}{\sqrt{J_2^3}} \quad \text{[8]}$$

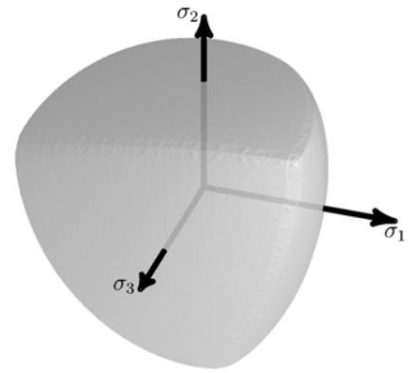

Figure 27 Yield Surface for the Menetrey-Willam Model [8]

The Menetrey-William (M-W) model requires the same parameters as the Drucker-Prager (D-P) model: uniaxial compressive strength, biaxial strength, and tensile strength of masonry. The M-W model also allows for the definition of the Hardening-Softening-Dilation (HSD) model, using the same parameters as the D-P model. The softening behavior in the M-W model, similar to the D-P model, can be specified as either linear or exponential [8]. In this study, only the linear softening model was tested on the benchmark, as shown in the figure below.

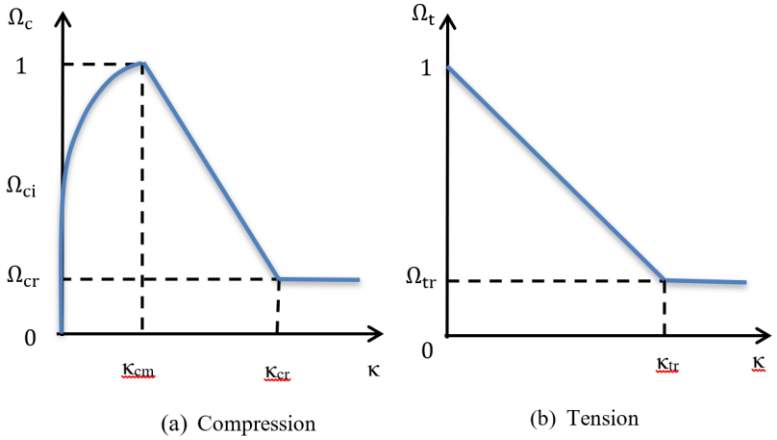

Figure 28 Linear Softening in (a) Compression and (b) Tension

No.	Parameter	Symbol	Value	Unit
1	Elastic modulus	E	3.20×10^9	Pa
2	Poisson's ratio	ν	0.15	–
3	Compressive strength	fc	6.32×10^6	Pa
4	Tensile strength	ft	0.36×10^6	Pa
5	Biaxial compressive strength	fb	7.2×10^6	Pa
6	Dilatancy angle	φ	0	°
6	Inelastic strain at compression peak	κ_{cm}	0.0025−fc/E = 0.000525	–
7	Inelastic strain at compression residual	κ_{cr}	0.0025	–
8	Damage variable at compression initiation	ω_{ci}	0.33	–
9	Damage variable at compression residual	ω_{cr}	0.10	–
10	Inelastic strain at tension residual	κ_{tr}	0.0005	–
11	Damage variable at tension residual	ω_{tr}	0.20	–

Table 5 M-W model parameter values

Figure 29 Capacity Curve of the shear wall for M-W model

2.3.5 Coupled Damage-Plasticity Microplane Model

The Coupled Damage–Plasticity Microplane Model (CDPMP) is a constitutive model in which the material behavior is described on a set of planes with different orientations, called microplanes. On each plane, an independent stress–strain relationship is defined. The macroscopic response is then obtained by combining the contributions of all microplanes. This concept is particularly suitable for quasi-brittle materials, such as masonry and concrete, whose behavior is dominated by cracking, softening, and direction-dependent stiffness degradation [8], [12].

In the microplane framework, direction-dependent stiffness degradation is represented through damage laws defined on each potential failure plane, resulting at the macroscopic level in an anisotropic damage response [8], [12].

Directly modeling anisotropic damage in a classical 3D continuum is complicated, because it requires additional damage variables and results in constitutive equations that are difficult to manage. The microplane model offers a simpler way to represent the same behavior, since the damage is defined directly on the individual planes rather than through complex macroscopic formulations [8].

The microplane theory is based on the assumption that a microscopic free energy Ψ_{mic} can be defined on each plane. The total macroscopic Helmholtz free energy Ψ_{mac} is then obtained by integrating the microscopic contributions over all plane orientations [8]. This relationship is expressed as:

$$\psi^{mac} = \frac{3}{4\pi}\int_{\Omega}\psi^{mic}\,d\,\Omega \quad [8]$$

The $\frac{3}{4\pi}$ factor results from the integration of the sphere of unit radius with respect to the area Ω. The stresses can then be derived by taking the free energy derivative with respect to the strain tensor as:

$$\sigma = \frac{3}{4\pi}\int_{\Omega}\frac{\partial\psi^{mic}}{\partial\varepsilon}\,d\,\Omega \quad [8]$$

For each microplane we can divide the free energy in its volumetric and deviatoric parts.

$$\psi^{mic}(\varepsilon_v, \varepsilon_D) = \psi^{mic}_{vol}(\varepsilon_v) + \psi^{mic}_{dev}(\varepsilon_D) = \frac{1}{2}K^{mic}\varepsilon_v^2 + G^{mic}\varepsilon_D{:}\,\varepsilon_D \; [8]$$

K^{mic} and G^{mic} represents microscopic bulk and shear modulus. We can define microplane stresses as the derivatives of microscopic free energy for the associated

strain comp.

$$\sigma_v := \frac{\partial \psi^{mic}}{\partial \varepsilon_v} = K^{mic}\varepsilon_v, \quad \sigma_D := \frac{\partial \psi^{mic}}{\partial \varepsilon_D} = 2G^{mic}\varepsilon_D \text{ [8]}$$

To do this numerical integration "Discretization" of the sphere is required, discretization is defined as the transition from the microsphere to microplanes, which illustrate the approximate form of the sphere. The numerical integration process utilizes a total of forty-two microplanes. Due to the symmetry of the microplanes (where every other plane has the same normal direction), 21 microplanes are considered.

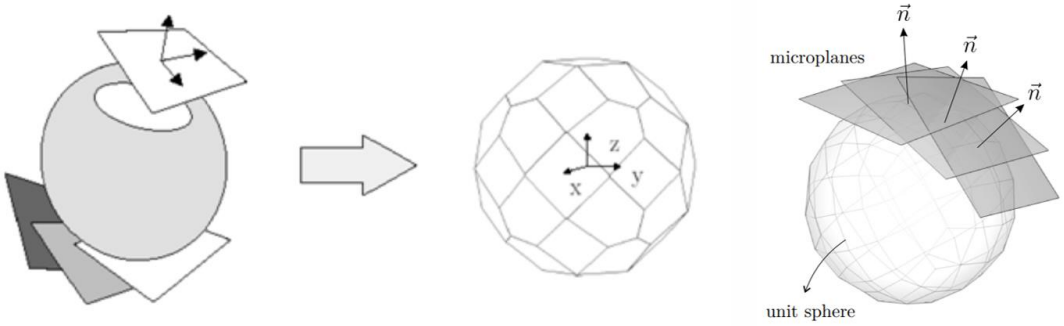

Figure 30 Sphere Discretization by 42 Microplanes and Schematic representation of microplane[8], [13]

The utilization of this model is intended to address the numerical instability and pathological mesh sensitivity that are inherent to strain-softening materials. The model employs an implicit gradient regularization scheme, defined via a nonlocal field, which introduces two additional degrees of freedom at each node. The model's plasticity is characterized by a three-surface microplane Drucker-Prager configuration, encompassing the complete spectrum of potential stress states and facilitating cyclic loading. The damage exhibited by the specimen includes a tension-compression split, which is indicative of the transition of the stress state during cyclic loading [8].

The use of this model is intended to address the numerical instability, and mesh sensitivity that are inherent to strain-softening materials. The model employs an implicit gradient regularization scheme, defined via a nonlocal field, which introduces two additional degrees of freedom at each node. The model's plasticity is characterized by a three-surface microplane Drucker-Prager configuration, encompassing the complete spectrum of potential stress states and facilitating cyclic loading. The

damage exhibited by the specimen includes a tension-compression split, which is indicative of the transition of the stress state during cyclic loading [8].

A smooth Drucker-Prager yield function with tension and compression caps covers the material response under all possible triaxialities. The Drucker-Prager cap model is specific to microplane plasticity, as it uses microplane quantities.

$$f^{mic} = \frac{3}{2}\sigma_D^e \cdot \sigma_D^e - f_1^2 f_c f_t \quad [8]$$

where f_1 is the Drucker-Prager yield function with hardening, f_c is the compression cap, and f_c is the tension cap.

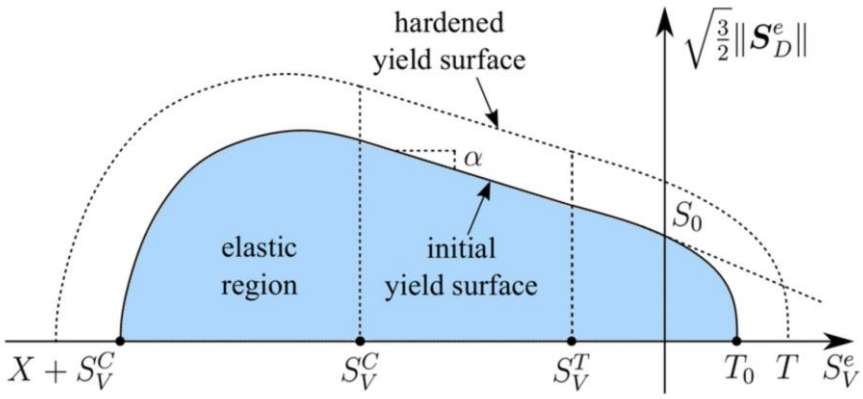

Figure 31 Smooth Three-Surface Microplane Cap Yield Function [8]

To include damage, it is important to consider the initiation of damage and its subsequent evolution, which is different in compression and tension. In the transition from tension to compression states, stiffness decreases due to tensile cracking is recovered through crack closure. Upon transition to tension, however, the damage sustained under compression is retained. For CDPMP model there are 15 parameters that should be defined including elasticity, plasticity, damage, and nonlocal parameters.

No.	Parameter	Symbol	Value	Unit
1	Elastic modulus	E	3.20×10^9	Pa
2	Poisson's ratio	ν	0.15	–
3	Compressive strength	fc	6.32×10^6	Pa
4	Tensile strength	ft	0.32×10^6	Pa
5	Biaxial compressive strength	fb	1.2 × fc = 7.584 ×	Pa

			10^6	
6	Strength/shear bias ratio	Rt	1.0	–
7	Cap hardening parameter	D	0.00	–
8	Cap yield stress	σ_{cv}	$-(2/3) \times fb = -5.056 \times 10^6$	Pa
9	Regularized crack band length	$R_{c,len}$	1.0	m
10	Tensile curvature at damage onset	γ_t	0.00000	–
11	Compressive curvature at damage onset	γ_c	0.00001	–
12	Post-peak tensile slope (damage growth)	βt	20000	–
13	Post-peak compressive slope (damage growth)	βc	15000	–
14	Nonlocal characteristic length (inverse square)	c_{nl}	1000	m^{-2}
15	Nonlocal weight coefficient	m_{nl}	2.5	–

Table 6 CDPMP model parameter values

The coupled damage-plasticity microplane model is a multifaceted model that incorporates plasticity as well as damage evolution in materials. A notable strength of this model is its ability to address the issue of mesh sensitivity, thereby enhancing its overall functionality and relevance to real-world applications. In addition, this model demonstrates a notable capacity to capture strain-softening phenomena during tensile stress, a capability that previous material models lacked. The resultant data from the CDPMP model demonstrates the optimal functionality of the wall under shear stress, accompanied by a softening behavior that ensues once the peak stress is attained.

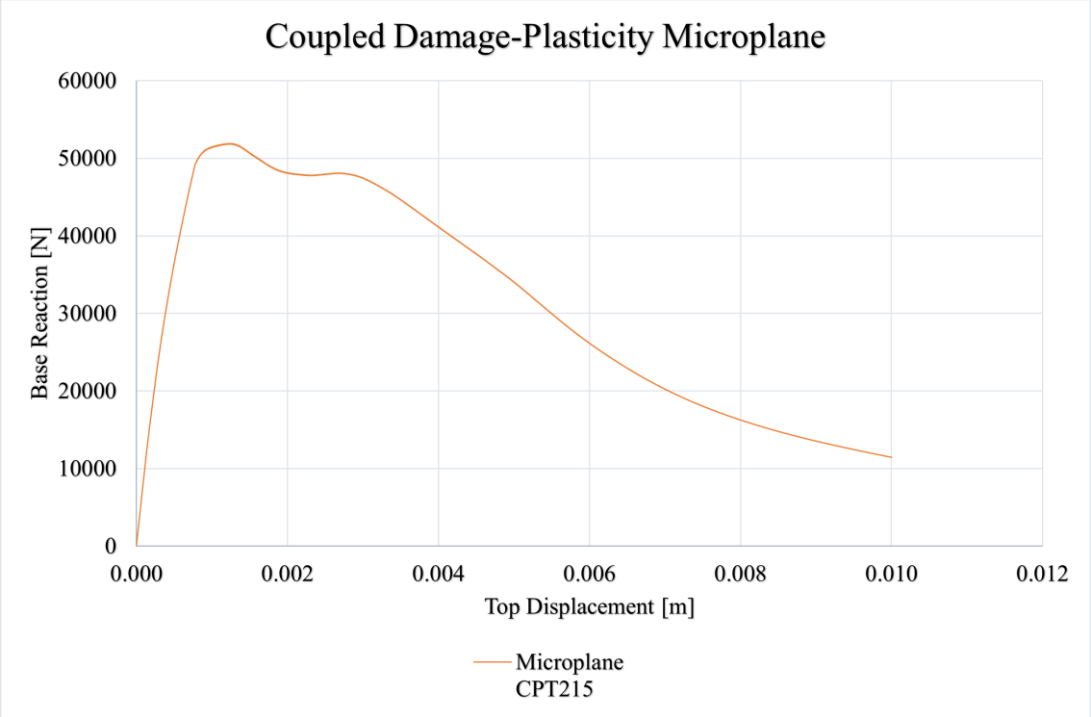

Figure 32 Capacity Curve of the shear wall for CDPMP model

The complexity inherent in the utilization of the CDPMP model comes from the necessity to define too many parameters. These parameters encompass those associated with plasticity and damage, in addition to the parameters previously discussed in the context of other material models. Therefore, it is necessary that the parameters should be carefully calibrated to ensure the attainment of a reliable result.

3.0 Case Study

3.1 Description

The case study examined in this thesis is the valuable bell tower of the S. Antonio Abate church in Monta, Italy, a historical masonry structure which has been undergone several transformations over the centuries. The original church was constructed around the 11th century, and a simpler tower was added during the 16th century. The current bell tower, which replaced the earlier one, was completed in 1814. It has a total height of 17.35 m, a square base measuring 2.7 m × 2.7 m, and an average wall thickness of approximately 0.57 m [1]. The structure is composed of brick masonry and exhibits irregularities and local discontinuities typical of historical constructions.

Figure 33 S. Antonio Abate church and the bell tower *[1]*

3.2 Numerical model description

The bell tower has been previously studied for structural parameters identification and calibration purposes. A detailed finite element model of the structure was developed in ANSYS, based on the available geometric and material information. Two main configurations of the model were defined: a theoretical intact state, representing the

structure without visible damage or cracks, and a damaged state, in which pre-existing cracks and material degradation were explicitly modeled. The nonlinear material model is applied to the intact model of the bell tower for increasing the computational efficiency of the analyses. In the model of bell tower a mix of 2D and 3D elements is used. Specifically, the façade was modeled with 8-node solid elements, each node possessing three degrees of freedom. The rigid floor at the top of the tower and the pyramidal spire of the roof were modeled with 4-node elements, each possessing six degrees of freedom. The part of the bell tower attached to the building of the church is modeled with series of linear elastic springs [1].

The use of linear elastic springs was adopted to reproduce the semi-rigid interaction between the bell tower and the church building. This modeling approach allows the tower to undergo limited relative movement, avoiding a fully rigid connection that would not represent the actual structural behavior of the interface. The mechanical property of elastic springs are not the same in all directions but depend on the degree of confinement provided by the church walls. For instance, the south-east connection offers greater stiffness along the Y-direction due to stronger contact, whereas the north-west corner provides lower stiffness along the X-direction. The mechanical parameters adopted for the *intact-state finite element model* were derived from the calibrated *damaged-state model* [1].

Parameter	Symbol	Value	Unit	Description
Young's modulus	E	1.03×10^9	Pa	–
Poisson's ratio	v	0.35	–	–
Density	ρ	2241	kg/m³	–
Spring stiffness (Y direction)	$K_{SE,Y}$	5.65×10^6	Pa	Elastic connection to church
Spring stiffness (X direction)	$K_{SE,X}$	5.26×10^5	Pa	Elastic connection to church
Spring stiffness (−X direction)	$K_{NW,-X}$	1.91×10^6	Pa	Elastic connection to church

Table 7 Mechanical and modelling parameter adopted for the intact-state FE model [1]

The compressive strength of the masonry used in the bell tower model was estimated through the empirical relationship suggested by the NTC 2018 code:

$$E = 1000\ f_k \quad [14]$$

where E is the modulus of elasticity and f_k is the characteristic compressive strength of the masonry.

The mechanical properties, including compressive strength, tensile strength, and biaxial compressive strength are adopted for the masonry are summarized in Table 8. Since direct experimental data were not available for this case study, the values were selected from the literature.

Property	Symbol	Value	Unit	Source / Note
Compressive strength	f_c	1.03×10^6	Pa	Estimated from (E = 1000 fk) (NTC 2018)
Tensile strength	f_t	5.16×10^4	Pa	Typical ratio ($f_t \approx 0.05\ f_c$) for brick masonry [2]
Biaxial compressive strength	f_b	1.24×10^6	Pa	Approx.($f_b \approx 1.2\ f_c$) [3]

Table 8 Mechanical properties of the bell tower

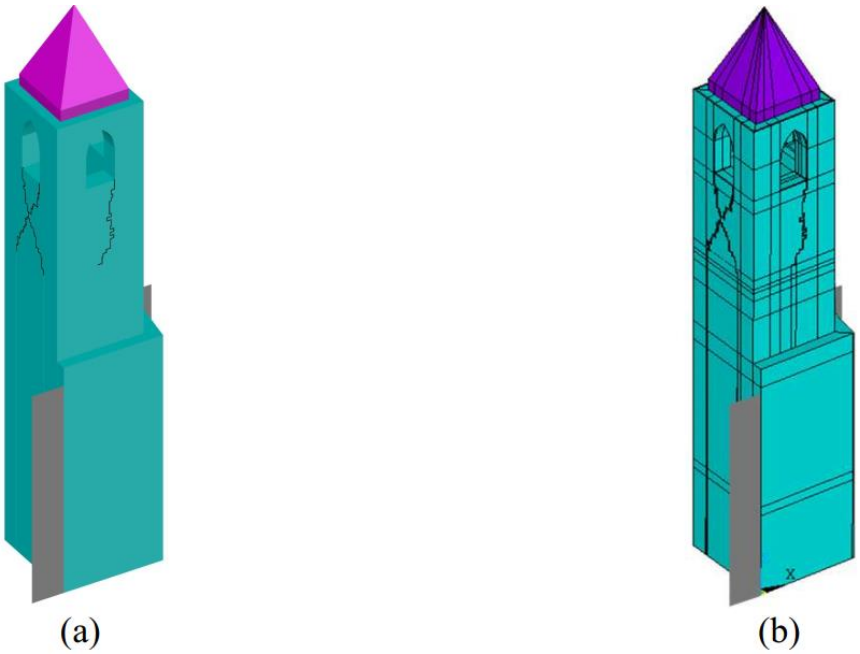

Figure 34 Geometric (a) and numerical FE (b) model of the bell tower of the old parish church of S. Antonio Abate in its damaged condition.[1]

The original finite element model of the bell tower was extremely detailed and complex. Even in the intact state configuration, the cracks were explicitly modeled as separate volumes, which made the geometry highly fragmented and difficult to mesh. In addition, the presence of curved openings and irregular shapes further increased the number of small elements required for an accurate discretization, resulting in an excessively dense mesh and high computational demand.

To make the model simpler for nonlinear analysis, the geometry was simplified by removing the explicitly modeled cracks and merging small volumes into larger ones, and the curved openings were also replaced with straight profiles to facilitate meshing. These modifications preserved the overall geometry and stiffness of the tower while allowing the generation of a coarser mesh suitable for nonlinear analysis.

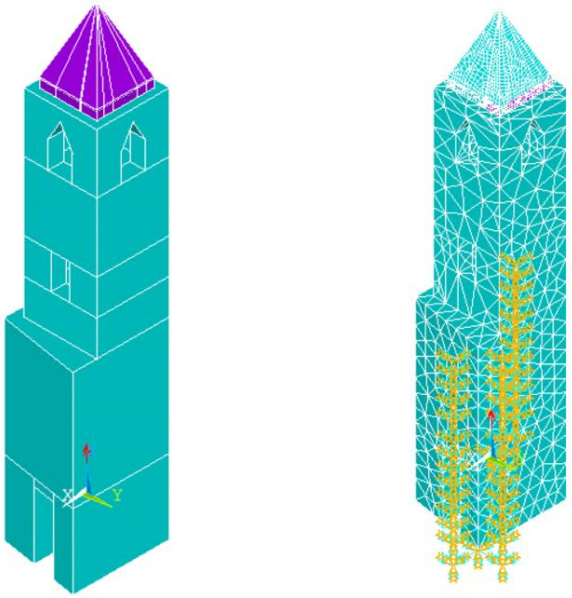

(a) (b)

Figure 35 (a) Simplified numerical FE (b) mesh size of the model

In the previous section of the thesis, different nonlinear material models were tested and calibrated on a simplified masonry wall specimen to evaluate their ability to reproduce the nonlinear response of masonry. Those tests showed satisfactory convergence and realistic results due to the simplicity of the geometry and limited number of elements. However, when the same material models were applied to the bell tower, the high geometric complexity and large mesh size led to convergence difficulties in most cases.

Among the tested material models, only the coupled damage-plasticity microplane

model successfully completed the full nonlinear analysis without convergence issues. With the assigned material model, the global response of the tower was then evaluated through a nonlinear static analysis to obtain the capacity curve and identify the most damaged regions of the structure.

3.3 Static nonlinear analysis

The nonlinear static analysis, also known as a static nonlinear analysis, is an incremental iterative analysis in which the structure is pushed up to a predetermined displacement threshold or until it reaches its ultimate deformation capacity. The monitored parameters during the analysis are in most cases the shear at the base of the structure

and the displacement of a control point, for this structure the one edge node has been chosen. The representation of the base-shear versus the top displacement provides what is called the structure capacity curve [15].

The static nonlinear analysis was performed by applying a monotonic lateral displacement to the top nodes, located at a height of 14.55 m where the solid elements terminate. Each analysis began with a gravity loading phase to establish the initial stress state, followed by the application of a displacement-controlled load up to 0.14 m. The corresponding base reaction was recorded at each increment to derive the structure's capacity curve.

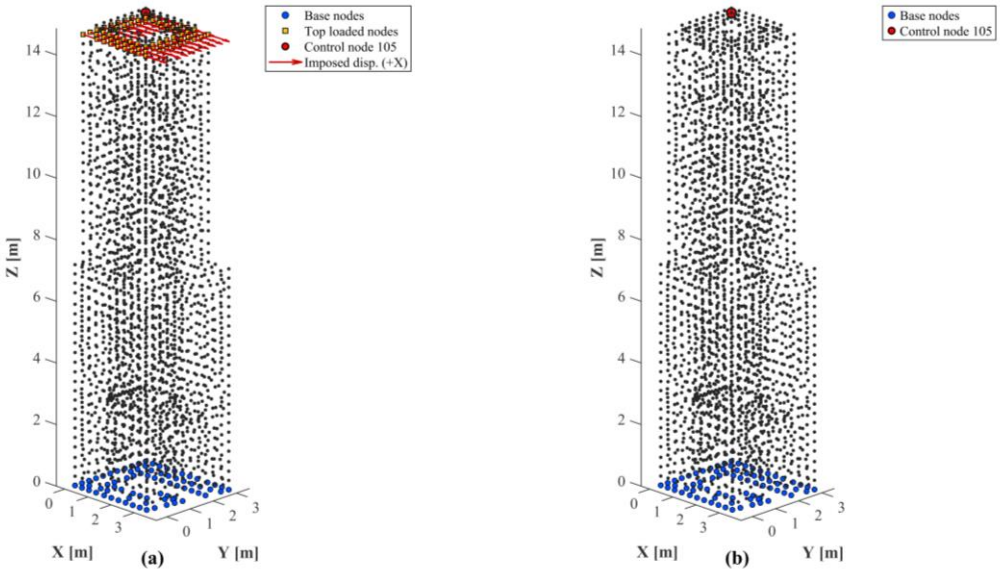

Figure 36 Configuration of the static nonlinear analysis (a) the application of the monotonic displacement loading (b) the control nodes

It is important to note that the base reaction is governed not only by the mechanical properties of the material but also by the mesh size. This effect arises from two main factors. First, coarse meshes cannot properly capture local stress gradients and strain localization, which leads to an unrealistically stiff global response. Refining the mesh improves the representation of cracking and damage, producing smoother and more realistic capacity curves. Second, the boundary condition which is assigned to the bell tower in the region of contact with church building by elastic springs, which depends on the mesh density. A finer mesh introduces more springs, allowing a more continuous load transfer along the interface; as a result, a portion of the lateral load is absorbed by the springs, and the base reaction slightly decreases. This trade-off between physical accuracy and computational cost was a key aspect considered in the static nonlinear analysis.

After completing the numerical setup, the static nonlinear analyses in the two orthogonal directions were performed to capture the structure's anisotropic response. The capacity curves obtained from these simulations are reported below and clearly show directional variations in strength and stiffness. It should be mentioned that the following results refer to the analysis of the model with a 0.5 m mesh size, using the mechanical properties of the bell tower reported previously.

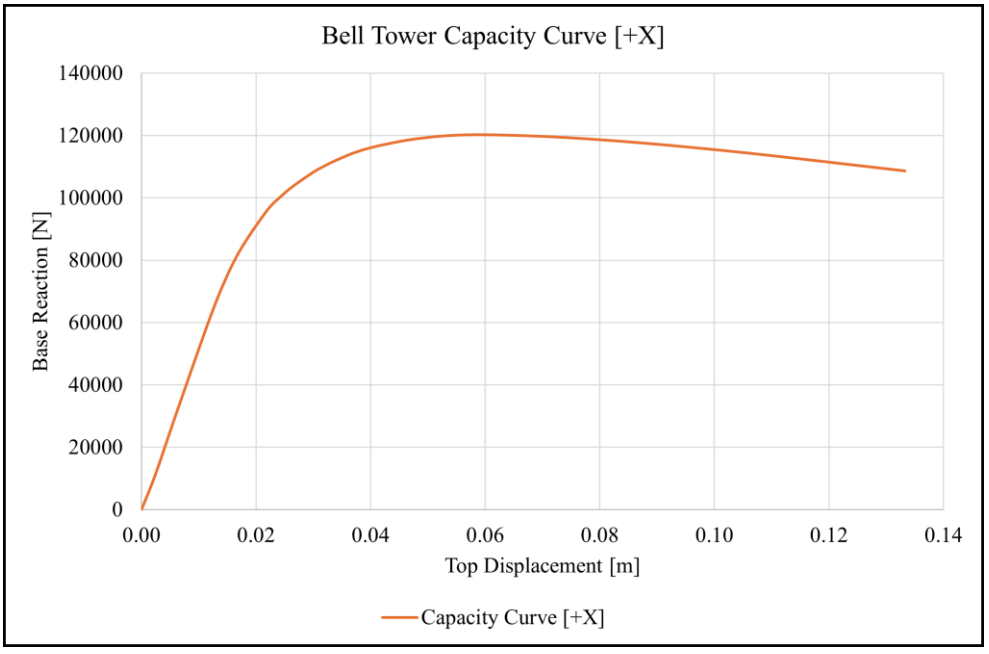

Figure 37 Bell tower capacity curve [+x]

In the +X (east) direction, the analysis shows the highest lateral resistance. This is mainly because along the eastern side there is no large opening, and the wall has continuous geometry. In addition, the stiffness of the springs in the east direction is lower compared to the west, which results in a higher base-shear capacity.

In the +Y (south) direction, the tower shows lower strength compared to the X direction with a peak resistance of around 72,000 N followed by steep post peak reduction. The first cause of this weaker response is the high stiffness of the spring in the Y direction, which transfers a significant portion of the horizontal load to the church, reducing the reaction measured at the tower base. Furthermore, the presence of a large opening on the southern façade decreases the continuity and lateral resistance of the wall, contributing to the reduced capacity in this direction.

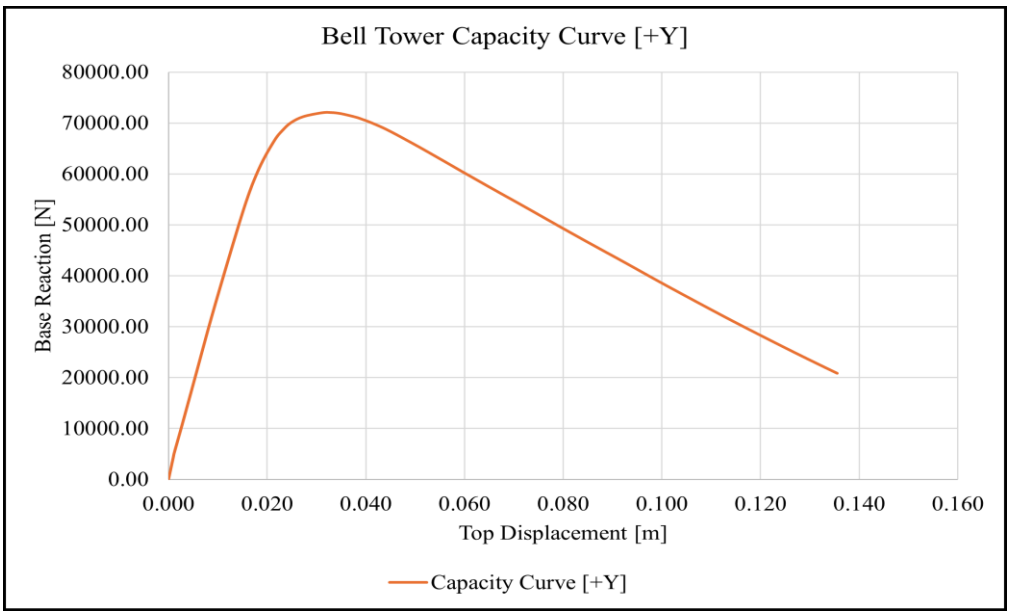

Figure 38 Bell tower capacity curve [+y]

The ductility factors (μ) which expresses how much inelastic deformation the equivalent SDOF system can sustain after yielding. In the N2 method, ductility is computed as the ratio between the ultimate displacement, taken at 85% of the maximum strength, and the yield displacement obtained from the equal energy bilinearization:

$$\mu = \frac{du}{dy}$$

Where, du is the ultimate displacement and dy is the yield displacement. To

determine *dy* the original SDOF capacity curve is idealized into a bilinear form which is followed by the approach described by NTC 2018 [14].

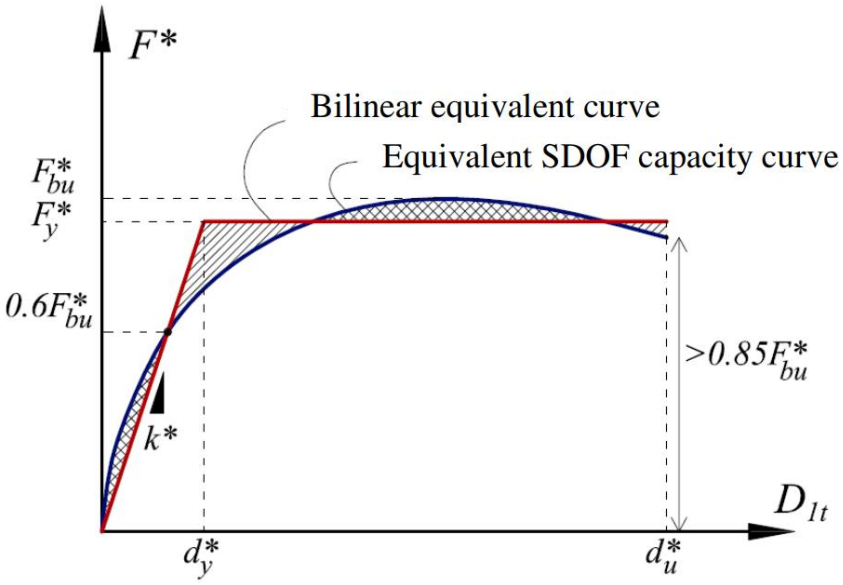

Figure 39 Bilinear equivalent curve and equivalent SDOF capacity curve

Bilinear curve for X direction			**Bilinear curve for Y direction**		
Parameter	Value	Unit	Parameter	Value	Unit
F_{bu}	120285.61	N	F_{bu}	72020.644	N
0.6 F_{bu}	72171.367	N	0.6 F_{bu}	43212.386	N
0.85 F_{bu}	102242.77	N	0.85 F_{bu}	61217.547	N
F_y	110149.55	N	F_y	68246.177	N
0.6Fu disp	0.014	m	0.6Fu disp	0.014	m
d_y	0.022	m	d_y	0.0192	m
du	0.13	m	du	0.0577	m
μ	5.731	-	μ	2.997	-

Table 9 Bilinear curve parameter and ductility factor

The ductility factor coming from the bilinear curves shows a noticeable difference in behavior in two directions. Along X direction the ductility factor is much higher than Y direction.

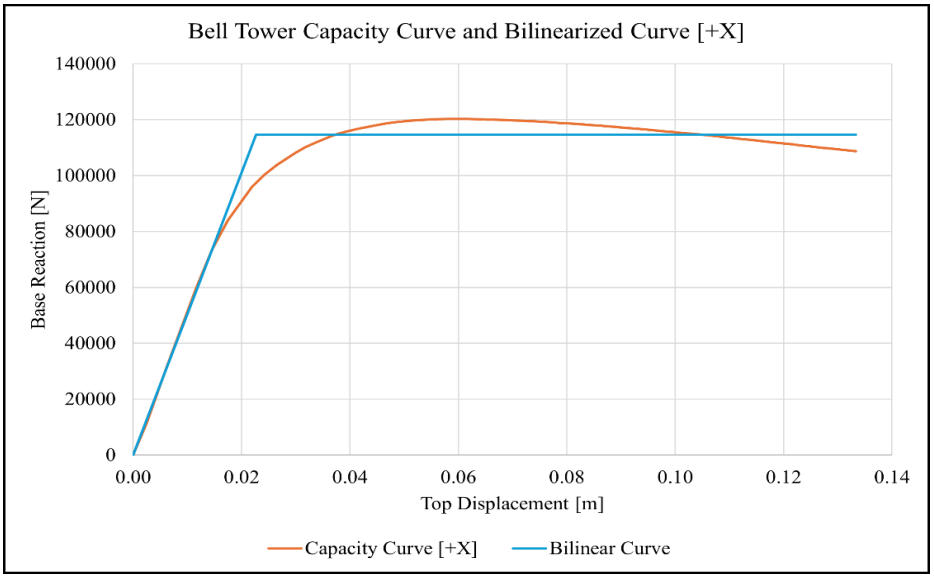

Figure 40 Bell tower capacity curve and bilinearized curve [+X]

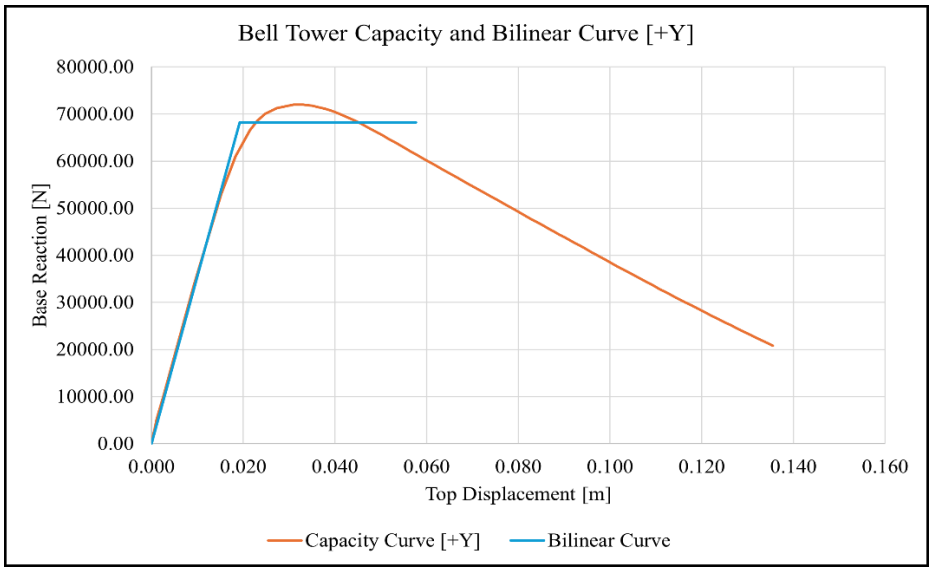

Figure 41 Bell tower capacity curve and bilinearized curve [+Y]

The static nonlinear analysis also provides essential information on the damage distribution in the tower, obtained from the distribution of equivalent plastic strain (EPS) at the final step of the simulation. EPS is a reliable indicator of masonry damage, as it highlights the zones where irreversible deformation, cracking in tension, and crushing in compression take place [8].

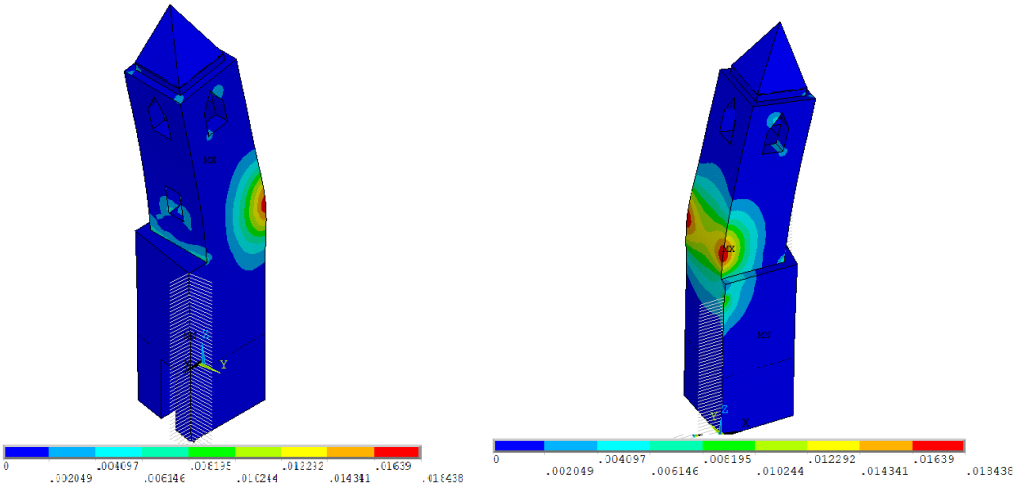

Figure 42 Nodal solution for distribution of equivalent plastic strain (EPS)

These results clearly show that damage in the bell tower is highly localized, forming in specific regions such as corners, discontinuities and openings where the stress concentration is high due to the brittle behavior of masonry. In contrast, large portions of the structure show zero plastic strain which means they remain practically elastic throughout the analysis.

Running a fully nonlinear material model over the entire structure comes with a significant computational cost. With the current mesh size of 0.5 m, a single static nonlinear analysis requires almost two hours of computation. If the mesh is refined to 0.1 m, the number of nodes and elements would increase significantly, and so does the analysis time. This makes fine-mesh nonlinear modelling impractical, especially when multiple analyses are needed for calibration or parametric studies.

Since the inelastic response develops only in specific locations, as highlighted previously, it is reasonable to model nonlinearity only in those zones while keeping the remaining parts elastic. This strategy still reproduces the same structural behavior as the fully nonlinear model, but with a much lower computational cost.

4.0 Surrogate Model

A surrogate model is an approximation of a complex numerical model that can reproduce its response using a set of inputs and outputs data, by learning the relationship between them, with a much lower computational effort [16]. The concept is that the surrogate learns how the model behaves based on the given data, and once this relationship is learned, it can reproduce the same behavior without running the full analysis. In our case, performing a complete nonlinear analysis every time requires a lot of time, while a trained surrogate model can provide the same result almost instantly.

In this work, the surrogate is trained using the material parameters (f_c, f_t) together with the spatial coordinates of each node as inputs, while the output corresponds to the maximum equivalent plastic strain obtained from nonlinear simulations in ANSYS. Since the quality of any surrogate model depends directly on the data used for training, the first step is to construct a reliable and sufficiently rich dataset.

4.1 Dataset creation

In this thesis a surrogate model was implemented using the data generated from the nonlinear static analyses. The model was trained directly on the outputs of 200 simulations with different mechanical properties of masonry, allowing it to capture the relationship between the material strengths and the resulting damage distribution. In the following section, the structure of this surrogate model and the training procedure used in this thesis are described.

Number of simulations	Mesh levels	Nodes per mesh	Damage output	Input parameters	Output size
200	Coarse, Medium, Fine	642 1128 2658	EPEQ_max	(X, Y, Z, fc, ft)	Number of nodes × 200

Table 10 General description of the data set

After each nonlinear analysis, the nodal coordinates together with the corresponding equivalent plastic strain were extracted from ANSYS. These data are then used to build the dataset for training the surrogate model.

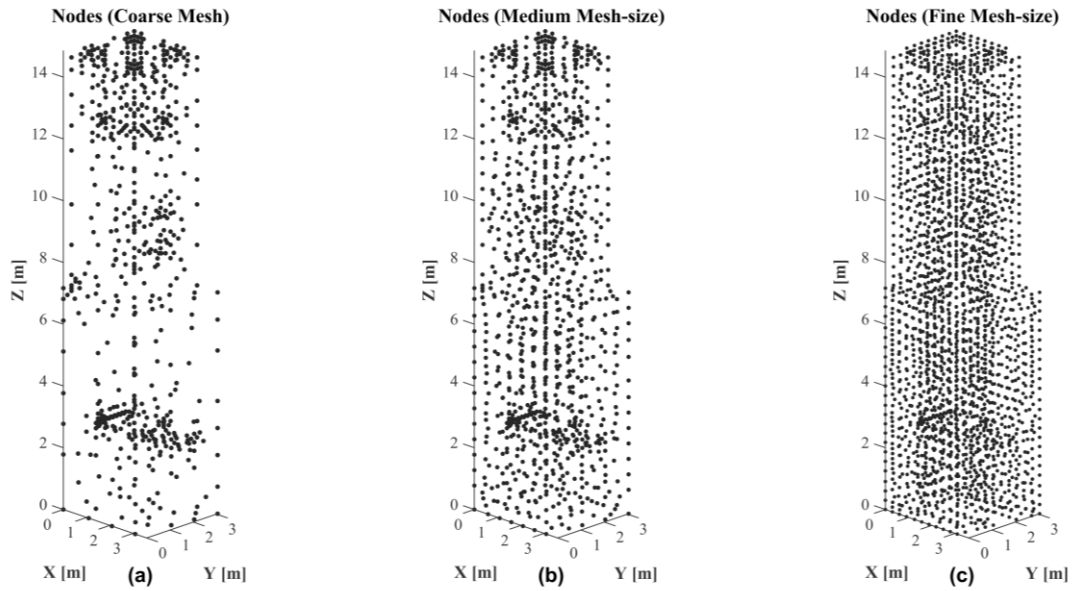

Figure 43 Node distribution density of the model (a) coarse mesh size (b) medium mesh size (c) fine mesh size

To understand how much information each simulation provides, it is useful to look at the three mesh sizes adopted for the bell tower and how they affect the number and distribution of nodes. With the coarse mesh (1.0 m), the number of nodes is very limited and the spacing between them is large, which reduces the level of detail in the damage distribution. Moving to the medium mesh (0.5 m), the node distribution becomes more regular and denser, offering a better description of the structural response. The fine mesh (0.3 m) provides the most detailed representation and is the closest to what we would ideally use. However, the computational time increases significantly as the mesh becomes finer, and running hundreds of nonlinear analyses on the finest mesh is not feasible.

For this reason, the 200 analyses (100 in X and 100 in Y) were not all performed with the same mesh resolution. In each direction, 50 simulations were carried out with the coarse mesh, 30 with the medium mesh and 20 with the fine mesh. This choice keeps the total computation time reasonable while still giving the surrogate model access to datasets with different mesh quality.

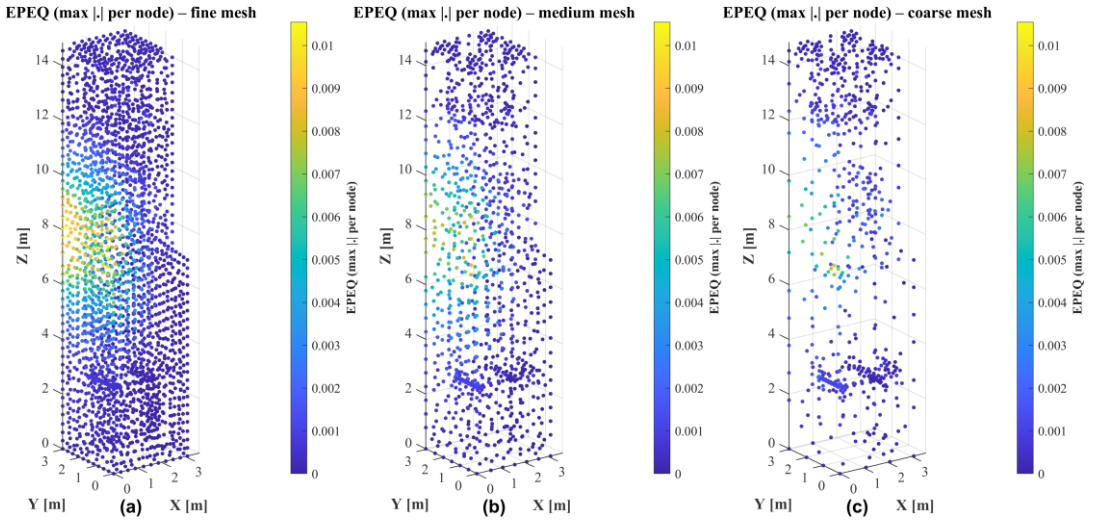

Figure 44 X-direction nodal solution of equivalent plastic strain distribution of the model (a) fine mesh size (b) medium mesh size (c) coarse mesh size

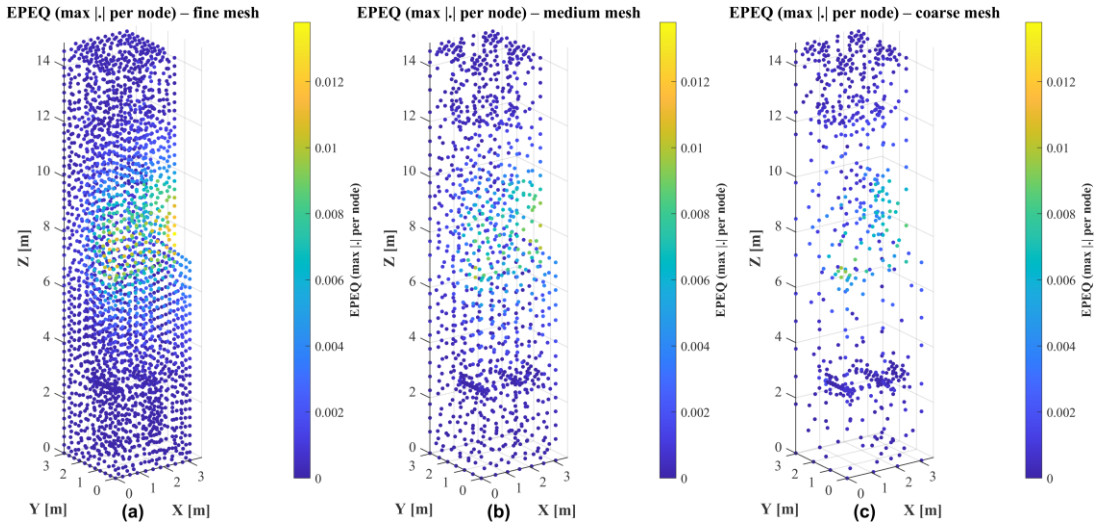

Figure 45 Y-direction nodal solution of equivalent plastic strain distribution of the model (a) fine mesh size (b) medium mesh size (c) coarse mesh size

In addition to the mesh-size variation, the mechanical properties of the masonry were also considered as input variables in the dataset. For each of the 200 analyses, a pair of compressive and tensile strengths (f_c, f_t) was assigned. These values were generated randomly within a realistic interval for the bell tower, using a Gaussian distribution to introduce natural variability in the material parameters. This allows the dataset to cover a wide range of possible strength conditions rather than relying on a single deterministic value. As a result, the surrogate model can learn how different combinations of f_c and f_t influence the structural response.

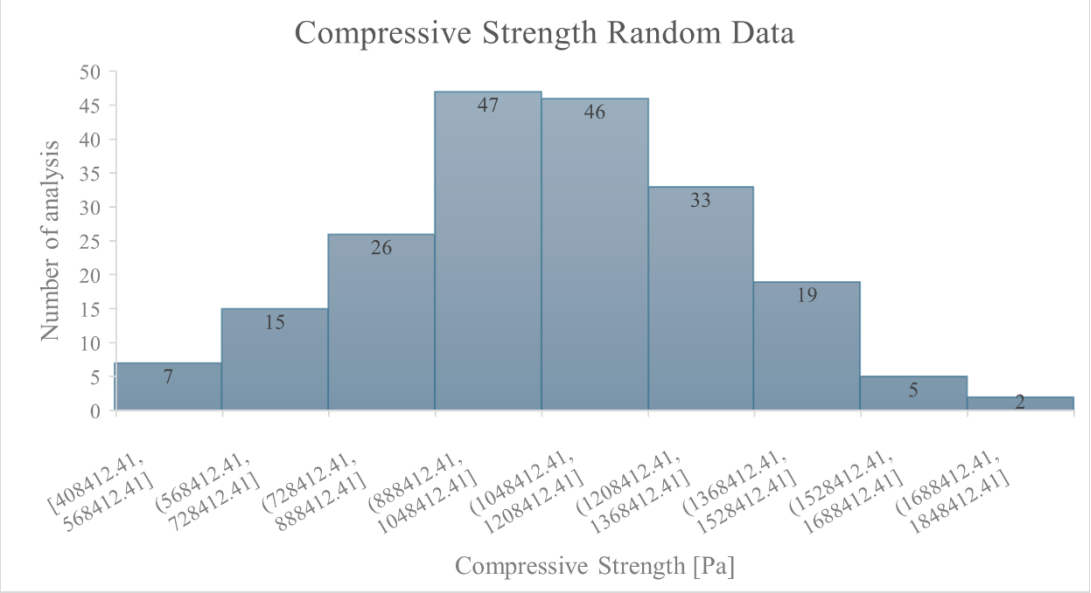

Table 11 Compressive strength random data

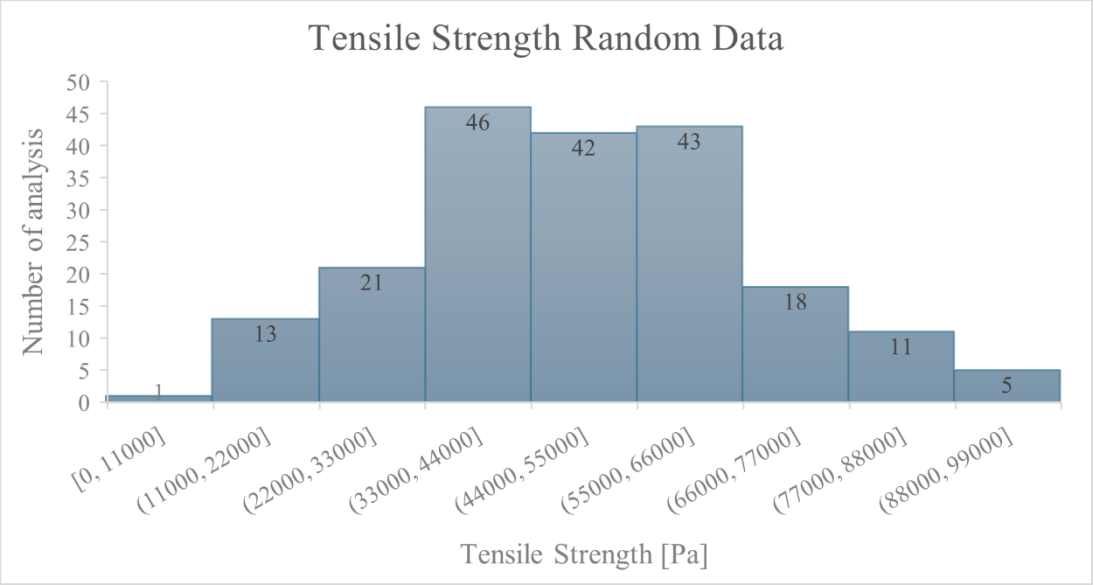

Table 12 Tensile strength random data

The selected ranges, the mean and standard deviation of data are presented below:

Parameter	**Mean**	**Std. Dev.**	**Min**	**Max**	**Original Value**
Compressive strength (*fc*) (Pa)	1,065,517	268,568	408,412	1,721,808	1,032,299
Tensile strength (*ft*) (Pa)	49,846	18,240	0	95,842	51,614

Table 13 Statistical value of mechanical parameter distribution

The resulting dataset combines simulations performed on coarse, medium, and fine meshes, which provides a rich basis for training the surrogate models but also introduces a dependence on mesh resolution. To understand this effect and its influence on the structural response, the next subsection examines the impact of mesh size on the capacity curves.

According to the available data, the analyses have been performed using different mesh sizes, and as discussed earlier, the base reaction is influenced not only by the mechanical properties of the material but also by discretization. This effect becomes evident in the capacity curves obtained from the nonlinear analyses, since these curves are derived solely from the base reaction, excluding the portion of the load carried by the modeled springs. As a result, both the mesh-dependent distribution of forces between the solid elements and the springs affects the magnitude and the shape of the capacity curves. Alternatively, the reaction of the spring nodes could also be included, or the number of springs could be kept consistent across all mesh sizes, but neither of these approaches was used in this thesis, and the analysis focuses exclusively on the base shear–displacement response.

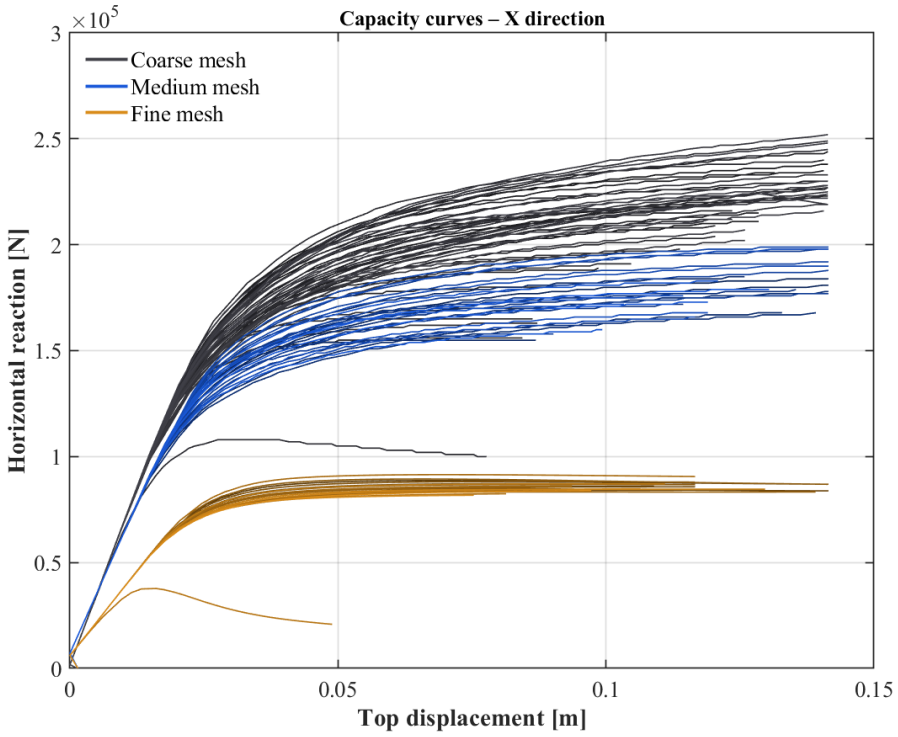

Table 14 100 Capacity Curves for different mesh density x direction

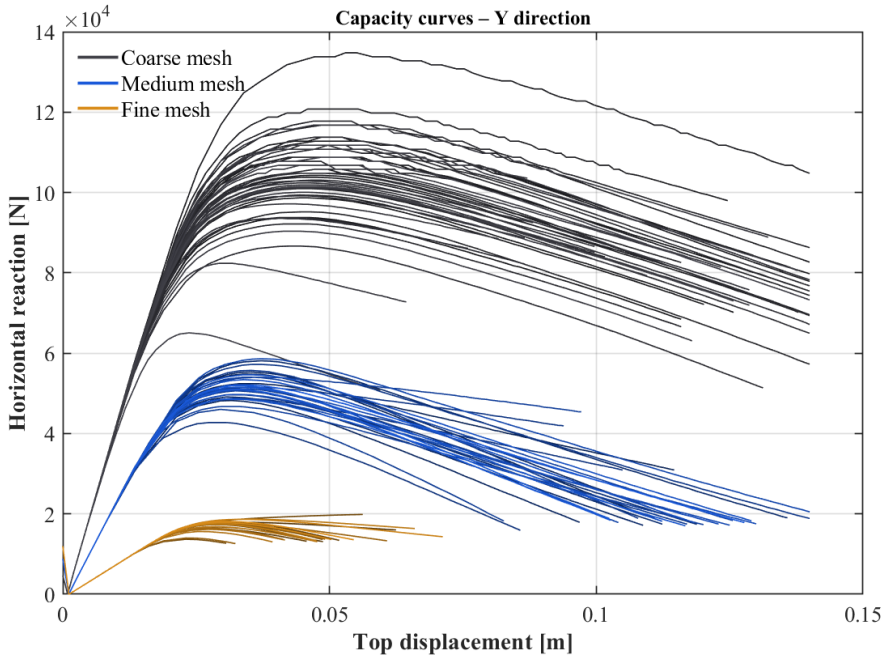

Table 15 100 Capacity Curves for different mesh density y direction

4.2 Training and Validation of the Surrogate Models

Now that the dataset is created, the next step is to make an algorithm capable of learning the relationship between the inputs (X, Y, Z, f_c, f_t) and the resulting damage. For this purpose, Gaussian Process Regression (GPR) was selected as the surrogate modelling technique. GPR is well suited for this kind of problem because it can capture nonlinear trends in the data and provides reliable interpolation even when the samples are not uniformly distributed. In this work, a separate GPR model was trained for each mesh level (coarse, medium and fine) and for both loading directions, resulting in six independent surrogates.

MATLAB's Gaussian Process Regression works by assuming that points which are close to each other in this five-dimensional input space should produce similar strain values. During training, the algorithm automatically adjusts its internal parameters so that this similarity rule matches the behavior observed in the FE data.

Once trained, the surrogate predicts the strain at any new input $\mathbf{x}_*$. The prediction is given by a weighted combination of all the previously observed FE results. The prediction formula used internally by MATLAB is:

where:

$$\hat{y}(x_*) = k(x_*)^\top (K + \sigma_n^2 I)^{-1} y,$$

- **K** is the matrix measuring similarity between all training points,
- $\mathbf{k}(\mathbf{x}_*)$ measures similarity between the new point and the training points,
- **y** contains the FE strain values,
- σ_n^2 is the noise level estimated during training.

This formula tells us that the surrogate prediction is essentially a smart interpolation of the FEM data: the closer a new point is to known data, the stronger its influence. The model also provides a second quantity, the prediction variance, which indicates how confident the surrogate is about the output. This uncertainty estimate is later used when constructing damage indicators and guiding the sampling procedure.

Once the training process was completed, each surrogate model was evaluated through comparison with ANSYS results and through cross-validation to assess its robustness. Several accuracy measures were considered, including error-based metrics (MSE, RMSE, MAE) and the coefficient of determination. These indicators describe both the typical prediction error and also how well the surrogate captures the FE behavior, and they indicate which model configuration offers the most reliable outputs.

Training Performance of Surrogate Models			
Model Name	Train RMSE	Train MAE	Train R2
Coarse X	0.000344	0.000205	0.936676
Medium X	0.000235	0.000140	0.983323
Fine X	0.000316	0.000162	0.980321
Coarse Y	0.000382	0.000220	0.956977
Medium Y	0.000325	0.000176	0.975365
Fine Y	0.000405	0.000201	0.969389
Cross-Validation Performance of Surrogate			
Model Name	Cv RMSE	Cv MAE	Cv R2
Coarse X	0.000364	0.000215	0.929450
Medium X	0.000250	0.000150	0.981106
Fine X	0.000323	0.000177	0.979349
Coarse Y	0.000375	0.000221	0.958735

Medium Y	0.000330	0.000176	0.974591
Fine Y	0.000404	0.000200	0.969470

Overall, the fine-mesh surrogates show the highest accuracy, with R^2 values close to 1.0 and the lowest error measures. Medium-mesh models also maintain a good level of precision, whereas the coarse-mesh surrogates show larger scatters, as expected due to their lower mesh density. Nevertheless, all models demonstrate satisfactory performance for predicting the maximum plastic strain.

The plots below show the comparison between the surrogate predictions and the FE-derived values of max equivalent plastic strain ($EPEQ_{\max}$), which confirms the trends already observed in the performance indicators. The coarse mesh model shows the loose correlation to the finer meshes, with a broader point cloud spread around the identity line. This pattern shows the effect of the lower mesh density, but the behavior of the model still follows the expected trend.

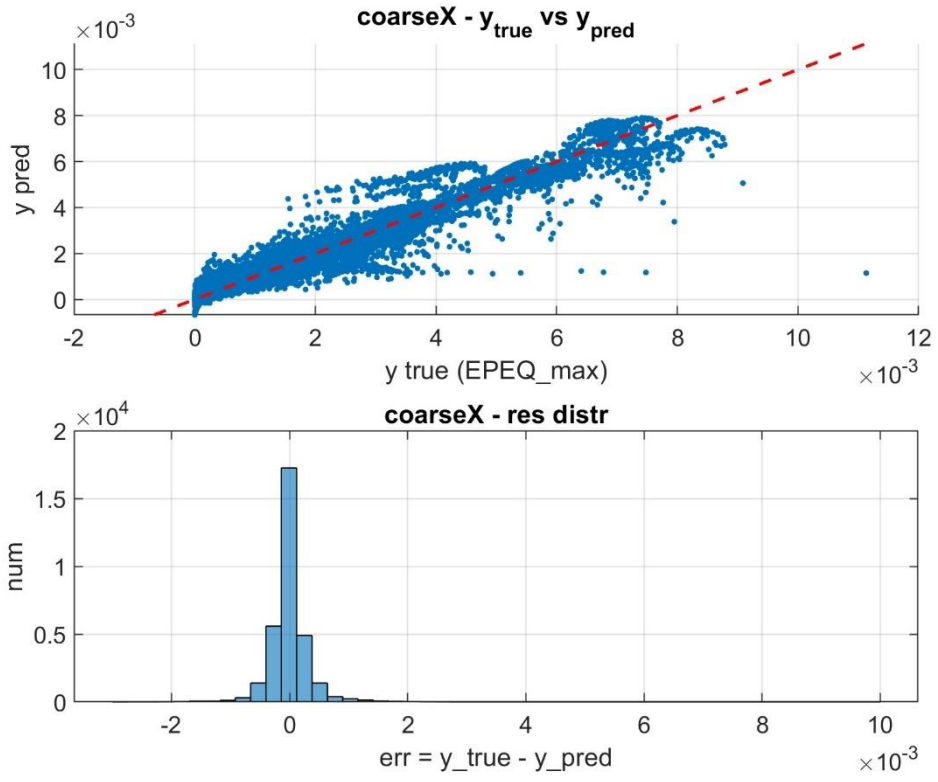

Figure 46 Validation of the surrogate model for the coarse mesh (X direction)

The medium mesh model shows a clearer correlation compared to the coarse one, with a tighter point cloud that aligns more closely with the identity line. This improvement

results from the higher mesh resolution, which allows the model to capture the strain variations more efficiently. At higher strain values, the point cloud diverges slightly from the trend, but the overall behavior remains acceptable.

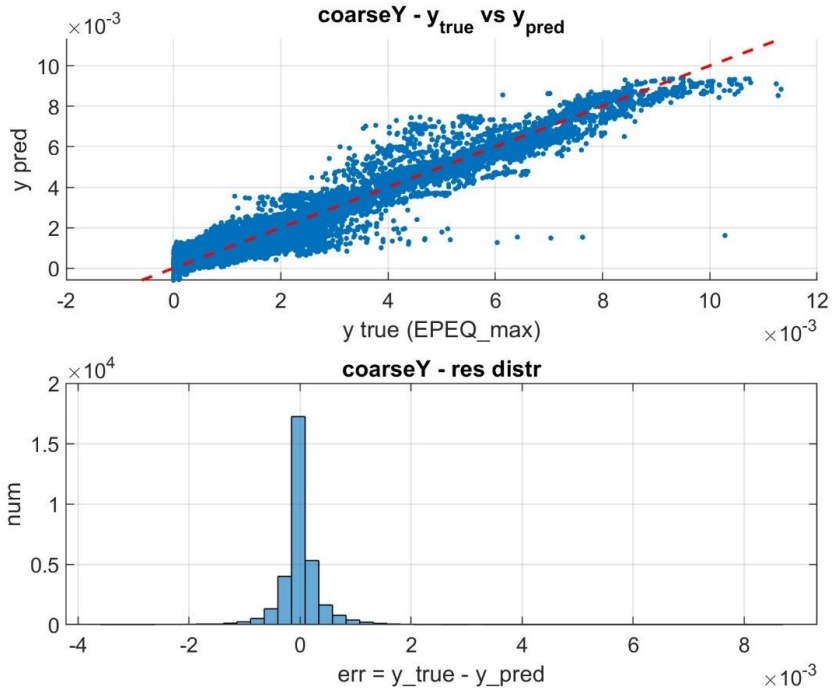

Figure 47 Validation of the surrogate model for the coarse mesh (Y direction)

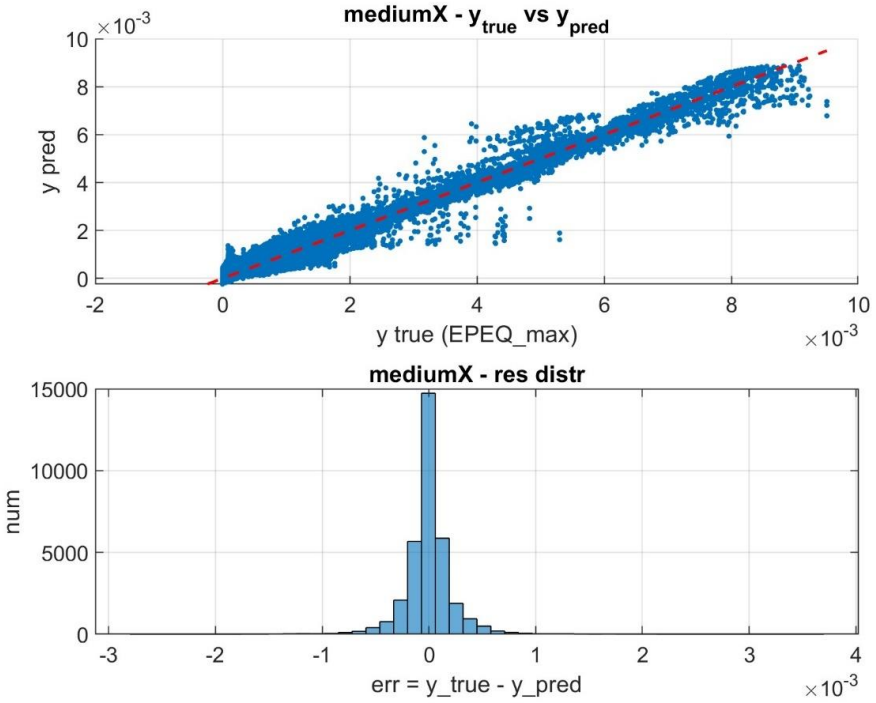

Figure 48 Validation of the surrogate model for the medium mesh (X direction)

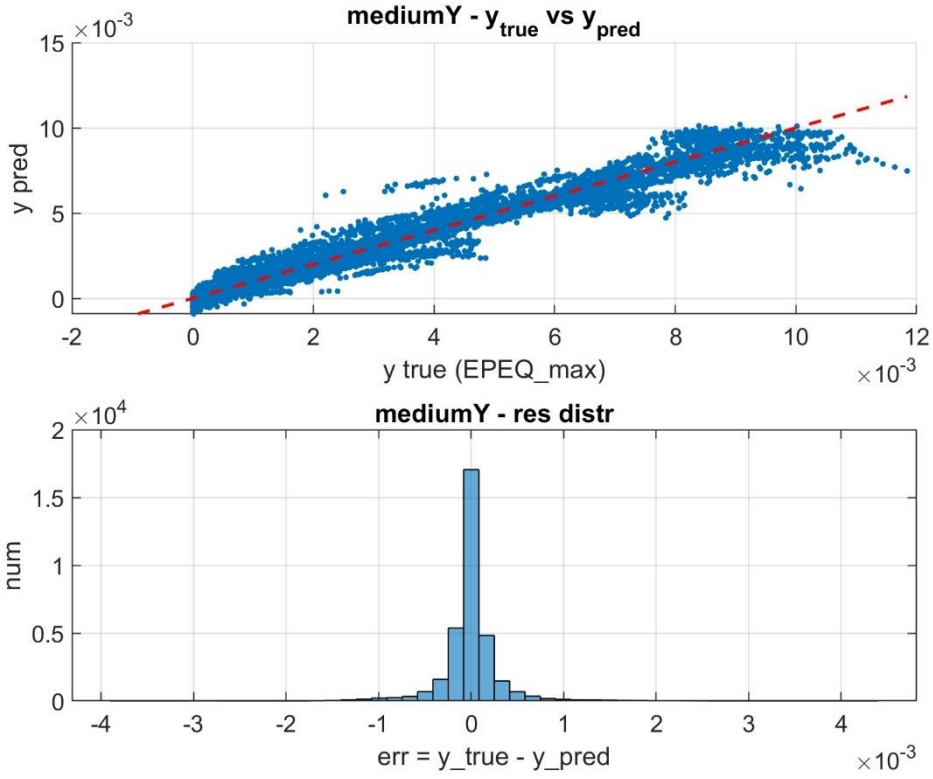

Figure 49 Validation of the surrogate model for the medium mesh (Y direction)

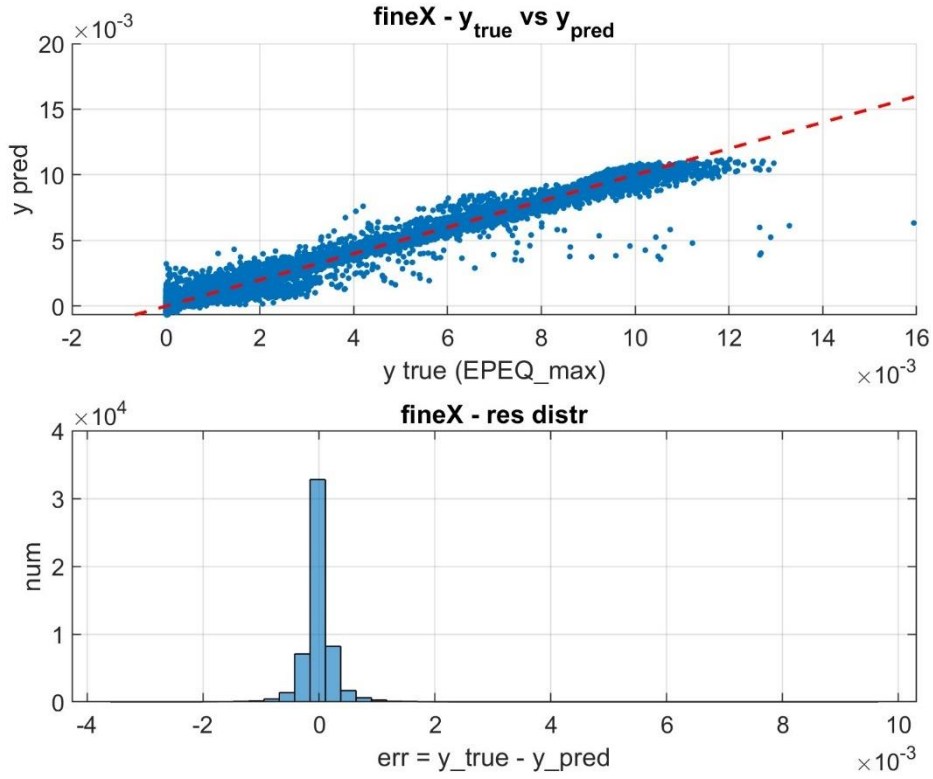

Figure 50 Validation of the surrogate model for the fine mesh (X direction)

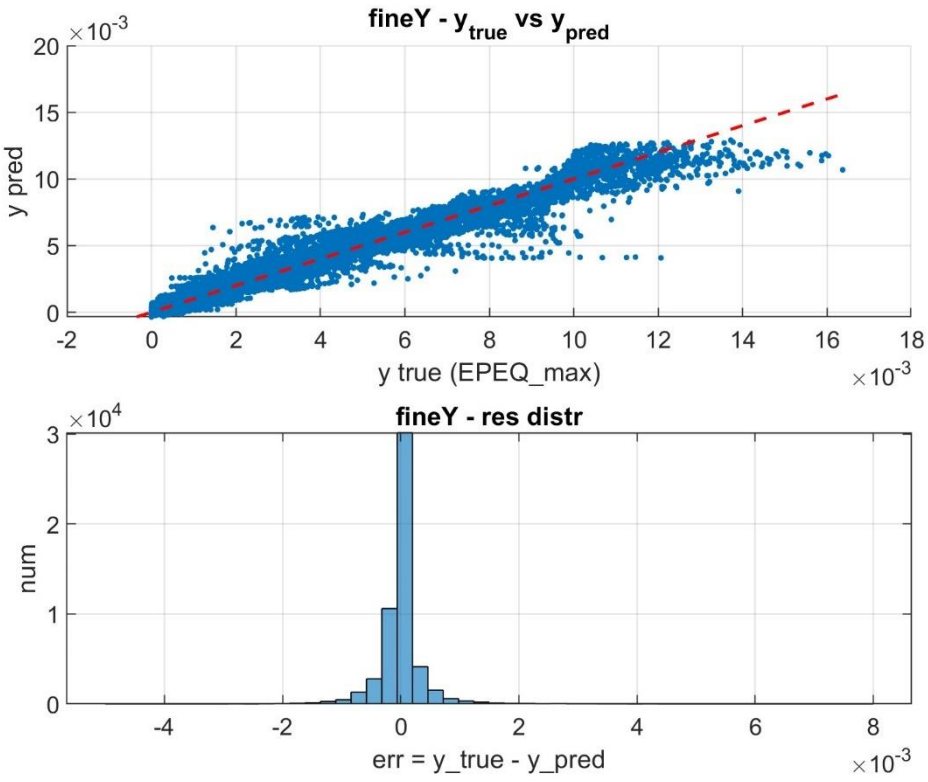

Figure 51 Validation of the surrogate model for the fine mesh (Y direction)

The fine-mesh model shows the strongest correlation compared to the other meshes, with the point cloud closely following the identity line and only minor deviations. Its higher resolution provides the most accurate strain predictions. Therefore, these results confirm the overall trend that accuracy improves from coarse to medium and is highest in the fine mesh.

4.3 Surrogate-based damage estimation

This section presents the damage fields obtained directly from the surrogate model and describes how these predictions can be visualized at higher spatial resolution. It is also possible to obtain an even finer spatial resolution by interpolating the surrogate predictions within MATLAB, since achieving such a fine resolution directly in ANSYS requires significant time and computational effort. Therefore, the idea is to generate a very fine mesh (0.03 m) of the model to use only as a reference for the node coordinates. This auxiliary mesh contains approximately 2.3 million nodes, compared to the 2,659 nodes used in the static nonlinear analysis, which illustrates the computational difficulty of running a full nonlinear simulation at this resolution. In

this approach, the surrogate provides the corresponding strain values, while the fine mesh is used solely to define the geometric detail of the tower, allowing MATLAB to perform a high-quality interpolation without requiring a full nonlinear analysis on such a dense discretization.

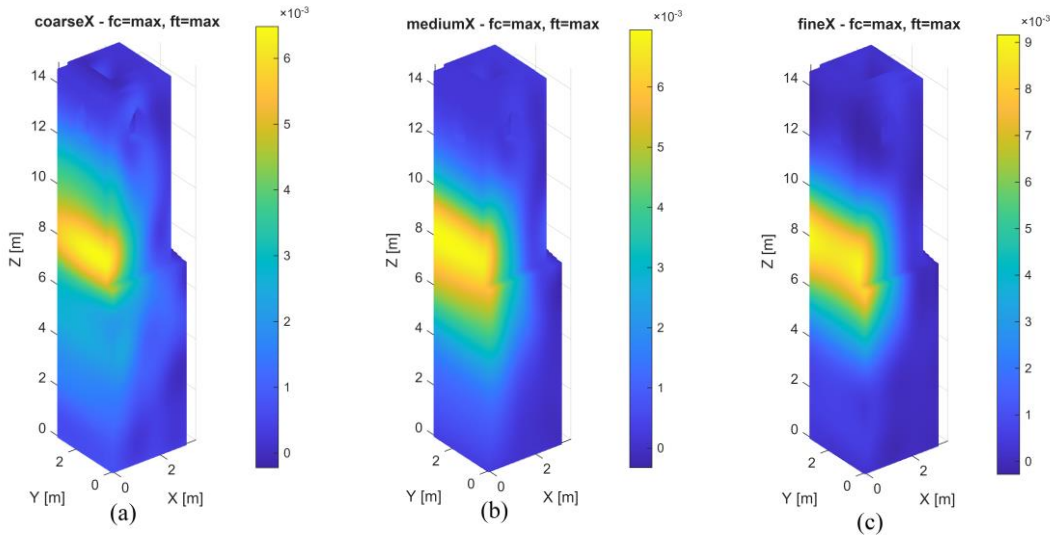

Figure 52 Interpolated EPEQ gradient for maximum value of fc and ft for (a) coarse (b) medium (c) fine X direction loading [SE direction]

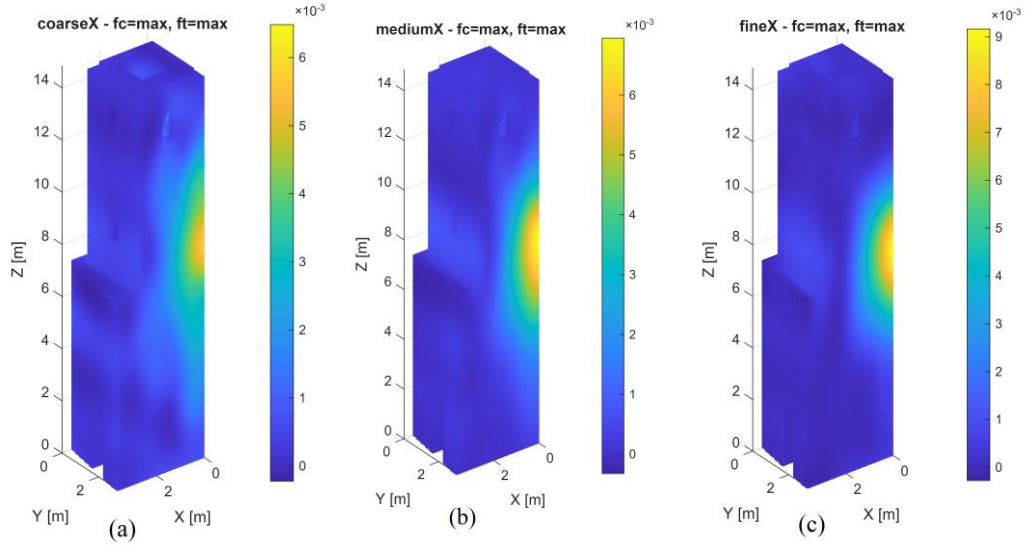

Figure 53 Interpolated EPEQ gradient for maximum value of fc and ft for (a) coarse (b) medium (c) fine X direction loading [NW direction]

The interpolated plastic strain fields provide a clear representation of the damage mechanism within the bell tower. Although the pattern of the strain field remains consistent for all mesh densities and mechanical parameter combinations, the intensity of the localized band increases with mesh refinement. The coarse mesh predictions display a broader damage region, whereas the medium mesh sharpens the contours,

and the fine mesh produces a highly concentrated strain band. Despite these differences in intensity, the position of the maximum EPEQ gradient is remarkably stable, consistently forming a localized zone between approximately 6 m and 9 m in height and oriented according to the imposed loading direction.

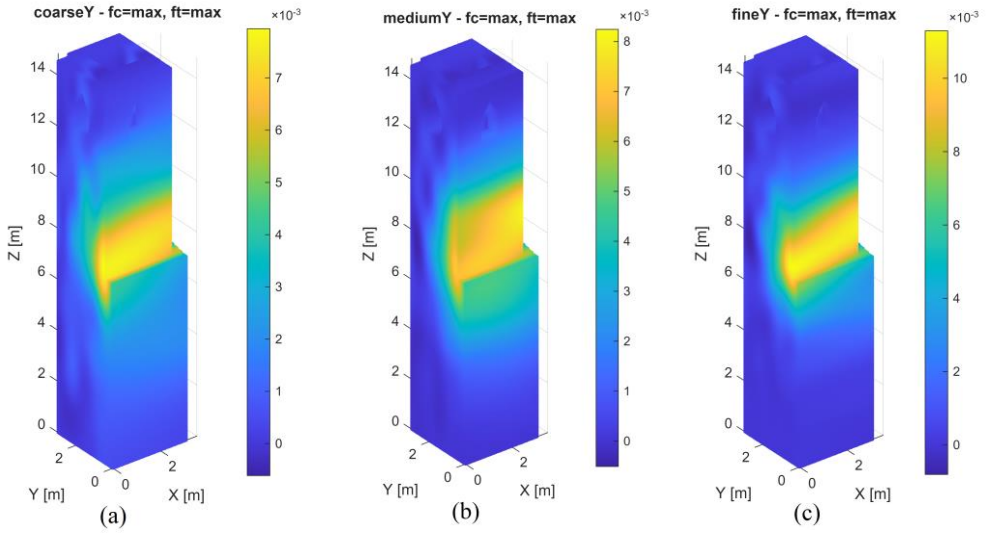

Figure 54 Interpolated EPEQ gradient for maximum value of fc and ft for (a) coarse (b) medium (c) fine Y direction loading [SE direction]

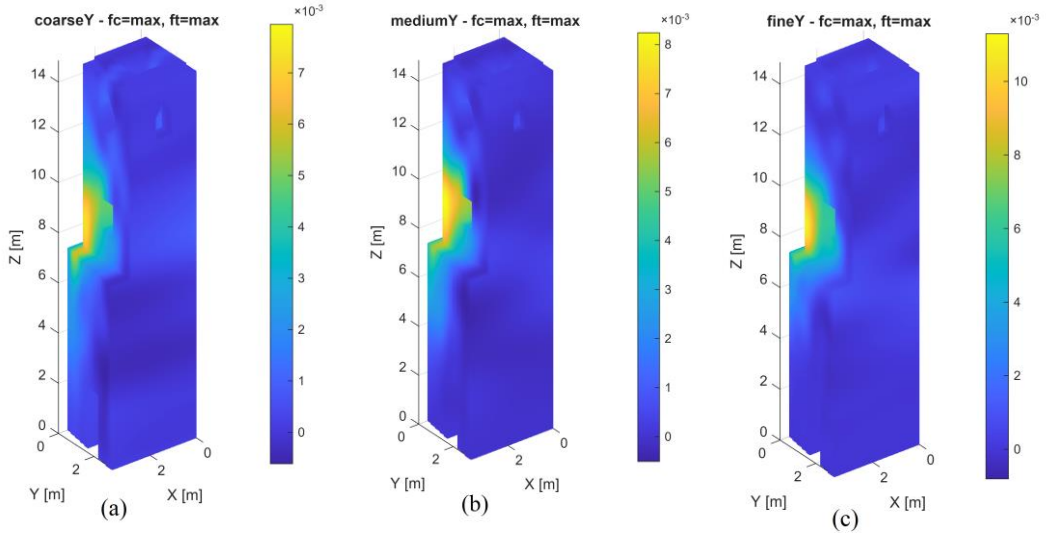

Figure 55 Interpolated EPEQ gradient for maximum value of fc and ft for (a) coarse (b) medium (c) fine Y direction loading [NW direction]

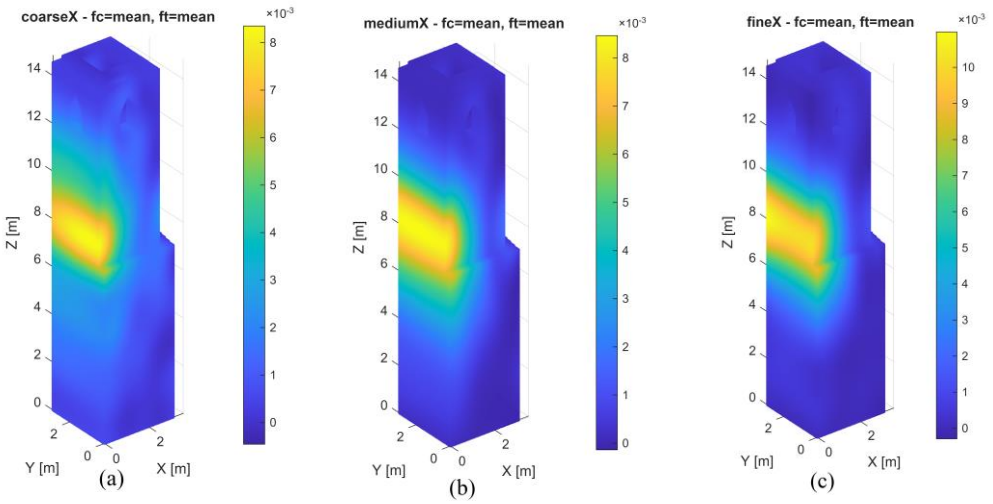

Figure 56 Interpolated EPEQ gradient for mean value of fc and ft for (a) coarse (b) medium (c) fine X direction loading [SE direction]

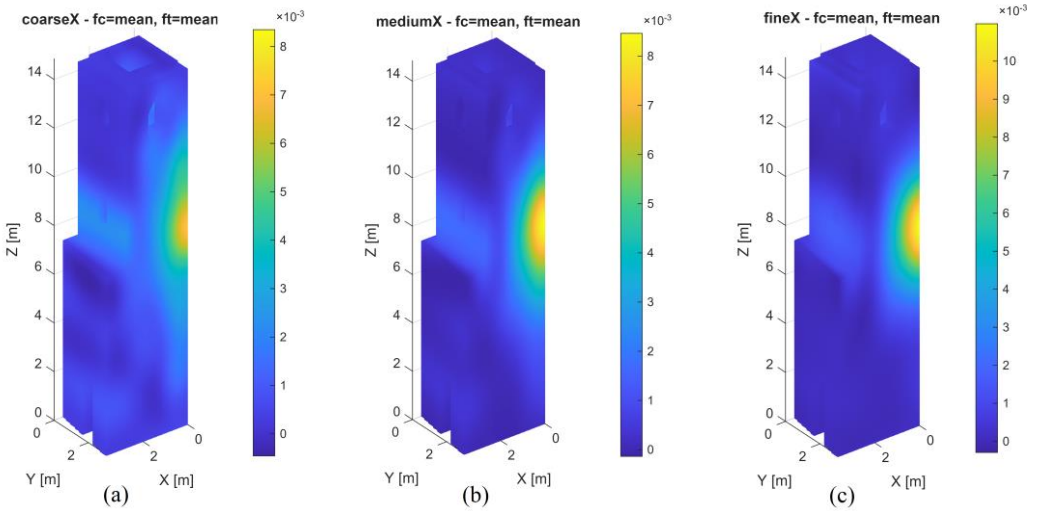

Figure 57 Interpolated EPEQ gradient for mean value of fc and ft for (a) coarse (b) medium (c) fine X direction loading [NW direction]

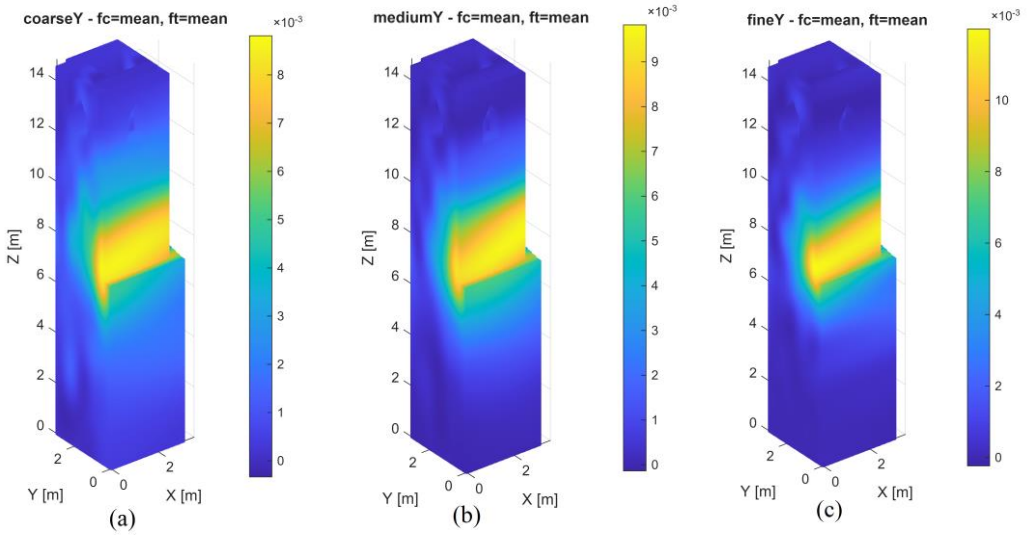

Figure 58 Interpolated EPEQ gradient for mean value of fc and ft for (a) coarse (b) medium (c) fine Y direction loading [SE direction]

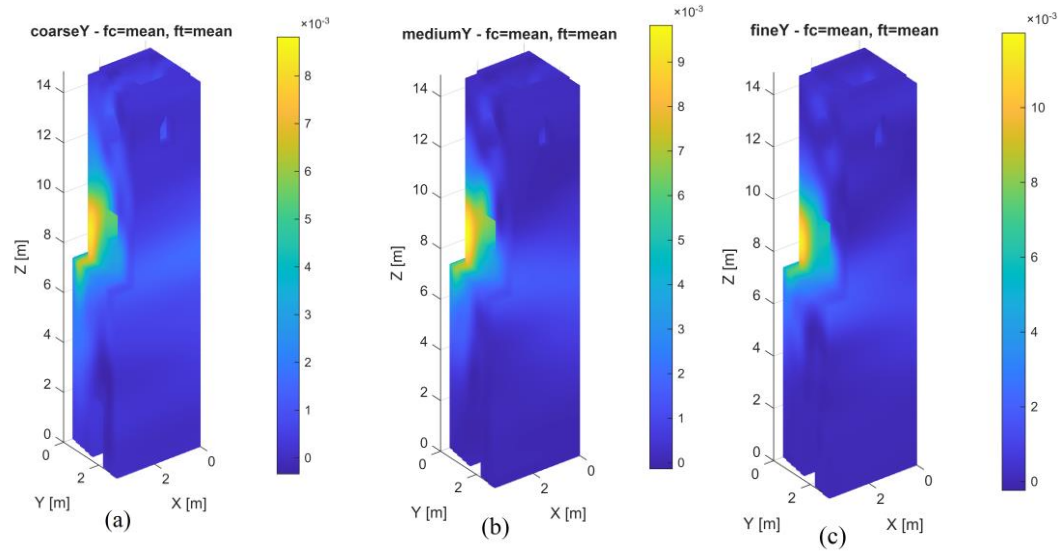

Figure 59 Interpolated EPEQ gradient for mean value of fc and ft for (a) coarse (b) medium (c) fine Y direction loading [NW direction]

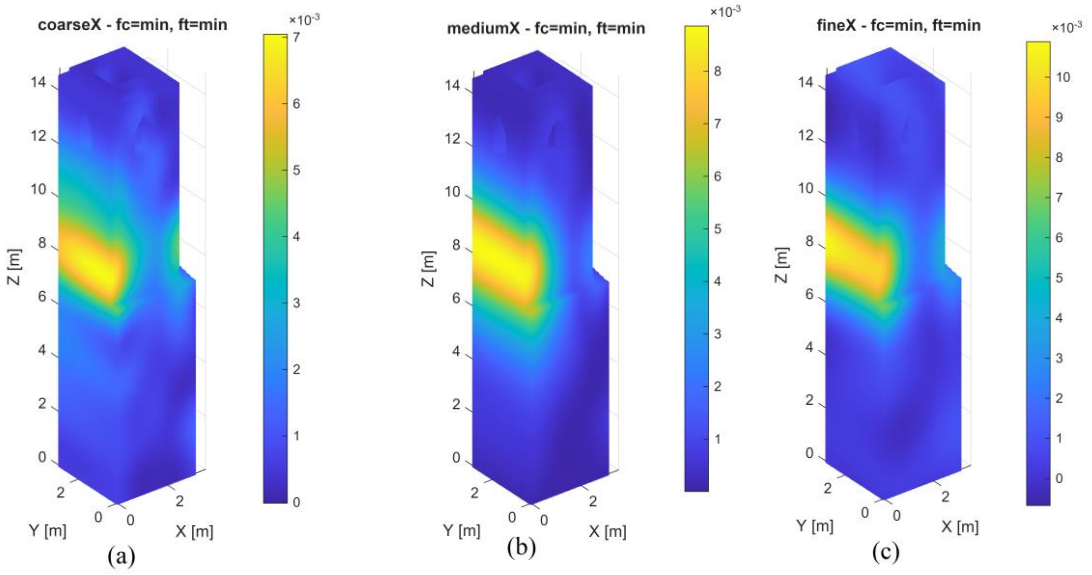

Figure 60 Interpolated EPEQ gradient for minimum value of fc and ft for (a) coarse (b) medium (c) fine X direction loading [SE direction]

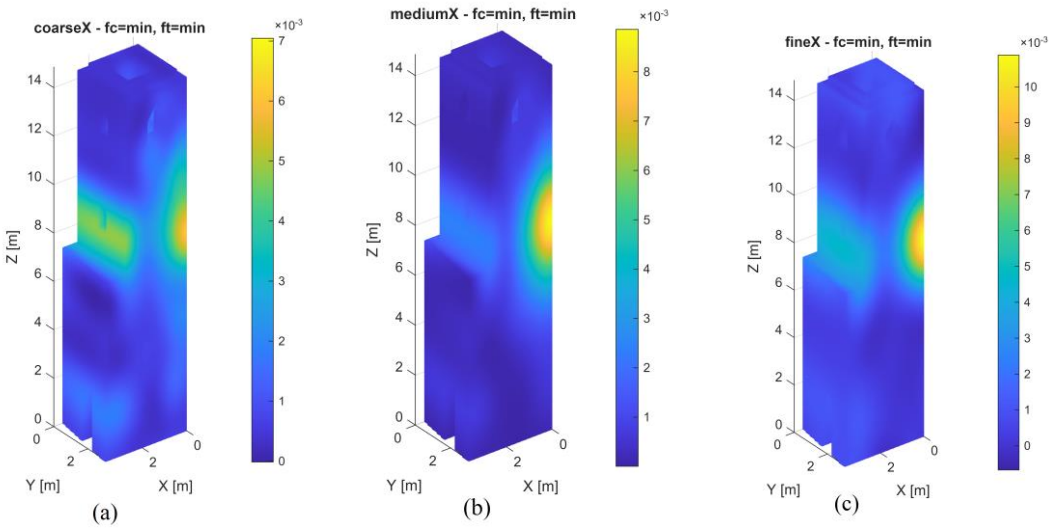

Figure 61 Interpolated EPEQ gradient for minimum value of fc and ft for (a) coarse (b) medium (c) fine X direction loading [NW direction]

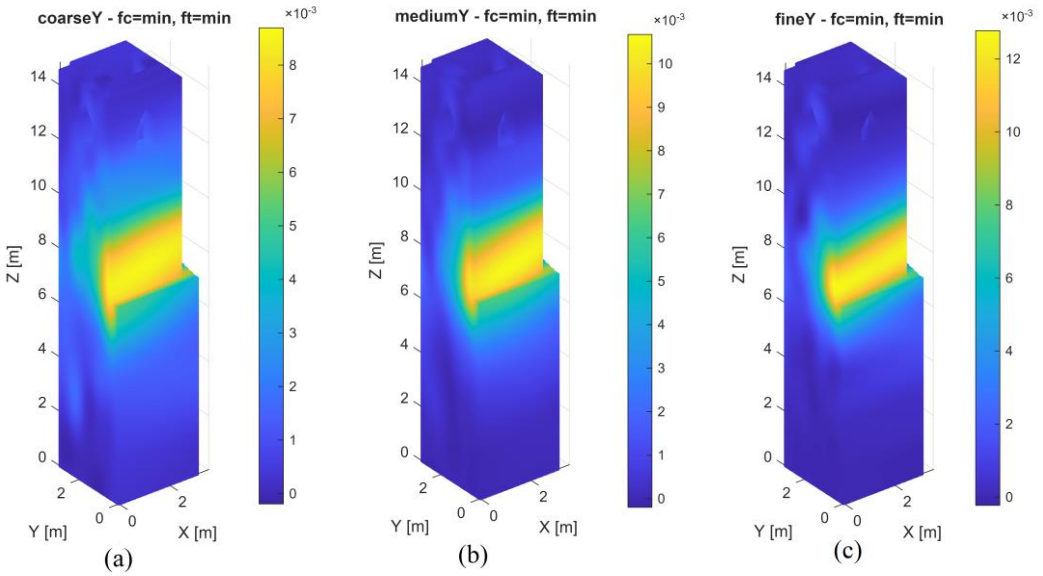

Figure 62 Interpolated EPEQ gradient for minimum value of fc and ft for (a) coarse (b) medium (c) fine Y direction loading [SE direction]

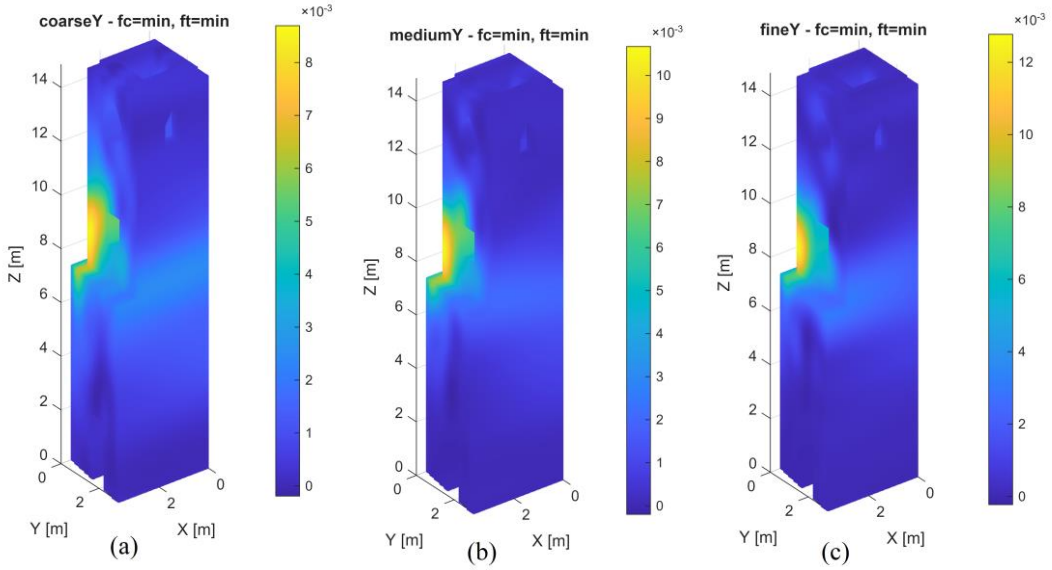

Figure 63 Interpolated EPEQ gradient for minimum value of fc and ft for (a) coarse (b) medium (c) fine Y direction loading [NW direction]

5.0 Model optimization framework

The numerical and surrogate analyses presented in the previous chapters indicated that nonlinear behavior in masonry structures is typically concentrated in specific regions, rather than being uniformly distributed. This gives the opportunity to formulate numerical models in which nonlinear constitutive laws are applied only where structurally required, reducing computational effort while maintaining accuracy. To support this strategy, a model optimization framework, based Bayesian Optimal Experimental Design is employed to identify the regions of the structure most sensitive to variations in material parameters and therefore most likely to exhibit nonlinear response.

In Hybrid Simulation applications, this optimization framework serves as a Bayesian tool for determining how a structure should be divided into its physical and numerical components, identifying which regions of a structure should be represented physically and which can be modeled numerically based on their expected informational contribution, thereby helping to determine in advance the area that would provide the most useful information if reproduced physically [17]. Although no physical–numerical coupling is carried out here, the same principle is applied to locate the structurally critical areas of the bell tower where nonlinear behavior is most likely to develop, and where nonlinear constitutive modelling is therefore required in the refined finite element model.

5.1 Setup and sampling for model optimization

The implementation of the model optimization strategy builds directly on the previously constructed surrogate models, which allow rapid evaluation of structural response for many combinations of material parameters. Using these models, the optimization procedure explores how the predicted damage pattern changes across the entire parameter range and uses this information to highlight the areas of the tower where nonlinear behavior is most likely to appear.

The optimization process begins with the definition of the material parameter vector $\theta = (f_c, f_t)$. Instead of sampling across an arbitrary parameter space, the bounds for f_c and f_t are restricted to the minimum and maximum values used in the finite element

analyses.

$$\theta_i = (f_{c,i},\, f_{t,i})$$

$$f_c \in [408{,}412,\ 1{,}721{,}808]\ Pa \quad , \quad f_t \in [0,\ 95{,}842]\text{Pa}$$

This approach maintains consistency with the approximated mechanical characteristics of the masonry bell tower and prevents the consideration of unrealistic strength combinations.

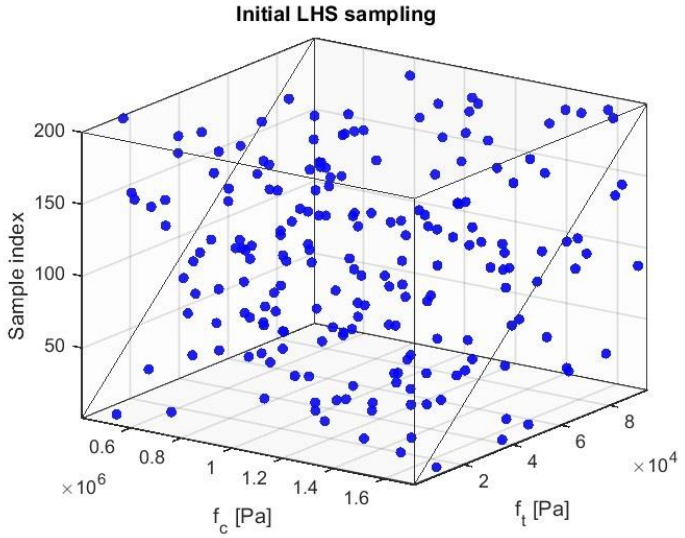

Figure 64 Initial LHS samples inside the (f_c, f_t) parameter domain

Within these bounds, Latin Hypercube Sampling (LHS) is used to create a well-distributed set of material parameter combinations.

5.2 Surrogate damage evaluation

For each sampled θ_i, the surrogate models are evaluated at all nodes to predict the strain components $S_x(i)$ and $S_y(i)$. These two quantities are then combined into a single measure of local damage and normalized across the entire structure. In this way, each parameter sample produces a complete damage field $D(i)$ that describes how the structure would respond under that specific material configuration.

$$X_{inp} = \left[\, x_i,\, y_i,\, z_i, f_{c,i},\, f_{t,i} \,\right], \qquad \forall\, i = 1, \ldots, n_{XYZ}$$

$$S_x(i) = modelsX.fine\left(X_{inp}(i)\right) \quad , \qquad S_y(i) = modelsY.fine\left(X_{inp}(i)\right)$$

$$D_i^{raw} = \sqrt{S_x(i)^2 + S_y(i)^2}$$

$$D(i)normalized = \frac{D_i^{raw}}{\max\limits_j D_j^{raw}}, D(i) \in [0,1]$$

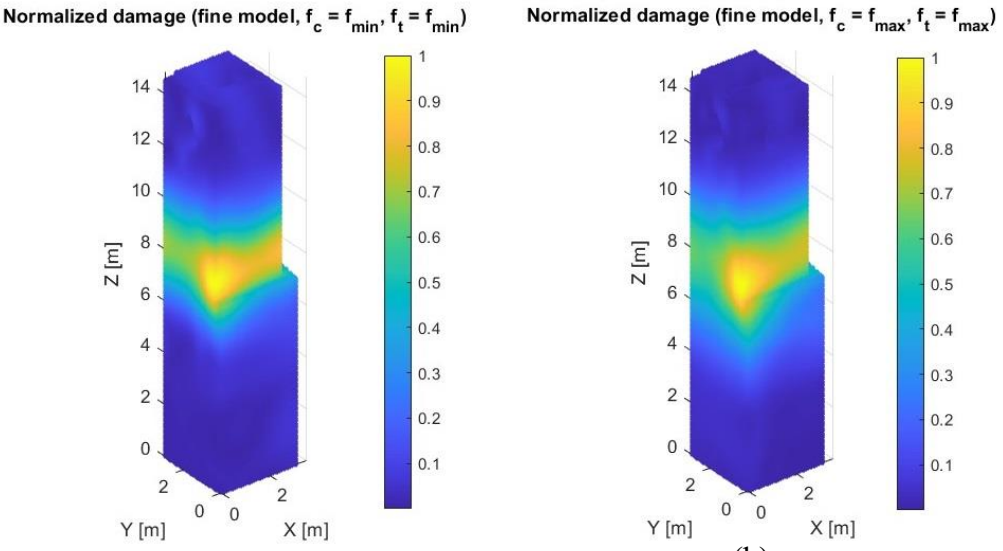

Figure 65 Normalized damage fields for the minimum (a) and maximum (b) material-strength parameters.

For each normalized damage field $D(i)$, three scalar indicators are calculated to describe how the predicted damage is distributed across the structure. In this scale, values of $D(i)$ close to 0 correspond to undamaged or elastic behavior, while values close to 1 indicate severe damage.

Following the approach adopted in the optimization framework, first, the Shannon entropy $H(\theta)$ indicates how widely the damage spreads across the structure, Low entropy means that the damage is concentrated in a few specific zones, while higher entropy reflects a more diffuse pattern [17].

$$H(\theta) = -\frac{1}{\log_2 N}\sum_{i=1}^{N} D(i)\ \log_2 D\ (i)$$

Second, the mean value $\mu(\theta)$ shows the overall intensity of the damage, small values indicate that the structure is mostly undamaged, whereas larger values correspond to

more severe global damage [17].

$$\mu(\theta) = \frac{1}{N}\sum_{i=1}^{N} D(i)$$

Third, the standard deviation $\sigma(\theta)$ shows how sharply damage is localized, by measuring the contrast between highly damaged and nearly undamaged regions [17].

$$\sigma(\theta) = \sqrt{\frac{1}{N-1}\sum_{i=1}^{N}\big(D(i) - \mu(\theta)\big)^2}$$

Together, these three quantities form the objective vector $J(\theta)$, which summarizes how each material sample influences the expected damage pattern [17].

$$J(\theta) = \left[H(\theta), \frac{1}{\mu(\theta)}, \frac{1}{\sigma(\theta)} \right]$$

5.3 Bayesian Optimization

After computing the objective indicators for all sampled parameter combinations, the model optimization framework builds a surrogate model that links these indicators $H(\theta)$, $\mu(\theta)$, and $\sigma(\theta)$ to the material parameters (f_c, f_t). The surrogate model is developed using Sparse Bayesian Learning (SBL). The (SBL) identifies the relationship between indicators and material parameters while also providing an estimate of the uncertainty associated with each prediction. This uncertainty is essential, as the damage values predicted by the surrogate models are not exact, and the algorithm requires information about the reliability of each prediction.

With the SBL predictions, each sampled parameter pair is evaluated using the Mahalanobis-distance. This distance measures how well the predicted indicators match the damage patterns obtained from the surrogate models, while also considering their uncertainty. Parameter combinations that lead to consistent and physically reasonable damage patterns have smaller distances, and these combinations are retained to form the approximate posterior distribution of (f_c, f_t).

Once these representative samples have been identified, Kernel Density Estimation (KDE) is applied to describe their distribution within the (f_c, f_t) domain. The KDE

produces a smooth probability surface that shows how the initially broad uncertainty in the material strengths becomes concentrated around the combinations that lead to coherent damage patterns across the structure. This transition from a diffuse prior to a focused posterior distribution is visible in the following figures, where the parameter density is shown before and after the Bayesian update.

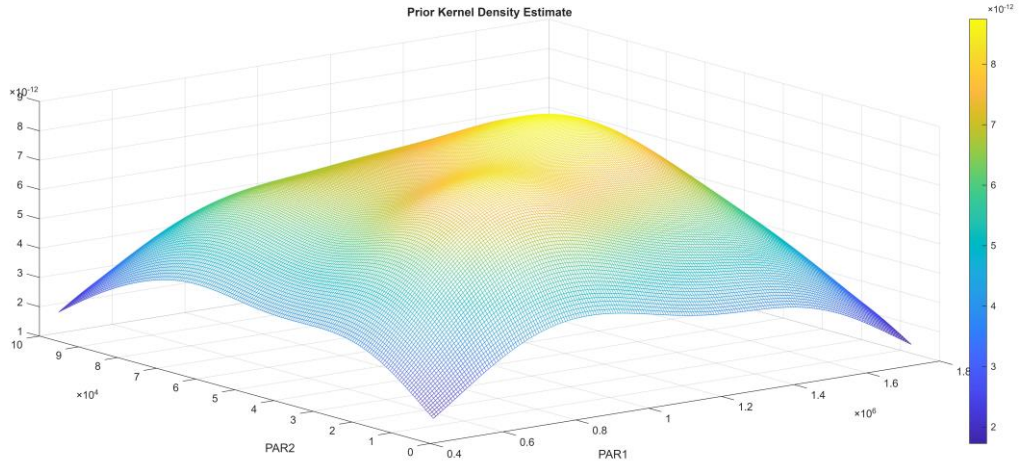

Figure 66 Prior Kernel Density Estimate.

The prior kernel density estimate represents the initial sampling distribution of the two material parameters, f_c (par1) and f_t (par2), before the Bayesian update is applied.

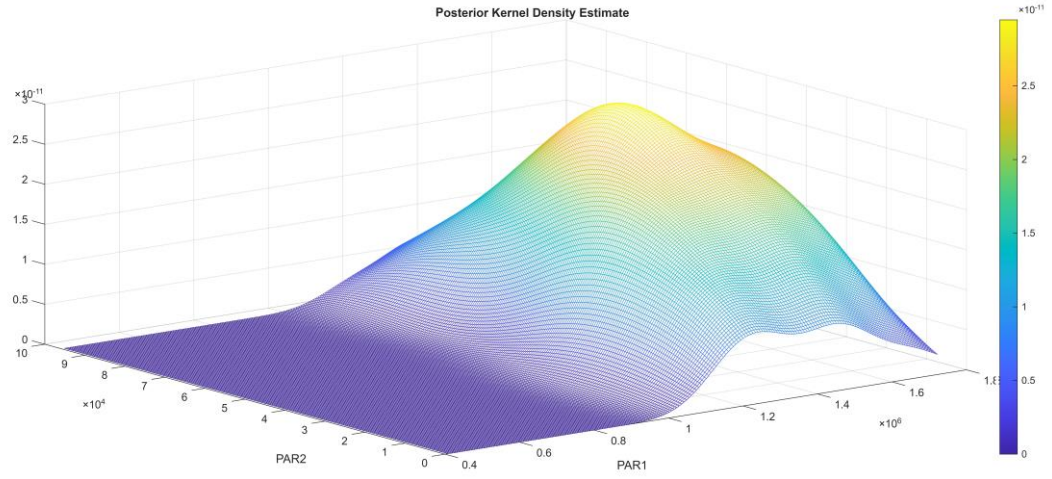

Figure 67 Posterior Kernel Density Estimate.

The comparison between the prior and posterior densities shows how the Bayesian update narrows the parameter domain. The prior is intentionally wide because the material strengths are initially uncertain, while the posterior becomes concentrated around the combinations of (f_c, f_t)that match the retained samples. This tightening of

the distribution reflects the region where the surrogate-based indicators are most coherent. Following this posterior update, the analysis proceeds by introducing an acquisition function that directs the exploration toward those regions of the parameter space that are considered most informative.

To further refine the parameter exploration, an Expected Improvement (EI) function is evaluated over the (f_c, f_t) domain. The EI surface highlights the parameter regions where new samples would be most useful, either because the predicted indicators are promising or because the uncertainty remains high. In this way, EI points to the areas where additional evaluations can provide the greatest information gain, as shown in the following figure.

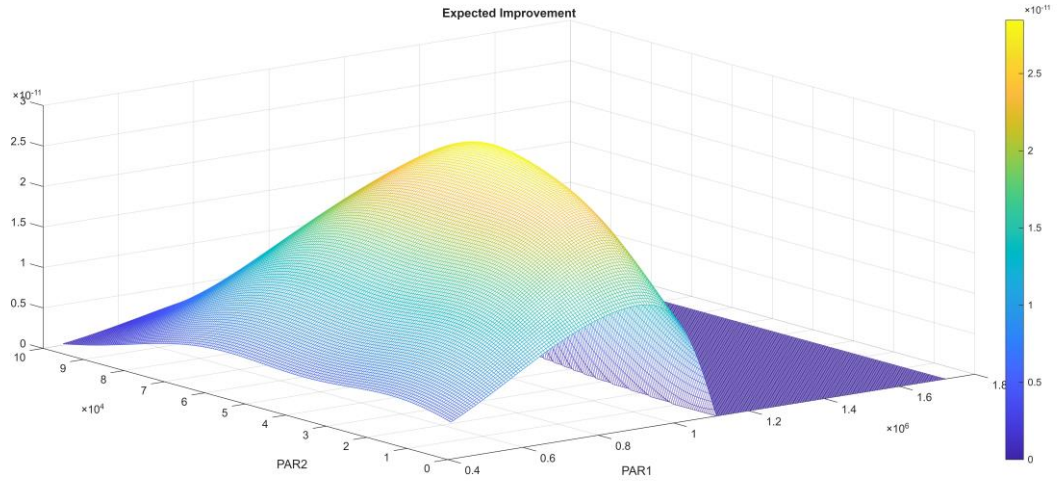

Figure 68 Expected Improvement

Building on the information provided by the posterior density and the EI surface, a sampling probability distribution is then constructed to generate the next set of material parameters. This distribution increases its weight in regions that are both plausible, according to the posterior, and potentially informative, according to the EI. In this way, the new samples are concentrated where they can meaningfully contribute to the refinement of the parameter domain. The resulting sampling PDF, together with the points drawn from it, is shown in the following figure.

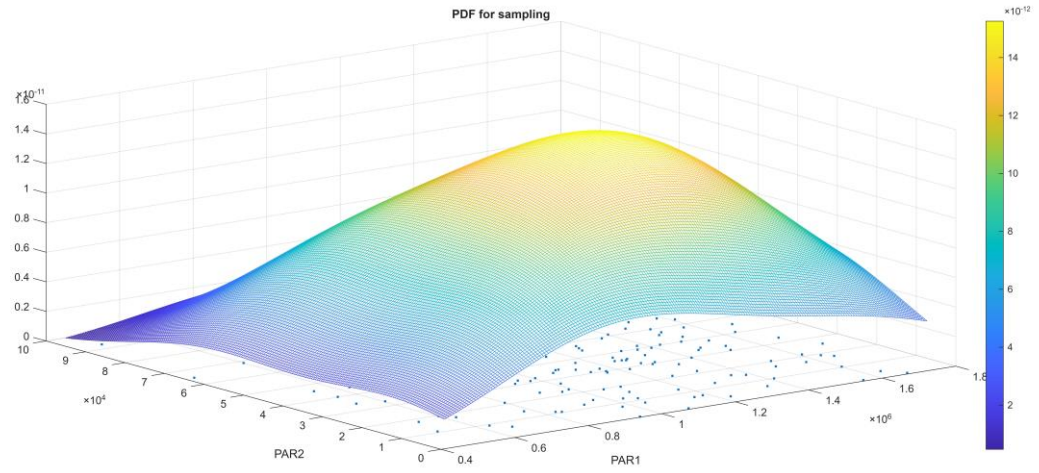

Figure 69 Probability density function for sampling

To assess whether the Bayesian optimization process is converging, the Jensen–Shannon Divergence (JSD) is evaluated at each cycle by comparing the initial prior density with the updated sampling distribution. The JSD provides a numerical measure of how much the distribution changes from one iteration to the next and gradually approaching zero shows that the updates no longer introduce significant changes. Also, it confirms that the algorithm has reached a stable posterior, and resulting parameter distribution used for the damage analysis is not the outcome of an early or arbitrary stopping point.

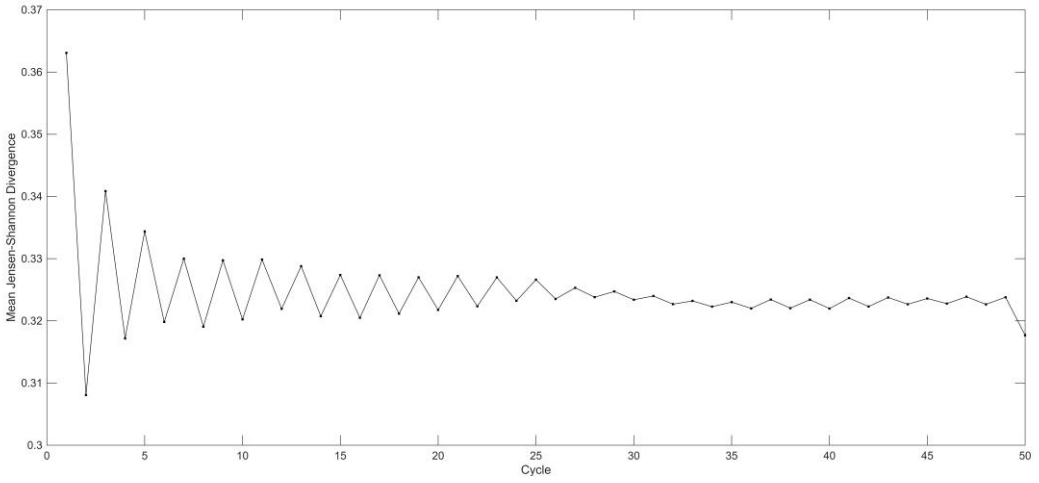

Figure 70 Mean Jensen Shannon divergence (JSD)

5.4 Final damage distribution

After the posterior distribution of the material parameters is obtained, the corresponding parameter samples are used to estimate the expected damage in the structure. For each retained sample in the posterior, the surrogate models are evaluated to compute the strain components at all nodes, and a normalized damage field is generated. By combining these fields, the mean, standard deviation, and a three-sigma estimate of the predicted damage can be derived, allowing the identification of the regions most likely to experience significant damage in the refined finite element model.

The first result obtained from the posterior samples is the mean of the normalized damage fields. This quantity highlights the regions where the surrogate models consistently predict higher damage across all plausible parameter combinations. Areas with elevated mean values correspond to zones where the structural response is more sensitive to the material parameters and therefore more likely to experience significant damage. The mean distribution of damage over the bell tower is shown.

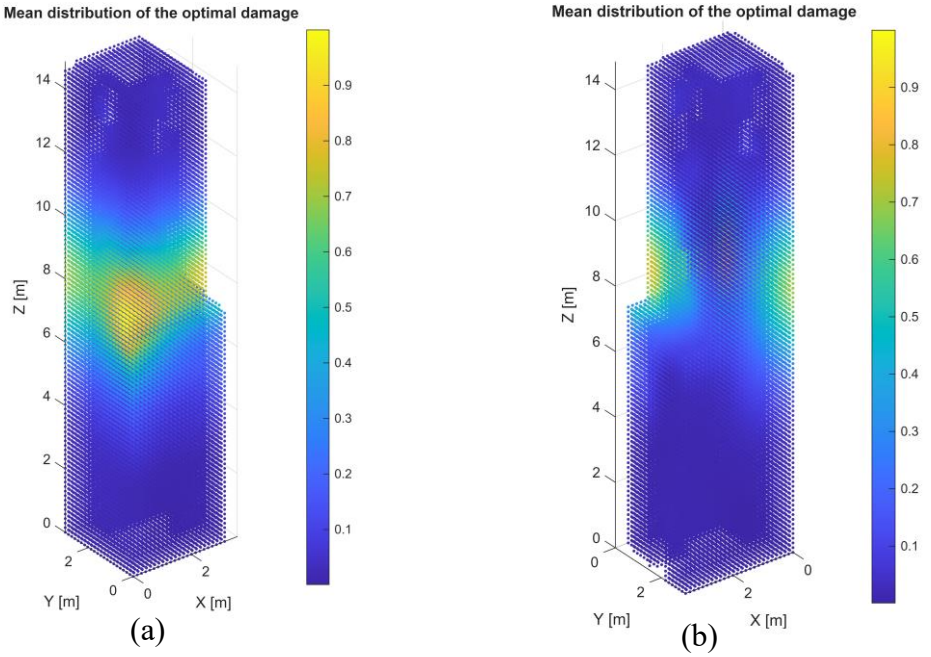

Figure 71 Mean distribution of the optimal damage (a) SE direction (b) NW direction

In addition to the mean field, the variability of the predicted damage is quantified through the standard deviation computed across all posterior samples. This measure reflects how sensitive each region of the structure is to changes in the

material parameters, low values indicate a stable prediction, while higher values reveal zones where the response is more uncertain.

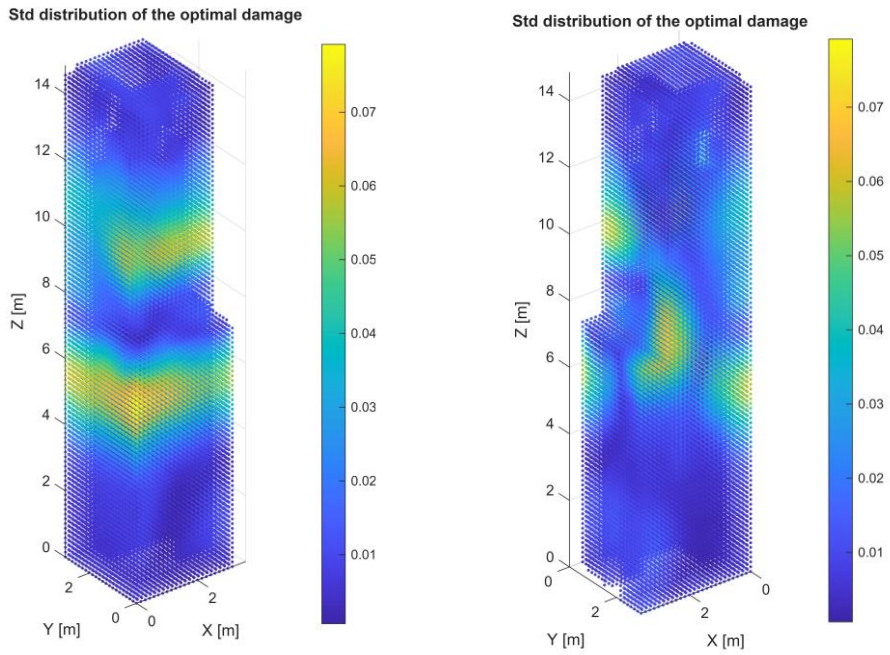

(a) (b)

Figure 72 Std distribution of the optimal damage (a) SE direction (b) NW direction

To obtain a conservative representation of the expected damage, a three-sigma envelope is constructed by combining the mean field with three times its standard deviation. The three-sigma damage field gives an overall picture of how the damage may vary across the structure.

To identify only the areas that matter for nonlinear modelling, a binary mask is applied to this field. A threshold range of 0.1 to 0.9 is used to divide the damage contour into two categories. Nodes with values above the threshold are designated as inelastic material and elastic material.

This mask turns the continuous damage results into a simple two-class map, clearly showing which parts of the structure should be modelled with nonlinear material behavior in the refined FEM model.

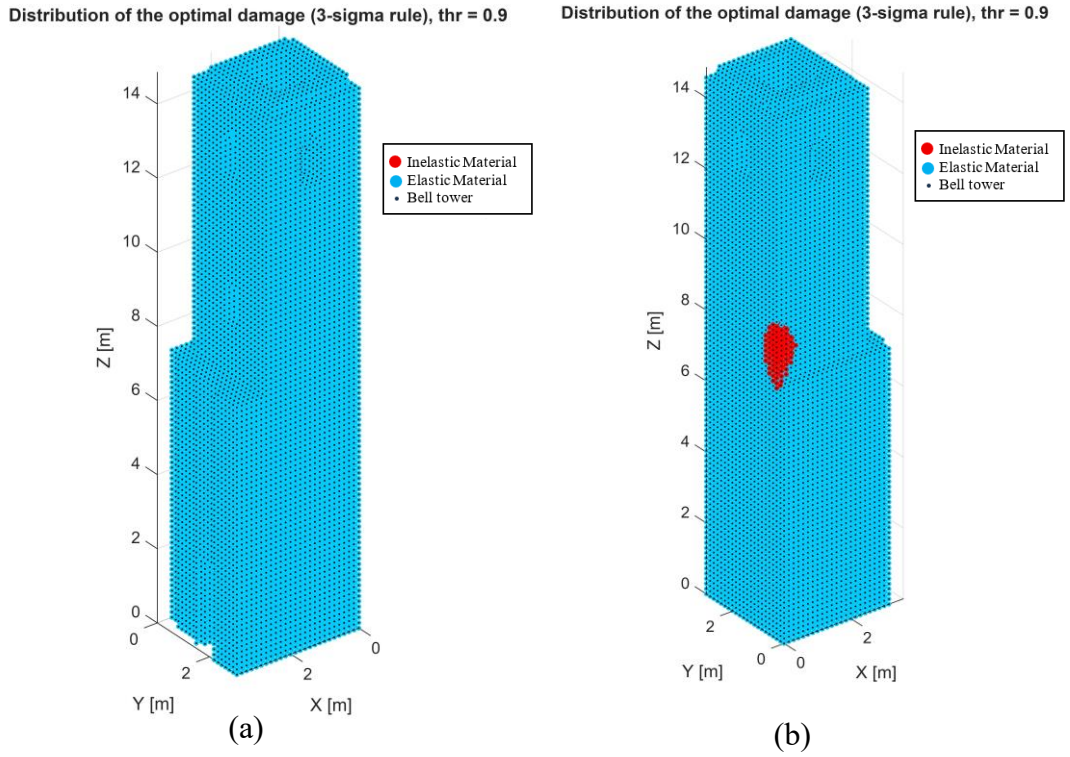

Figure 73 Distribution of optimal damage threshold 0.9 (a) NW direction (b) SE direction

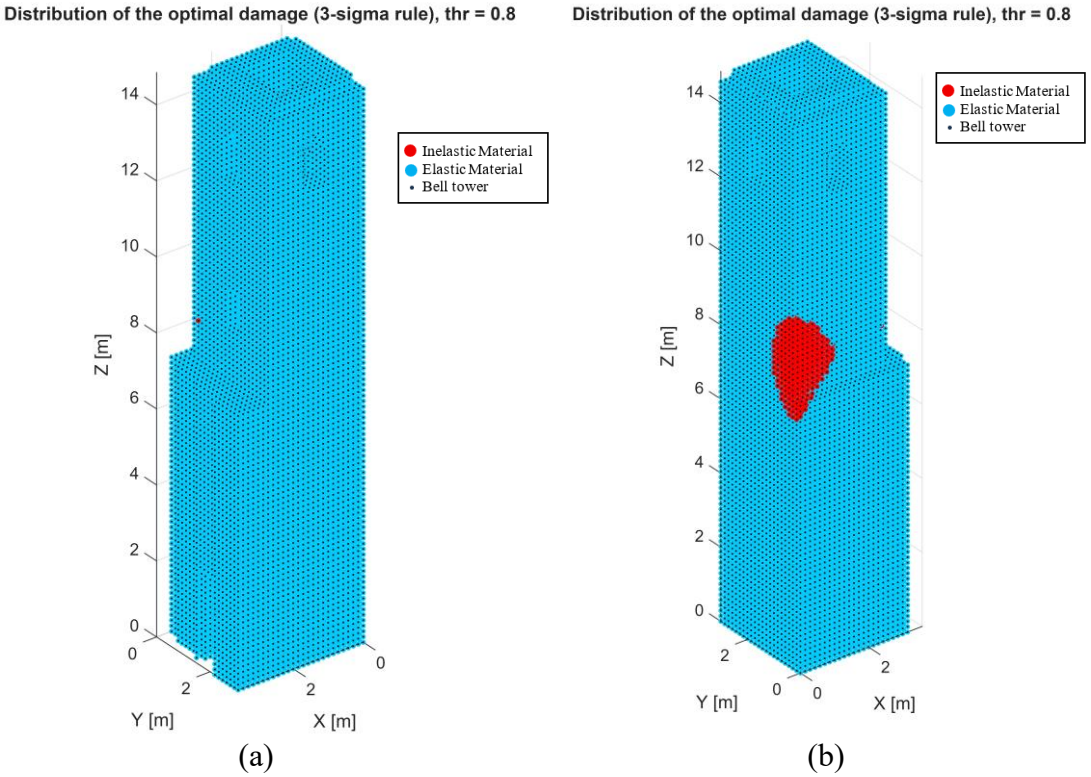

Figure 74 Distribution of optimal damage threshold 0.8 (a) NW direction (b) SE direction

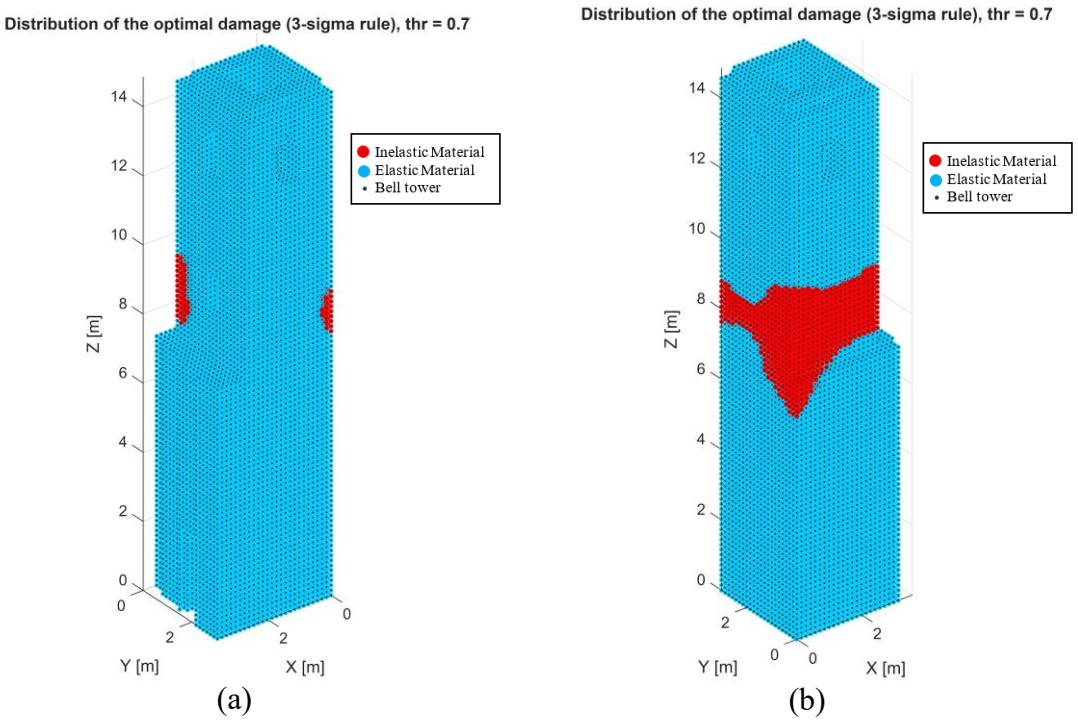

Figure 75 Distribution of optimal damage threshold 0.7 (a) NW direction (b) SE direction

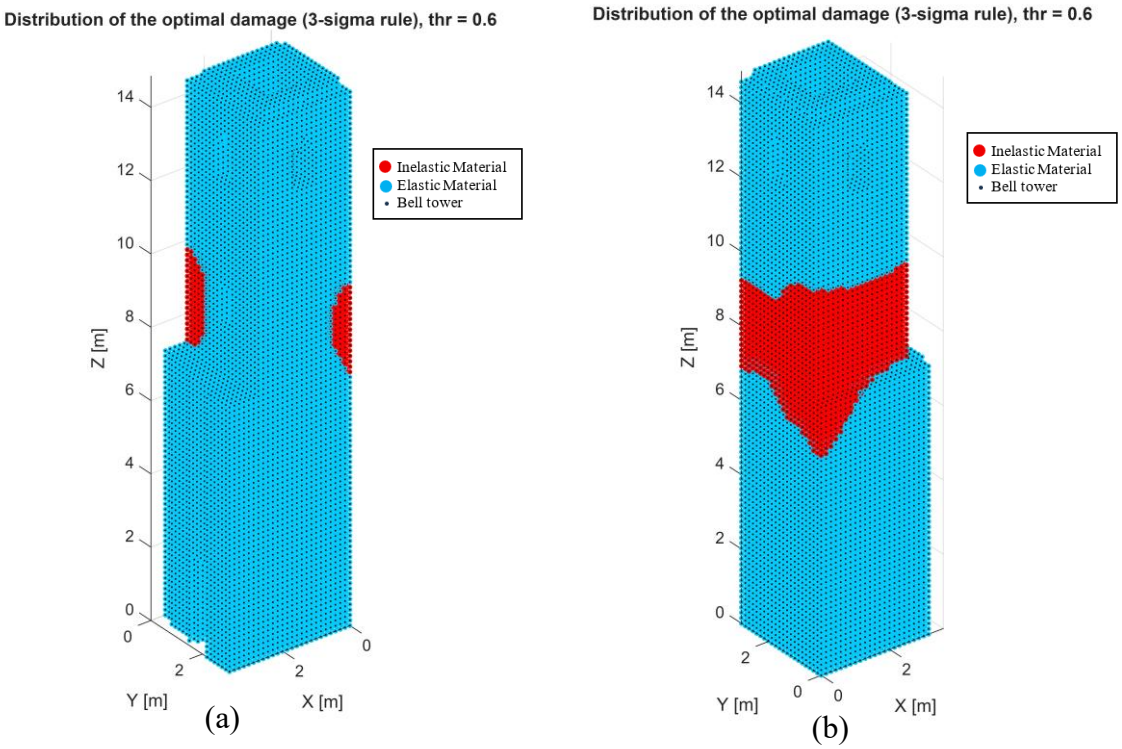

Figure 76 Distribution of optimal damage threshold 0.6 (a) NW direction (b) SE direction

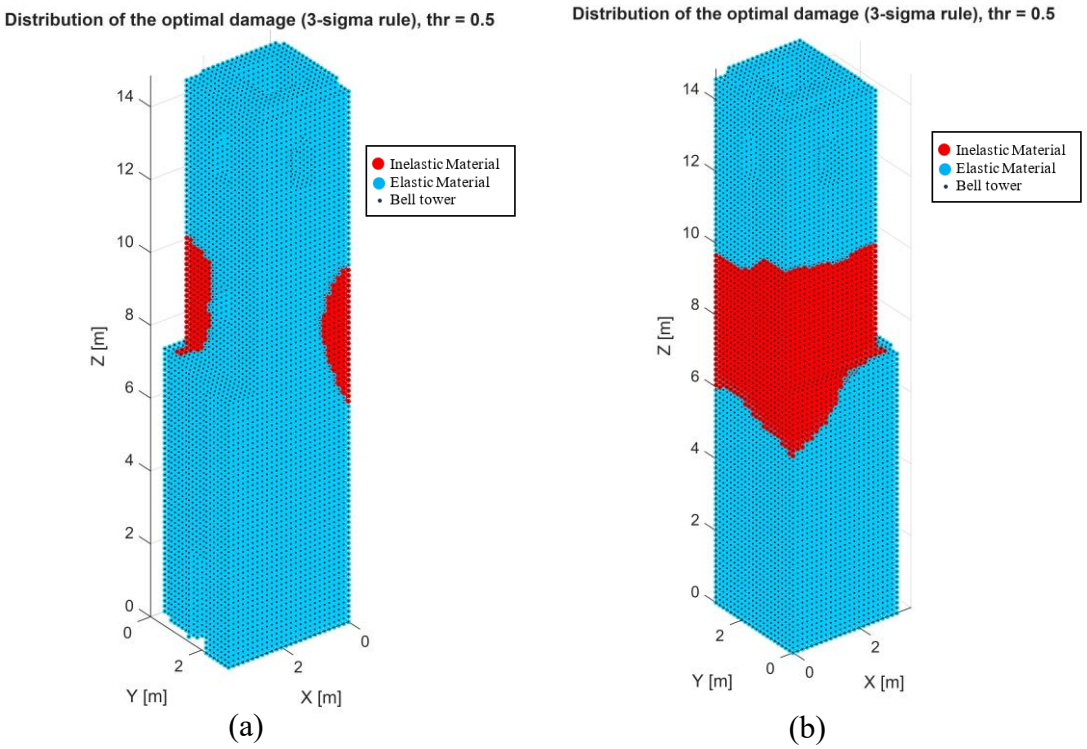

Figure 77 Distribution of optimal damage threshold 0.5 (a) NW direction (b) SE direction

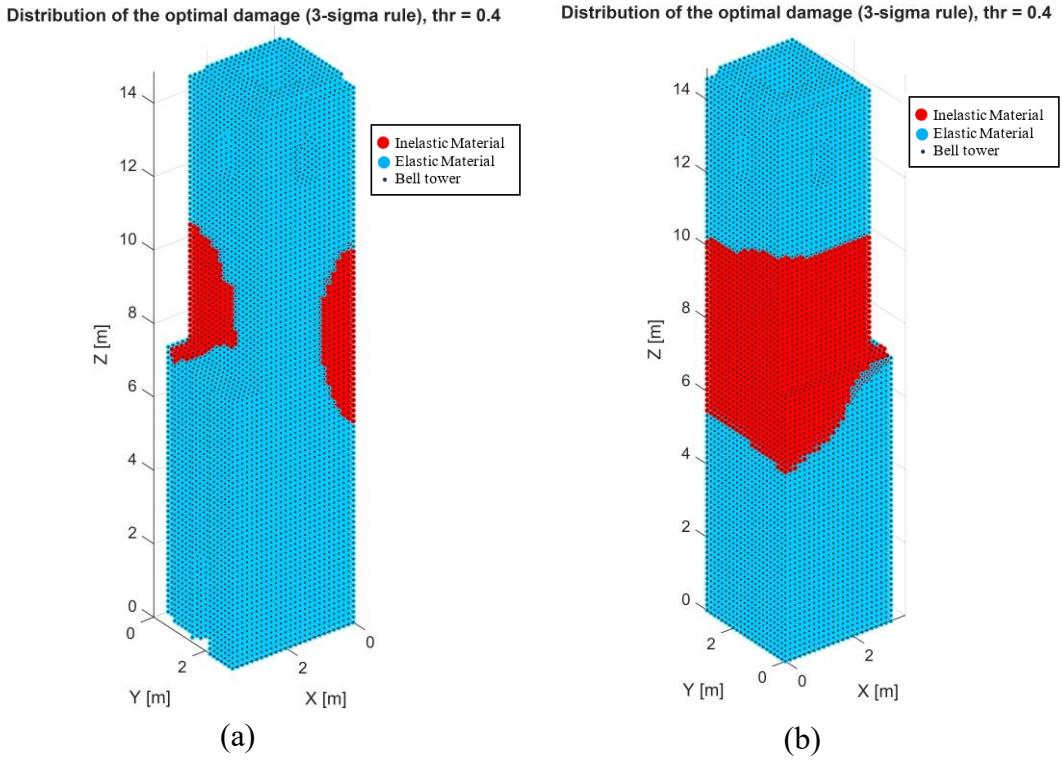

Figure 78 Distribution of optimal damage threshold 0.4 (a) NW direction (b) SE direction

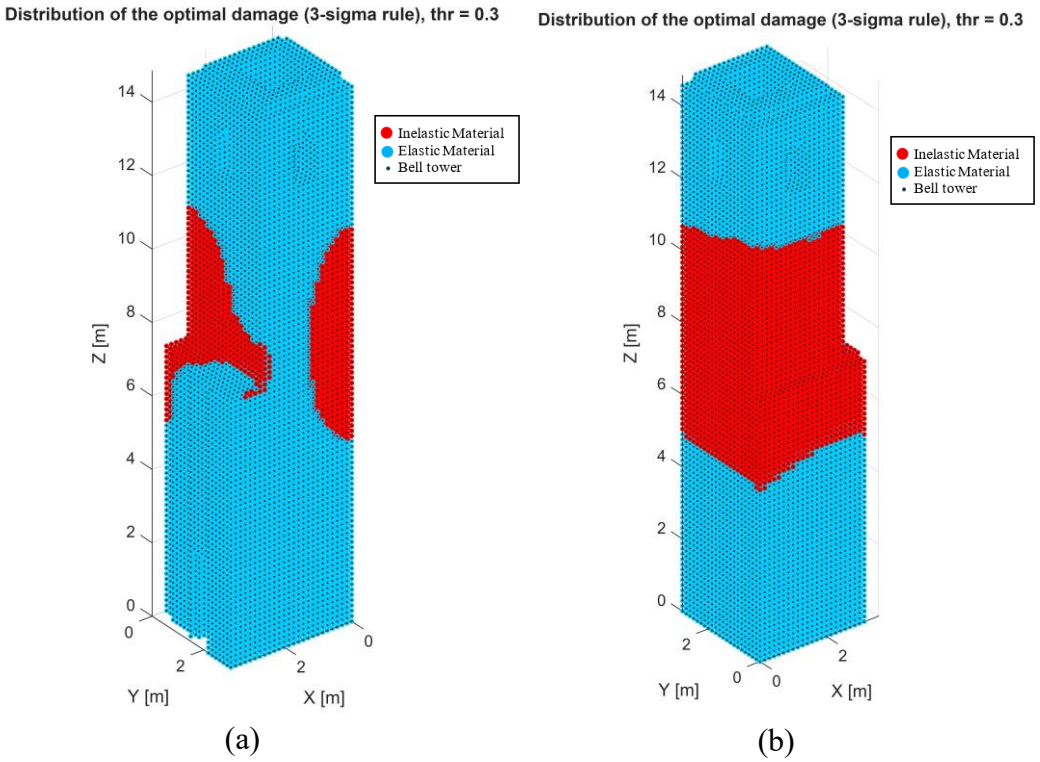

Figure 79 Distribution of optimal damage threshold 0.3 (a) NW direction (b) SE direction

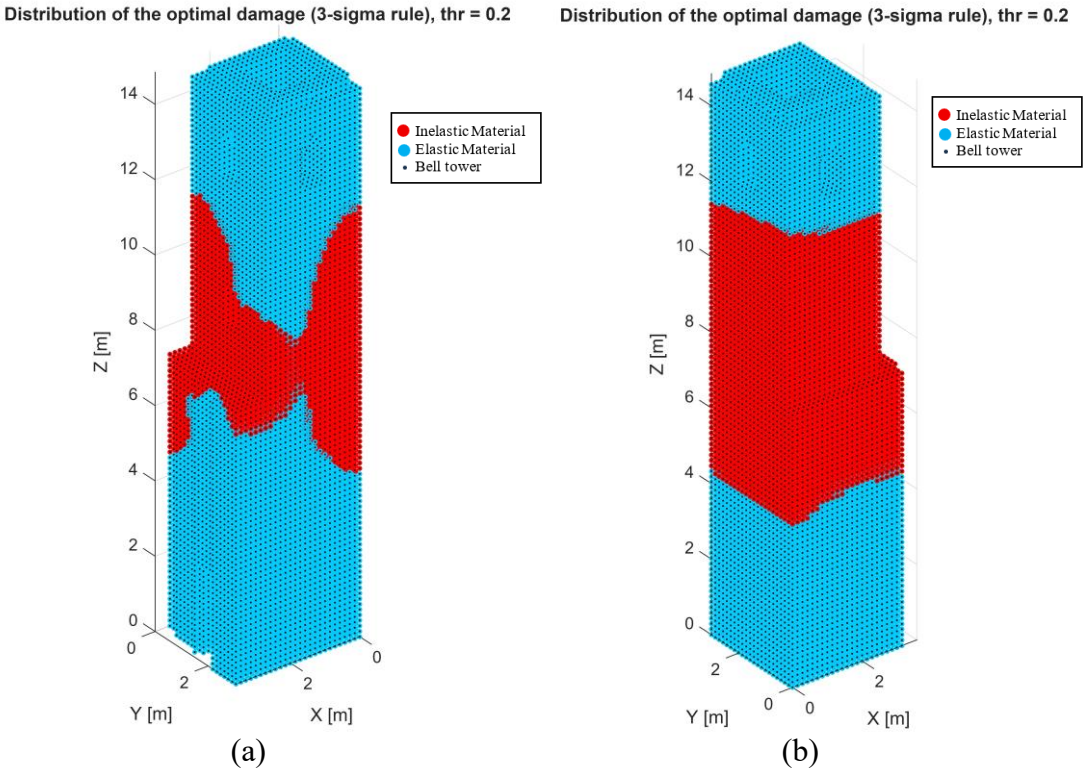

Figure 80 Distribution of optimal damage threshold 0.2 (a) NW direction (b) SE direction

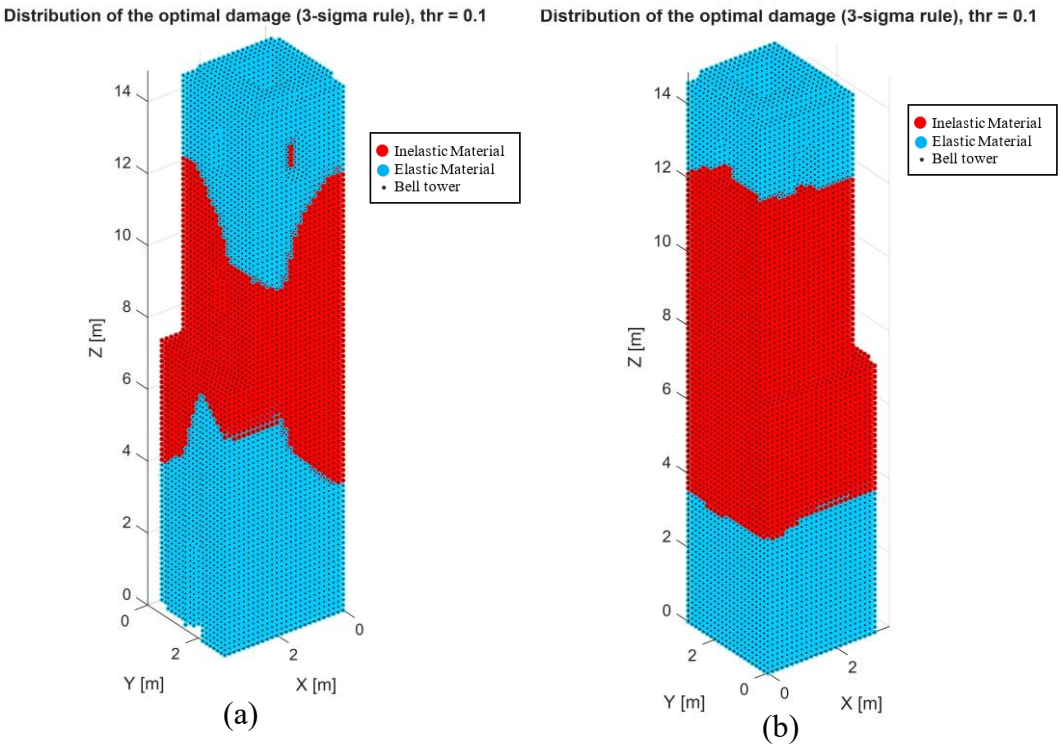

Figure 81 Distribution of optimal damage threshold 0.1 (a) NW direction (b) SE direction

Determining an appropriate threshold for defining the region to be modelled as nonlinear is an essential step, for that reason different values between 0.1 and 0.9 were tested, and the corresponding capacity curves were analyzed. For thresholds below 0.7, the capacity curve matched the full nonlinear capacity curve almost exactly, showing the same shape and behavior. When the threshold was increased above 0.7, the nonlinear region became smaller and the capacity curve changed, indicating that relevant damaged zones were being removed.

For this reason, the threshold of 0.7 was chosen and based on this the nonlinear material model was assigned to potentially significant area, using the mean values of f_c and f_t from dataset. The static nonlinear analysis is performed for both the X and Y directions on fine-mesh model.

5.5 Static nonlinear analysis of proposed model

The highly damaged region identified through the model optimization framework is now used to define the localized nonlinear model. In this configuration, the nonlinear constitutive law is assigned only to the highly damaged area. For simplicity, and to avoid introducing artificial discontinuities in the structural response, the nonlinear material is not applied strictly to damage nodes alone, but to all elements located within the corresponding elevation range. In this case, the nonlinear zone is bounded between Z_1 = 6.0 m and Z_2 = 9.0 m, as highlighted in the figure, ensuring that the entire structural band containing the damaged region is modelled consistently.

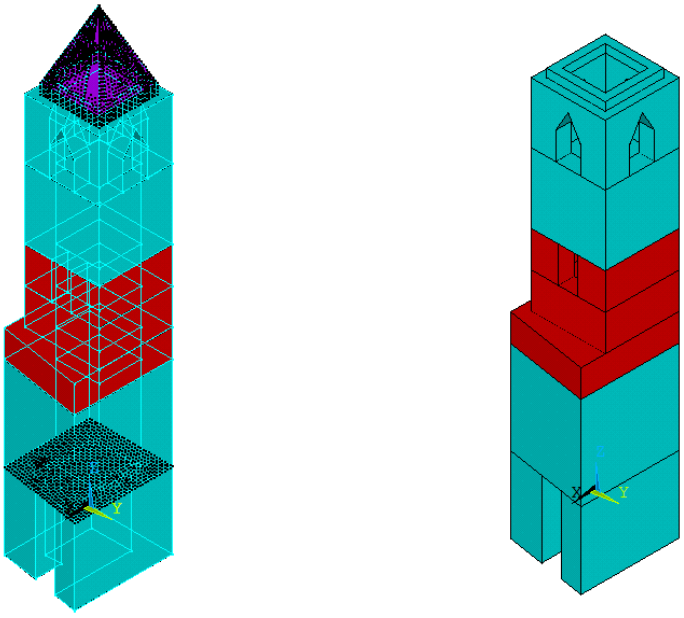

(a) (b)

Figure 82 Localized nonlinear regions highlighted in red: (a) full structural model and (b) masonry portion.

The static nonlinear analysis follows the procedure and analysis settings outlined in the earlier analyses section. Masonry material properties are defined using the mean values of the parameters from the dataset used to train the fine-mesh surrogate models. The capacity curve is derived and compared to the capacity curve obtained from the full nonlinear model which has been shown below.

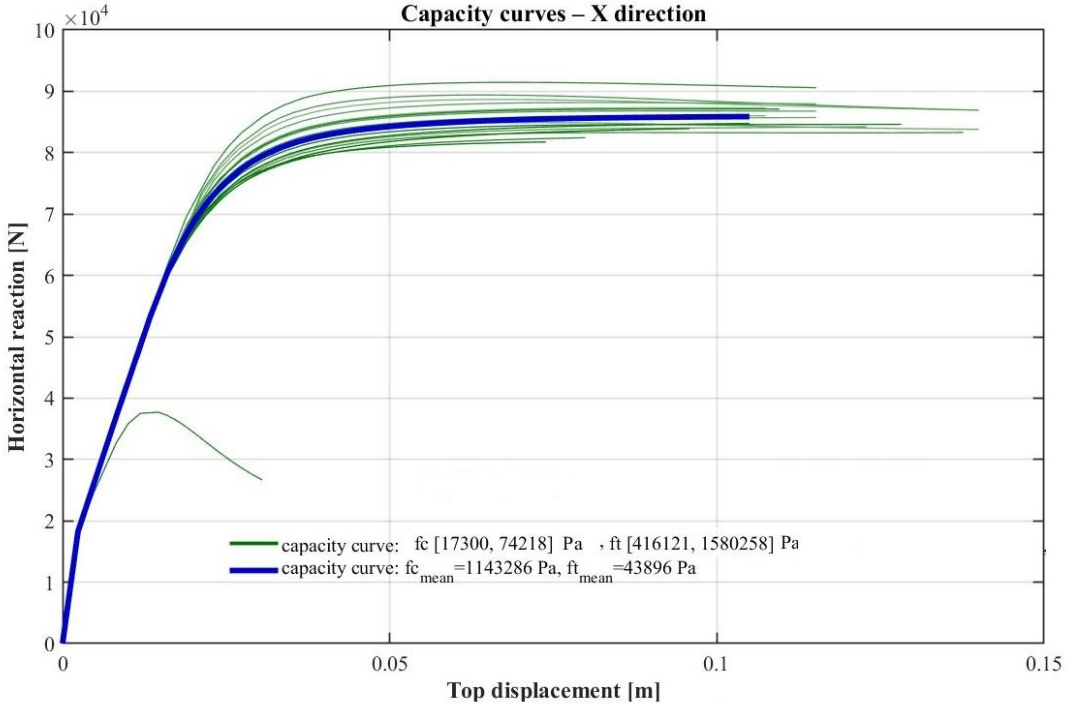

Figure 83 Capacity curves for localized nonlinear model (blue) and full nonlinear model (green) X - direction

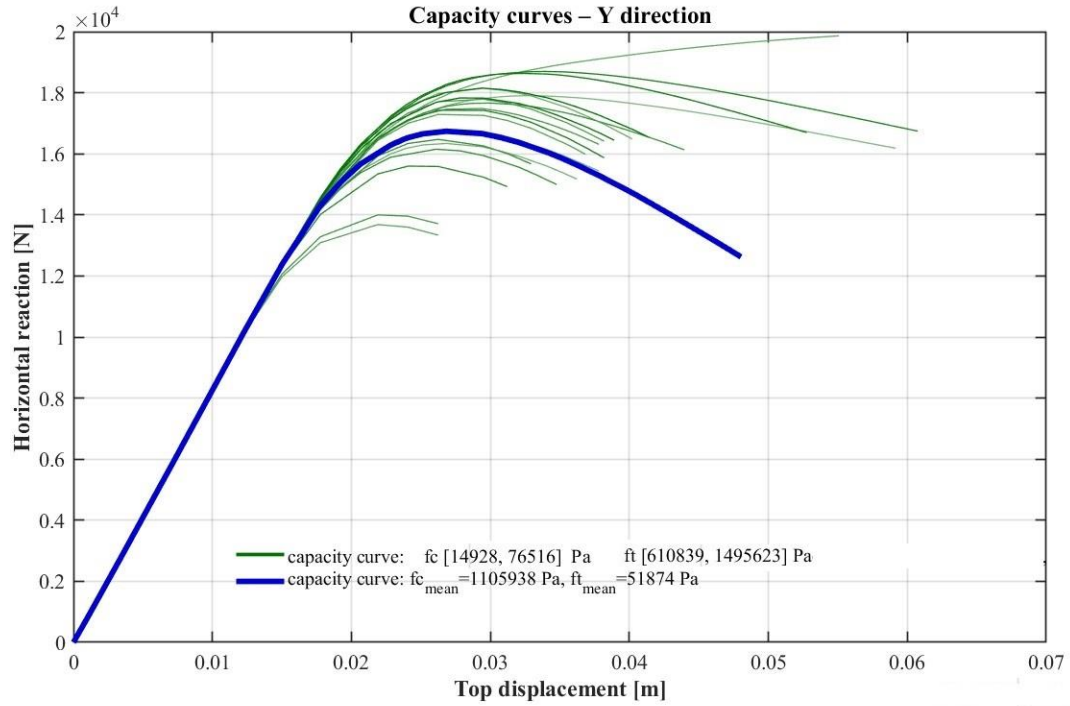

Figure 84 Capacity curves for localized nonlinear model (blue) and full nonlinear model (green) Y - direction

Analysis of the capacity curve indicates that modeling only the vulnerable region of

the structure can accurately simulate the results of full nonlinear modeling. Additionally, this approach mitigates convergence issues caused by stress concentrations that typically occur at loaded nodes during static nonlinear analysis.

In conclusion, the ductility factor for both the x and y directions is evaluated, consistent with the methodology applied in the static nonlinear analysis. Previously, this assessment used the 'real value' of the mechanical parameter in a medium-mesh model. In the present analysis, the capacity curve is derived for the fine mesh-size model using the mean value of the mechanical parameter.

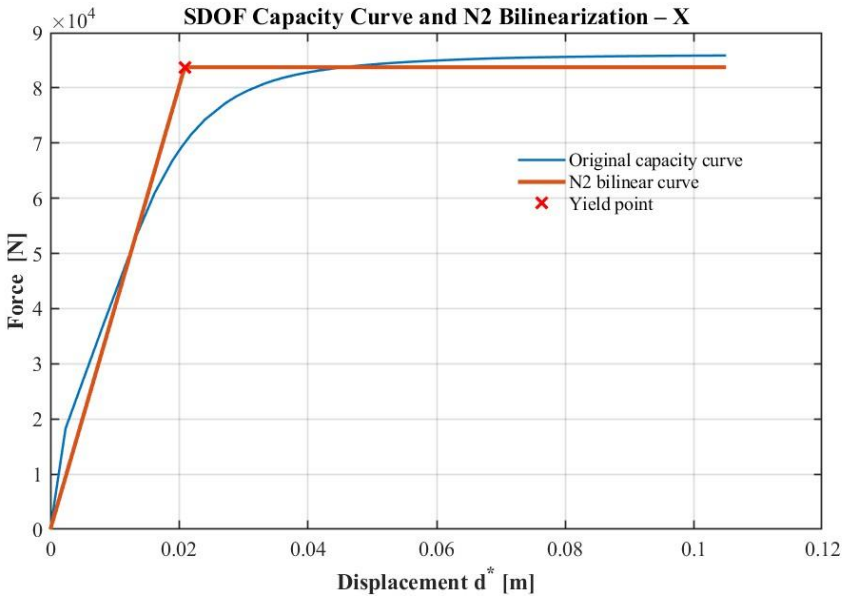

Figure 85 SDOF capacity curve and N2 bilinearization X- direction

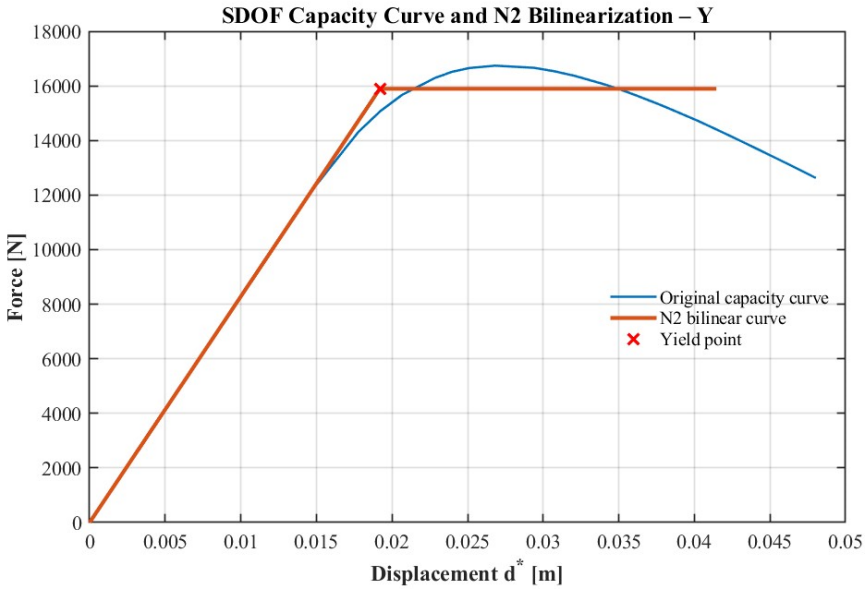

Figure 86 SDOF capacity curve and N2 bilinearization Y- direction

The ductility factor and related parameters were derived and discussed in detail in the static nonlinear analysis section. Here, only the final values are reported for this model.

Bilinear curve for X direction			**Bilinear curve for Y direction**		
Parameter	Value	Unit	Parameter	Value	Unit
F_{bu}	85877.896	N	F_{bu}	16738.850	N
0.6 F_{bu}	51526.738	N	0.6 F_{bu}	10043.310	N
0.85 F_{bu}	72996.212	N	0.85 F_{bu}	14228.023	N
F_y	83742.840	N	F_y	15892.793	N
0.6Fu disp	0.0128	m	0.6Fu disp	0.0121	m
d_y	0.0209	m	d_y	0.0192	m
du	0.1050	m	du	0.0415	m
μ	5.030	-	μ	2.159	-

Table 16 Bilinear curve parameter for X and Y direction

6.0 Discussion

Nonlinear analysis of large masonry structures, such as bell towers, is computationally intensive, especially when a fine mesh is required to accurately capture localized cracking and strain concentrations. The primary objective of this thesis is to reduce computational demand associated with nonlinear analysis. For example, on a relatively powerful workstation (Intel® Xeon® E5-2630 v4, 20 CPUs, 64 GB RAM, 34 GB GPU memory), a full nonlinear simulation with a 0.3 m mesh required approximately 27 minutes in ANSYS Mechanical APDL 2020 R2. On standard engineering machines with fewer resources, the computational cost would be even greater, rendering repeated analyses impractical.

In contrast, the proposed nonlinear model greatly reduces the number of elements that need to be treated as nonlinear. On the same workstation, this model completed a full static nonlinear analysis in only 15 minutes, reducing computational time by 45%. While the time savings may seem moderate, it is a significant improvement because the localized model still captures the key structural response and avoids unnecessary nonlinear calculations in the rest of the tower. By focusing on nonlinearity only in the critical zone, the mesh can also be refined further without increasing the computational cost to that of a full nonlinear simulation.

A further limitation of relying only on full nonlinear FE simulations is the strong sensitivity to the mesh. Improving the spatial resolution directly in ANSYS would require substantially more computation time and memory, making it unsuitable for repeated analyses. For this reason, a surrogate-based strategy was introduced. Using Gaussian Process Regression together with the model optimization framework, implemented in MATLAB, the strain response of the tower could be approximated efficiently without running additional nonlinear simulations.

The surrogate model played a central role in making the analysis manageable. By learning the relationship between the material parameters and the strain response from a limited set of nonlinear FE simulations, it allowed the behavior of the tower to be explored over the full parameter domain without performing additional costly analyses. The optimization framework then used these surrogate predictions to

evaluate how different values of f_c and f_t influence the damage distribution. Through this process, the algorithm was able to highlight the parameter combinations that consistently lead to higher vulnerability and more concentrated damage.

This information provided a clear basis for identifying the region of the tower where nonlinear effects are most likely to occur and for selecting a threshold that separates significant from non-significant zones. As a result, the definition of the nonlinear region in the localized model is supported directly by the behavior indicated by the surrogate and refined by the model optimization process, demonstrating that the adopted approach is both coherent and technically justified.

7.0 Conclusion

This study conducted a seismic assessment of a historic masonry bell tower using advanced nonlinear modelling, aiming to enhance computational efficiency while maintaining the reliability of the structural response. The findings indicate that performing full nonlinear analyses on the entire structure, using detailed meshes and realistic material laws, is computationally intensive for large and irregular masonry systems. To overcome this challenge, a hybrid approach was adopted in which only the most vulnerable section of the tower, identified through surrogate-based damage estimation and Bayesian refinement, was modelled with nonlinear constitutive behavior, while the remaining structure was represented as elastic.

The results indicate that the localized nonlinear approach can reproduce the essential features of the global structural response while substantially reducing computational effort. The observed damage concentration is consistent with the expected behavior of slender masonry towers, thereby confirming the validity of the modeling framework and its applicability to practical seismic assessment. In summary, the proposed workflow offers an efficient and robust alternative to full-scale nonlinear modeling, especially for historical structures where computational cost and model calibration present significant challenges.

Future research could improve the methodology by refining surrogate models with additional numerical data and by applying the framework to a wider range of tower geometries or loading scenarios to assess its generalizability.

References

[1] Crocetti, Alessio, Miraglia, Gaetano, Ceravolo, Rosario, Ciavarrella, Giovanni, Scussolini, Linda, and Taliano, Maurizio, “Symptom-based Prognosis through Integrated Digital Models and Experimental Data,”

[2] P. J. B. B. Lourenço, *Computational strategies for masonry structures*. Delft: Delft Univ. Press, 1996.

[3] A. Page, “THE BIAXIAL COMPRESSIVE STRENGTH OF BRICK MASONRY.,” *Proceedings of the Institution of Civil Engineers*, vol. 71, no. 3, pp. 893–906, Sept. 1981, doi: 10.1680/iicep.1981.1825.

[4] H. B. Kaushik, D. C. Rai, and S. K. Jain, “Stress-Strain Characteristics of Clay Brick Masonry under Uniaxial Compression,” *J. Mater. Civ. Eng.*, vol. 19, no. 9, pp. 728–739, Sept. 2007, doi: 10.1061/(ASCE)0899-1561(2007)19:9(728).

[5] European Committee of Standardization (CEN), *Design of masonry structures. Part 1-1: General rules for buildings—Reinforced and unreinforced masonry.*, Eurocode 6 ENV 1996-1-1, Brussels, Belgium.

[6] N. Mariacarla, “Micromechanical and macromechanical approaches for the analysis of periodic masonry structures,” PhD Thesis in Structural Engineering, SAPIENZA UNIVERSITA DI ROMA, ROMA, ITALY, 2021.

[7] J. A. Campbell Barraza, *Numerical model for nonlinear analysis of masonry walls*, 1. Aufl. in Mitteilungen des Lehrstuhls für Baustatik und Baudynamik, Fakultät für Bauingenieur- und Vermessungswesen, Rheinisch-Westfälische Technische Hochschule Aachen, no. 22. Aachen: Mainz, 2012.

[8] “Ansys Help.”

[9] A.T. Vermeltfoort and Theo Raijmakers and H.J.M. Janssen", “Shear tests on masonry walls,” *“Technomic Publ. Co.”,* no. "Hamid, \{Ahmad A.\} and Harris, \{Harry G.\}", pp. 1183--1193, 1993.

[10] M. Sekkaki and A. Chaaba, “Failure Analysis of Masonry Walls in 2D and 3D Subjected to Combined Compression and Shear Loading,” *cea*, vol. 12, no. 6, pp. 3944–3961, Nov. 2024, doi: 10.13189/cea.2024.120614.

[11] M. Wojciechowski, “A note on the differences between Drucker-Prager and Mohr-Coulomb shear strength criteria,” *Studia Geotechnica et Mechanica*, vol.

40, no. 3, pp. 163–169, Oct. 2018, doi: 10.2478/sgem-2018-0016.

[12] Z. P. Bažant and B. H. Oh, “Microplane Model for Progressive Fracture of Concrete and Rock,” *J. Eng. Mech.*, vol. 111, no. 4, pp. 559–582, Apr. 1985, doi: 10.1061/(ASCE)0733-9399(1985)111:4(559).

[13] A. Daneshyar and M. Ghaemian, “Coupling microplane-based damage and continuum plasticity models for analysis of damage-induced anisotropy in plain concrete,” *International Journal of Plasticity*, vol. 95, pp. 216–250, Aug. 2017, doi: 10.1016/j.ijplas.2017.04.011.

[14] Ministero delle Infrastrutture e dei Trasporti, *NORME TECNICHE PER LE COSTRUZIONI (NTC 2018)*, Jan. 17, 2018.

[15] A. K. Chopra, *Dynamics of structures: theory and applications to earthquake engineering*, Sixth edition in SI Units. Hoboken, NJ: Pearson, 2025.

[16] “Novel Tool for Selecting Surrogate Modeling Techniques for Surface Approximation,” in *Computer Aided Chemical Engineering*, vol. 50, Elsevier, 2021, pp. 451–456. doi: 10.1016/B978-0-323-88506-5.50071-1.

[17] G. MIRAGLIA, *Hy-Learn project*. (Dec. 10, 2024). Zenodo. doi: 10.5281/ZENODO.14363677.

Acknowledgement

First, I would like to express my deepest appreciation to Professor Rosario Ceravolo for granting me the opportunity to develop this thesis under his supervision. His scientific guidance, thoughtful insights, and continuous encouragement have been fundamental throughout the entire research process. I am sincerely grateful for the trust he placed in my abilities and for the support he provided at every stage of this work.

I am deeply grateful to my co-supervisors, Ing. Gaetano Miraglia, Ing. Linda Scussolini, and Ing. Alessio Crocetti, whose expertise, feedback, and consistent support were essential to this thesis. Their guidance extended beyond technical matters, offering clarity during complex moments, motivation in the face of challenges, and scientific direction throughout the research. I sincerely appreciate their invaluable contributions and dedication.

در ادامه لازم می‌دانم از پدر جان عزیزم و مادرِ جانِ مهربانم با تمام وجود قدردانی کنم؛
کسانی که عمر و جوانیِ خود را برای من گذاشتند و هرچه امروز دارم، نتیجه دعاها، فداکاری‌ها و عشق بی‌پایان آن‌هاست.
از همسر زیبایم که در تمام لحظات سخت و آسان کنارم بود و با صبر و مهربانی‌اش مرا همراهی کرد و انگیزه ادامه مسیر را به من بخشید، صمیمانه سپاسگزارم.
همچنین از فرزند عزیزم که حضورش بزرگ‌ترین دلگرمی زندگی من است، با تمام قلبم تشکر می‌کنم.
در کنار آن‌ها، از خانواده محترم و دوست‌داشتنی‌ام نیز کمال قدردانی را دارم؛
خانواده‌ای که همیشه پشتیبان من بودند، با محبت و مهربانی مرا دلگرم کردند و آرامش و امنیتی را فراهم ساختند که بدون آن طی‌کردن این مسیر ممکن نبود.
حمایت‌های بی‌دریغ، دعای خیر، صبوری و همراهی آن‌ها بزرگ‌ترین سرمایه و نیروی من در این راه بوده است.
این پایان‌نامه را با افتخار به پدر و مادر عزیزم، همسر و فرزندم و تمامی اعضای خانواده‌ام تقدیم می‌کنم؛
به عشق و به خاطر همه چیزهایی که برای من بوده‌اند و خواهند بود